

# A comprehensive study of corneal tissue responses to customized surgical treatments

Citation for published version (APA):

Francis, M. (2023). *A comprehensive study of corneal tissue responses to customized surgical treatments*. [Doctoral Thesis, Maastricht University]. Maastricht University. <https://doi.org/10.26481/dis.20230619mf>

## Document status and date:

Published: 01/01/2023

## DOI:

[10.26481/dis.20230619mf](https://doi.org/10.26481/dis.20230619mf)

## Document Version:

Publisher's PDF, also known as Version of record

## Please check the document version of this publication:

- A submitted manuscript is the version of the article upon submission and before peer-review. There can be important differences between the submitted version and the official published version of record. People interested in the research are advised to contact the author for the final version of the publication, or visit the DOI to the publisher's website.
- The final author version and the galley proof are versions of the publication after peer review.
- The final published version features the final layout of the paper including the volume, issue and page numbers.

[Link to publication](#)

## General rights

Copyright and moral rights for the publications made accessible in the public portal are retained by the authors and/or other copyright owners and it is a condition of accessing publications that users recognise and abide by the legal requirements associated with these rights.

- Users may download and print one copy of any publication from the public portal for the purpose of private study or research.
- You may not further distribute the material or use it for any profit-making activity or commercial gain
- You may freely distribute the URL identifying the publication in the public portal.

If the publication is distributed under the terms of Article 25fa of the Dutch Copyright Act, indicated by the "Taverne" license above, please follow below link for the End User Agreement:

[www.umlib.nl/taverne-license](http://www.umlib.nl/taverne-license)

## Take down policy

If you believe that this document breaches copyright please contact us at:

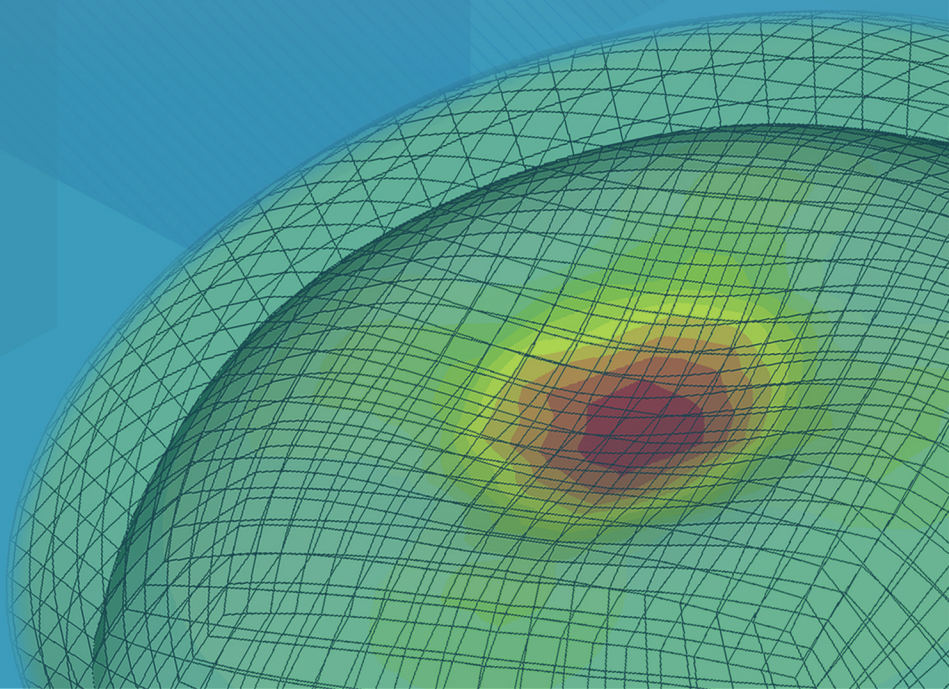
[repository@maastrichtuniversity.nl](mailto:repository@maastrichtuniversity.nl)

providing details and we will investigate your claim.

# **A COMPREHENSIVE STUDY OF CORNEAL TISSUE RESPONSES TO CUSTOMIZED SURGICAL TREATMENTS**

---

**MATHEW FRANCIS**







# **A Comprehensive Study of Corneal Tissue Responses to Customized Surgical Treatments**

## **DISSERTATION**

To obtain the degree of Doctor at Maastricht University, on the  
authority of the Rector Magnificus, Prof. dr. Pamela Habibović

---

In accordance with the decision of the Board of Deans, to be defended  
in public on Monday October 9<sup>th</sup> 2023 at 10.00 hours

---

By

**Mathew Francis**

**Supervisors:**

Prof. dr. R.M.M.A. Nuijts

Dr. R. Shetty (Narayana Nethralaya Eye Hospital, Bangalore, India)

**Co-supervisor:**

Dr. A.S. Roy (Narayana Nethralaya Foundation, Bangalore, India)

**Assessment Committee:**

Prof. dr. D.E.J. Linden (Chair)

Prof. dr. J. Hjortdal (Aarhus University Hospital, Denmark)

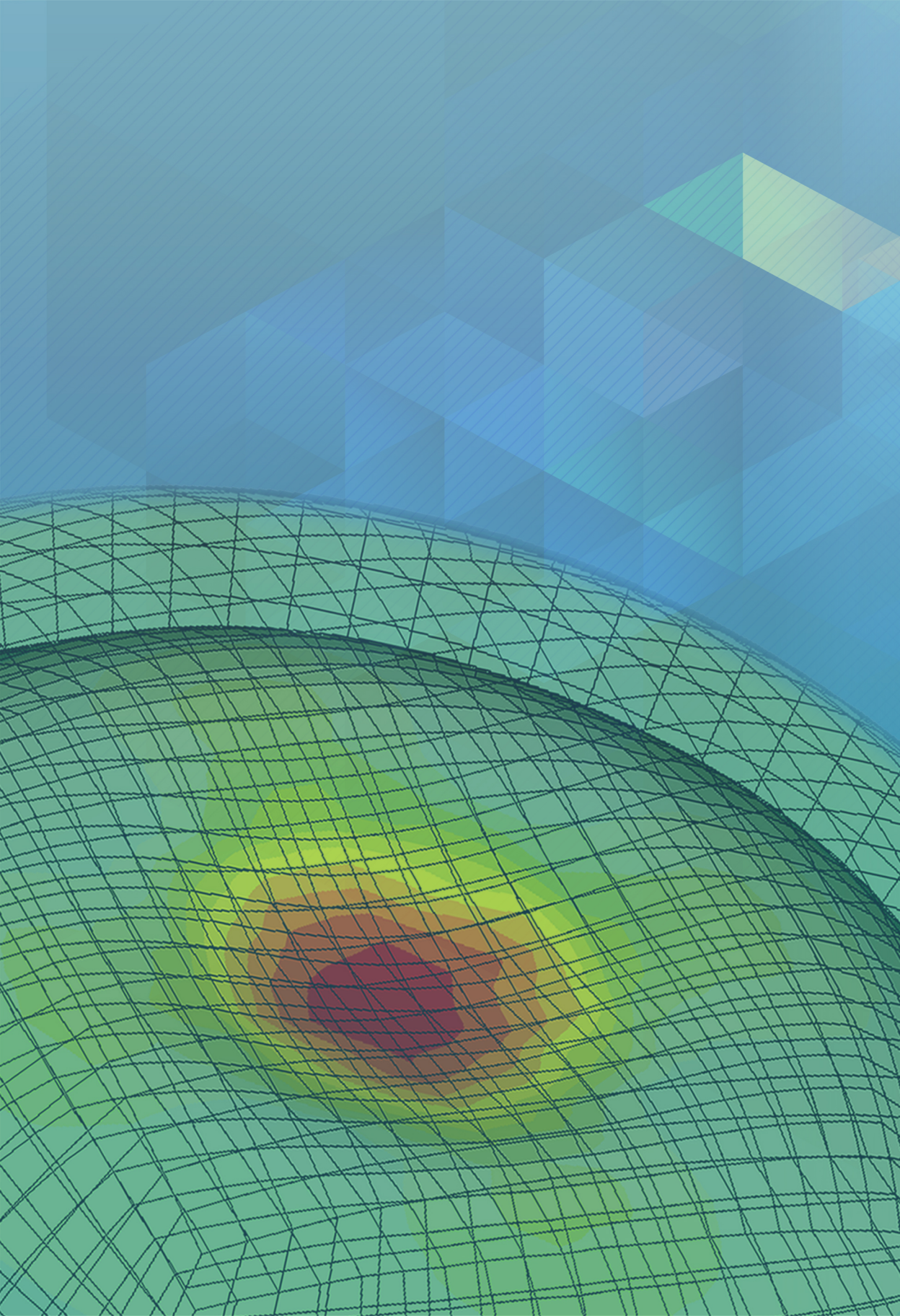
Dr. M. Lombardo (Studio Italiano di Oftalmologia, Rome, Italy)

Prof. dr. M.A.M.J. van Zandvoort



# Table of contents

1.	Introduction	1
2.	Waveform analysis of deformation amplitude and deflection amplitude in normal, suspect, and keratoconic eyes	33
3.	Corneal viscous properties cannot be determined from air-puff applanation	73
4.	Corneal biomechanical changes and tissue remodeling after SMILE and LASIK	99
5.	In vivo prediction of air-puff induced corneal deformation using LASIK, SMILE, and PRK finite element simulations	131
6.	A novel simulation software to predict postoperative corneal stiffness prior to laser vision correction	169
7.	Customization of corneal crosslinking in keratoconus using eye specific computational modeling	207
8.	Discussion	239
9.	Summary	271
10.	Impact paragraph	277
11.	Acknowledgement	283
12.	Curriculum vitae	289





**Chapter 1**

---

# **Introduction**





The cornea is the tough outermost layered structure of the eye.<sup>1</sup> It maintains a distinct shape against intraocular pressure (IOP) induced forces, which helps in refracting light towards the retina along with its transparency and refractive index.<sup>2, 3</sup> The mechanical strength or stiffness for maintaining such a distinct corneal curvature comes from the stromal layer.<sup>1,2</sup> The stromal layer occupies about 90% of the human corneal thickness and is made up of sheets of lamellae composed of collagen fibrils and extracellular matrix.<sup>1, 3, 4</sup> However, uncorrected vision may not always be of the desired level due to abnormal axial length or corneal surface defects resulting in the need for corrective glasses, contact lenses or implantable collamer lenses.<sup>5</sup> In certain cases, elective laser vision correction (LVC) surgery is chosen instead of lens-based solutions.<sup>5</sup> LVC surgery is one of the most popular elective surgeries around the world.

Photorefractive keratectomy (PRK) brought about the LVC surgery era; it was first performed in the year 1987 by Theo Seiler.<sup>6, 7</sup> PRK procedure begins with the removal of the epithelial layer, followed by the ablation of equivalent tissue to achieve the desired refractive correction on the now exposed stroma using an excimer laser.<sup>8</sup> Epithelial removal in PRK surgery was widely associated with post-surgery pain and increased recovery time after surgery.<sup>6, 8, 9</sup> Corneal haze and regression of treatment were observed after the PRK procedure, with an increased incidence and severity when higher refractive corrections were attempted.<sup>6, 8, 9</sup> The PRK era was followed

by laser-assisted in situ keratomileusis (LASIK). LASIK combined the microkeratome blade and the excimer laser to correct a few microns below Bowman's layer in the stroma for preserving epithelium and Bowman's layer.<sup>10-12</sup> The LASIK procedure creates a hinged flap using the microkeratome, followed by ablation on the exposed stroma using an excimer laser.<sup>12</sup> LASIK quickly overtook the refractive surgery volume due to its shorter recovery time and increased patient comfort.<sup>8,</sup><sup>12</sup> A Femtosecond laser-assisted flap cut was introduced in the year 2001 to reduce microkeratome blade related complications.<sup>13,14</sup> Femtosecond laser is a pulsed laser which causes photo-disruption rather than photo-ablation.<sup>15</sup> Photo-disruption is the process of using a laser to create ionized molecules which cause shockwaves followed by tissue ruptures.<sup>15</sup> Introduction of the femtosecond laser allowed precise flap cut which resulted in less undesired aberrometric changes.<sup>12</sup> A Femtosecond LASIK procedure has a significant logistic issue, as it needs two separate laser platforms and patient transfer mid procedure from a femtosecond laser to the excimer laser platform to complete the procedure. A novel technique was soon introduced in clinics combining the merits of flapless and non-surface ablation procedures at the same time called small incision lenticule extraction (SMILE).<sup>16</sup> Here, the cornea was docked to a Femtosecond laser platform (VisuMax Laser System, Carl Zeiss Meditec AG, Jena, Germany) followed by an anterior and posterior lenticule surface cut according to the desired refractive correction called a cap cut.<sup>17</sup> In SMILE, the laser passes through the epithelium, the Bowman's layer and anterior stroma; but

causes photo-disruption at the laser focal point.<sup>16</sup> The lenticule was then removed via a 2 – 3 mm side-cut in the superior zone of the cornea.<sup>16</sup> Studies have shown that the anterior stroma has higher tensile strength (maximum stress a material can endure) in comparison to the posterior cornea using mathematical models.<sup>18</sup> The anterior stroma has a higher degree of interweaving and branching collagen fibre network in comparison to the posterior cornea which is spared in LASIK and SMILE.<sup>19</sup> Hence, intuitively LASIK and SMILE enjoy an edge over PRK surgery due to their deeper tissue removal site. Also, SMILE preserves the peripheral lamellar layer in the anterior stroma, unlike LASIK.<sup>16</sup> Mathematical models have predicted higher postoperative tensile strength in SMILE compared to LASIK,<sup>20</sup> and suggested lesser biomechanical risk.<sup>21</sup>

All LVC surgery spatially alters the corneal stroma thickness by subtracting the tissue equivalent to the spherocylindrical power to improve the visual acuity.<sup>16,22</sup> Due to the tissue subtractive nature of the LVC procedure, they cause a reduction in corneal stiffness and could undermine the biomechanical balance of the cornea.<sup>16, 22, 23</sup> Ectasia is a class of progressive degenerative disorders thought to be caused due to altered biomechanical balance of the cornea.<sup>23, 24</sup> Keratoconus is an ectatic disorder, where localized biomechanical weakness causes clinical signs such as corneal curvature changes, corneal thinning, increased aberration, blurred vision, etc.<sup>23-26</sup> Another ectatic disorder is the post-LVC ectasia, where the above symptoms manifest after LVC



surgery insult to the otherwise seemingly healthy cornea on clinical assessment.<sup>23, 25</sup> However, many articles have implied that the LVC ectasia in fact could be a result of undiagnosed subclinical keratoconus before surgery.<sup>27-29</sup> An epidemiological study found 171 ectasia eyes of which 95.9% were post-LASIK and 4.1% were post-PRK between the years 1998 and 2005 among post LVC eyes.<sup>30</sup> Another study reviewing 30,167 LASIK surgery cases over 8 years found an ectasia incidence of 0.033% and concluded current risk factors were not sufficient to screen potential ectasia cases.<sup>31</sup> Even with mathematical models reporting biomechanical advantages of SMILE surgery,<sup>20, 21</sup> ectasias were still being reported after the SMILE procedure.<sup>25, 32</sup> A report presented in 2019 reported 6 eyes developed ectasia out of 10,394 eyes that underwent SMILE surgery in 6 years (0.058% of all operated eyes).<sup>33</sup> All the above studies reporting post-LVC ectasia had also noted that a significant portion of the eyes among the ectatic set had topographical abnormalities preoperatively.<sup>25, 30, 31</sup> As Sinha Roy et al. pointed out mathematical models reporting advantages for one surgical technique were using models derived from normal eyes, thus patient screening is still an essential part of ectasia avoidance.<sup>34</sup> Sensitive tools are thus required to understand corneal biomechanics to separate keratoconic eyes from normal ones. Also, predicting possible corneal stiffness after surgery using computational modelling (currently not possible with any devices or algorithms) could provide a decisive edge in minimizing ectasia manifestation risk after LVC.

Collagen cross-linking (CXL) is a surgical procedure where topically applied riboflavin (vitamin B2) soaked cornea is treated with an Ultraviolet A (UVA) light source to form chemical bonds between lamellae layers.<sup>35</sup> The idea of CXL was shown by Spoerl and Seiler in 1998 on de-epithelized porcine corneas.<sup>36</sup> CXL induced interlamellar bonds had shown to improve corneal stiffness in the ex-vivo cornea.<sup>36</sup> It was soon followed by a pilot clinical study by Wollensak et.al. in 2003, where CXL was found to be effective in stopping progressive keratoconus.<sup>37</sup> Long term results have shown CXL could be used to stabilize or in certain cases to improve the visual acuity of post-LVC ectasia eyes.<sup>38,39</sup> The early CXL procedures were based on the safe and effective Dresden protocol, where UVA irradiance was carried out for 30 min using the power of  $3\text{mW}/\text{cm}^2$  resulting in a dose of  $5.4\text{ J}/\text{cm}^2$ .<sup>35,37,40</sup> The Dresden protocol also included an additional 30 min soak time before UVA irradiation, resulting in a longer procedural time. Hence, accelerated CXL strategies were proposed utilizing higher power levels with a lower UVA irradiation time (Bunsen Roscoe Law).<sup>41</sup> Also, studies showed that accelerated CXL causes less tissue dehydration and optical haze after treatment in comparison to the Dresden protocol.<sup>42</sup> Sinha Roy and Dupps proposed the use of smaller diameter UVA treatment centred on the affected zone of the ectasia rather than on the corneal apex centration used in standard and accelerated CXL, based on a patient-specific computational model.<sup>43</sup> The model suggested greater corneal stiffness benefit due to focused treatment and reduced CXL effects on relatively healthy surrounding tissue.<sup>43</sup> KXL II system

(Glaukos Corporation, USA formerly Avedro Inc, USA) is one of the clinical system for a customized CXL treatment on human cornea. Currently, a randomized clinical trial by Vandevenne et al. is underway to compare customized CXL to Dresden protocol based CXL in our department (ClinicalTrials.gov Identifier: NCT04532788).<sup>44</sup> Early clinical studies report customized CXL induced greater flattening in the keratoconic cornea.<sup>45-47</sup> Reports also suggest customized CXL could have a faster recovery time as significantly reduced denervation and cell apoptosis were observed in the area surrounding the treatment zone<sup>47</sup>, along with shorter epithelial healing time<sup>45</sup>. Studies have also indicated that a reduced region of treatment in a customized treatment approach could result in a lower average UVA dose delivered to the cornea.<sup>45, 48</sup> However, the challenge was to locate the actual disease affected degeneration zone and target these sites with maximum UVA power.<sup>48</sup> A study by Shetty et al. looked into different methods of treatment planning involving axial and tangential curvature maps, and treatment delivery using axial rings and sectors.<sup>48</sup> The studies conclude that concentric rings centred on the steepest tangential curvature point provided maximum flattening thereby better visual acuity.<sup>48</sup> As no clinical data directly define the degeneration zone, alternate interpretations using curvature and thickness map were relied upon to make assumptions.<sup>24, 45, 46, 48</sup> In summary, customized CXL treatment could be the next innovation in the treatment of keratoconus or post-LVC ectasia, provided an effective corneal degeneration zone estimation methodology could be demonstrated.

## **In-vivo corneal biomechanics assessment**

In material science, evaluation of mechanical property requires stress and an understanding of the resultant strain on an object. It is also possible to measure mechanical properties using inelastic scattering, e.g. spontaneous Brillouin scattering.<sup>49</sup> In mechanical testing, an increase in stress and the corresponding strain is recorded to form the stress-strain curve which describes the mechanical behaviour of the structures, such as the cornea. The material property parameter derived from the slope of the stress-strain curve within the linear elastic region of the curve is called Young's modulus.<sup>50, 51</sup> Almost all biological tissues are viscoelastic, meaning they have both elastic and viscous nature at the same time.<sup>50, 52</sup> Being viscoelastic, the stress-strain relationship for biological tissue such as cornea would be a hysteresis loop rather than a linear line (as in the case of elastic material) and the area enclosed by the hysteresis loop represents the loss of energy during the deformation process.<sup>50, 52</sup> Also, it is not just one stress-strain relationship but a family of relationships, depending on the loading rate.<sup>50, 52</sup>

The first device that estimated in-vivo corneal biomechanics was the ocular response analyser (ORA; Reichert Ophthalmic Instruments, Buffalo, NY). ORA is a bi-directional air-puff applanation based non-contact tonometer.<sup>53</sup> ORA has an electro-optical collimation detection system that records the infrared beam reflecting from the central 3mm

zone of the cornea.<sup>53, 54</sup> ORA makes two distinct measurements when the cornea is flattened, within a 20 msec time frame after the start of the air-puff, distinguished by maximum infrared signal return.<sup>53</sup> The first measurement is at the time when the corneal surface flattens for the first time due to air-puff deformation called applanation 1 (A1) time point.<sup>53</sup> Immediately after A1, the air pump responsible for the air-puff is turned off and thus the air pressure reduces.<sup>53</sup> Meanwhile, the cornea would continue past the A1 time to reach the highest concavity (HC) state and then start to regain its normal convex shape.<sup>53</sup> Afterwards, during the reforming phase, the cornea would again reach a flattened state called applanation 2 (A2) time point.<sup>53</sup> ORA reports two distinct biomechanical terms namely the corneal hysteresis (CH) and the corneal resistance factor (CRF).<sup>55-58</sup> CH is the pressure difference at A1 and A2 time points called P1 and P2 respectively.<sup>55, 57, 58</sup> CRF is calculated from the following equation.<sup>55, 57, 58</sup>

$$CRF = a[P1 - 0.7 * P2] + b$$

In the CRF equation,  $a$  and  $b$  are the constants to maximize the correlation to central corneal thickness (CCT).<sup>55, 57</sup> The overall pressure profile of the ORA has a shape similar to a Gaussian curve, but the peak pressure of the profile depends on the pressure at A1 time.<sup>55, 57</sup> CH and CRF are both empirical parameters representing a corneal response to air-puff and had no evidence to connect to the elastic behaviour parameters of the material such as Young's modulus.<sup>55</sup> Calculation of

Young's modulus with ORA data was troublesome due to the lack of a direct strain measure (deformation).<sup>59, 60</sup> CH was more related to the viscosity observed during applanation,<sup>55</sup> it was described as "*viscous damping* or *stress-damping capacity*" in an editorial in the Journal of Cataract and Refractive Surgery.<sup>59</sup> CRF on the other hand was described as resistance to the shear force created during fast indentation of the cornea.<sup>55</sup> This being said, recent studies have shown that CH and CRF have a flawed definition as they had ignored the extra-corneal deformation or whole eye movement during the air-puff applanation of the cornea which could lead to erroneous estimation of corneal mechanical properties.<sup>61</sup> Significantly decreased CH and CRF values were observed in keratoconic eyes in comparison to normal eyes, but the parameters failed to achieve good sensitivity and specificity for disease diagnosis.<sup>55, 57</sup> Similarly, CH and CRF parameters were found to be decreased after LVC surgery.<sup>55</sup> However, these parameters didn't show a significant difference between preoperative and 1-year post-CXL treatment.<sup>55</sup> Lower CH values were observed several weeks after CXL, which could be an effect of edema or tissue reorganization after CXL.<sup>55</sup> As all ORA measurements were based on the reflected infrared signals, hence requires an intact tear film for reliable measurement.<sup>55</sup>

A more recent device for quantifying in-vivo corneal biomechanics is the Corvis-ST (OCULUS Optikgeräte GmbH, Wetzlar, Germany) introduced in the year 2011.<sup>62</sup> Corvis-ST is a high-speed Scheimpflug camera based bi-directional air-puff applanation non-

contact tonometer.<sup>62</sup> The Scheimpflug camera records at a frame rate of 4,330 frames per second for a duration of 32.33 msec (140 frames).<sup>63</sup> The camera records horizontal (nasal to temporal) tomographic section images of the eye passing through the corneal apex with an 8mm capture width illuminated with a 455 nm light source.<sup>63</sup> The device has an internal pressure sensor that records the air-puff pressure profile created by the forceful ejection of air through a nozzle.<sup>61</sup> The Corvis-ST pressure profile is constant for all measurements with a max pressure of 25 KPa.<sup>63</sup> Terminology used to describe corneal applanation phases during Corvis-ST air-puff is similar to the ORA; consisting of A1, HC and A2 time points.<sup>63</sup> From the captured video of applanation, Corvis-ST reports the position of the anterior and posterior corneal edge (using 576 measurement points) and the corresponding air-puff pressure in the millisecond time and millimetre of mercury scale respectively. The anterior and posterior corneal edge is then available in the form of a comma-separated values (CSV) file.<sup>64</sup> The device also analyses the anterior edge of the cornea from the applanation video at three distinct locations, at the corneal apex and two peripheral points at the nasal and temporal regions.<sup>64-66</sup> The waveform generated by the displacement of the apex position of the cornea is called the deformation amplitude (DA) curve, figure 1.<sup>64, 65</sup> The displacement of the two peripheral points is arithmetically averaged to form the whole-eye movement (WEM) curve, figure 1.<sup>64, 65</sup> Then the arithmetical difference of DA and WEM is taken as the true deformation of the cornea called as deflection amplitude (DfA) curve, figure 1.<sup>64, 65</sup> Much similar to ORA, Corvis-ST



also reports quite a few empirical parameters.<sup>63, 67</sup> The most significant of these parameters are listed in table 1.

Table 1: Most significant Corvis-ST report empirical parameters.

Parameters (unit)	Description
Peak DA (mm)	The maximum value of DA during the air-puff applanation.
Peak DfA (mm)	The maximum value of DfA during the air-puff applanation.
Peak WEM (mm)	The maximum value of WEM during the air-puff applanation.
biomechanical-compensated IOP (bIOP)	Corrected IOP measurement for the effects of CCT and age. <sup>68</sup>
Stiffness parameter - A1 (SP-A1)	Stiffness parameter at A1, adjusted pressure at A1 timepoint minus bIOP (equivalent to force) whole divided by DfA at A1. <sup>69</sup>
DA ratio 1mm	DA ratio between the apex and at 1 mm from the apex. <sup>62, 69</sup>
DA ratio 2mm	DA ratio between the apex and at 2 mm from the apex. <sup>62, 69</sup>

In 2016, a new logistical regression-based term built using empirical Corvis-ST parameters called Corneal biomechanical index (CBI, a unit-less value between 0 and 1) was introduced to separate normal from keratoconic eyes.<sup>69</sup> An initial development study with 658 eyes showed a sensitivity and specificity of more than 94% in testing and validation for a CBI value of 0.5.<sup>69</sup> It was followed by a new parameter called Tomographic and Biomechanical Index (TBI, a unit-

less value between 0 and 1) in 2017, which combined Pentacam HR (OCULUS Optikgeräte GmbH, Wetzlar, Germany) tomographic parameters and Corvis-ST biomechanical parameters for enhancing ectasia detection using a random forest artificial intelligence (AI) classifier.<sup>62</sup> A development study of TBI had achieved good classification across groups, especially identifying the very asymmetric ectatic eyes, which had normal topography and were considered subclinical ectasia cases.<sup>62</sup> The TBI had a sensitivity and specificity of 90.4% and 96% respectively for a cut-off of 0.29 identifying very asymmetric ectatic eyes (area under the curve of 0.985).<sup>62</sup>

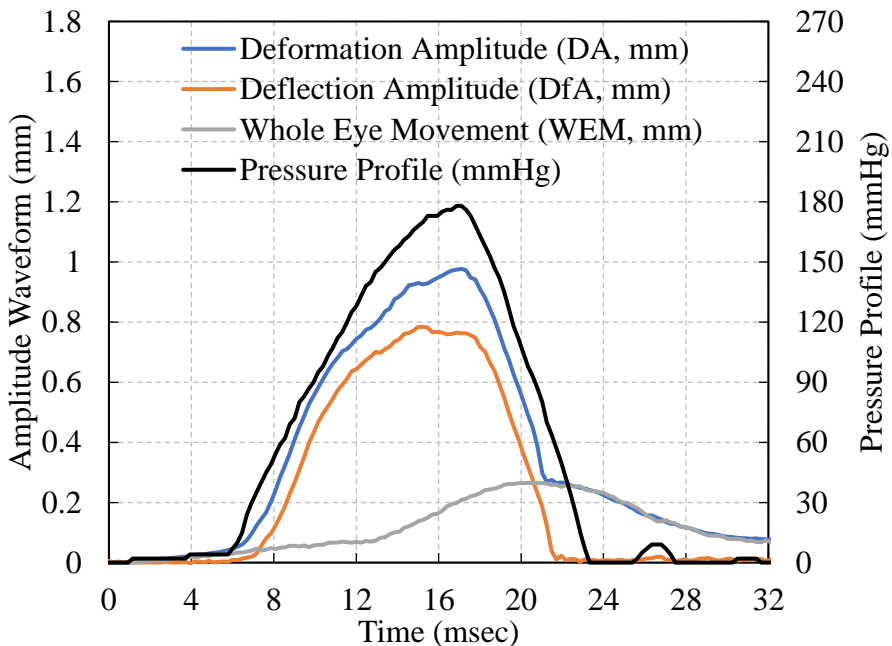


Figure 1: Corvis-ST amplitude waveforms (primary y-axis) and pressure profile (secondary y-axis).

Corvis-ST provides direct information regarding the air-puff pressure profile and corneal deformation required for biomechanical assessment. The pressure profile used by Corvis-ST was fixed across measurements with relatively unchanged peak pressure. While Corvis-ST enjoys few advantages over the ORA, a suitable whole waveform analysis based biomechanical model was needed to fully explore the true potential of Corvis-ST. Two methods could be used to fill this void, analytical biomechanical model (ABM) and finite element methods (FEM).

The ABM involves the use of one-dimensional elastic and viscous to model complex mechanical behaviour.<sup>70</sup> Elastic behaviour was modelled as a pure spring (stress is proportional to strain).<sup>70</sup> Viscous behaviour was modelled as a pure dashpot (stress is proportional to strain rate).<sup>70</sup> For modelling viscoelastic material a combination of spring and dashpot was used either in parallel or series arrangement.<sup>70</sup> The parallel arrangement of spring and dashpot to represent viscoelastic materials is called the Kelvin-Voigt model.<sup>70</sup> The series arrangement of the same is called the Maxwell model. Kelvin-Voigt model ensures equal stress to both spring and dashpot and was preferred for modelling organic polymers, rubber etc.<sup>70</sup> Stroma is generally equated to a rubber-like material and hence Kelvin-Voigt model was the preferred choice.<sup>60</sup> Glass DH et.al. proposed a standard linear solid model (which has an additional spring in series to a Kelvin-Voigt model) to demonstrate an experimental setup to quantify the biomechanical property using a

phantom cornea (soft contact lens).<sup>60</sup> The experimental setup used ORA reported pressure and externally recorded deformation from 500 frames per second high-speed camera to calculate viscoelastic material property.<sup>60</sup> However, the study suffered from the fundamental flaws of the ORA and was impractical for clinical use, but did show the merits of an ABM.

Han et al. proposed an ABM model comprising of parallel spring and dashpot connected to a lumped mass for calculating the deformation of the cornea under air-puff load.<sup>71</sup> The model used the air-puff pressure profile from the ORA and calculated theoretical deformation of the cornea and compared it to Corvis-ST recorded deformation.<sup>71</sup> This study concluded that the theoretical deformation calculated was in the same numerical order as the Corvis-ST measurement deformation.<sup>71</sup> Additionally, the study observed corneal vibration in both Corvis-ST measurement and the calculated deformation.<sup>71</sup> However, in a large clinical study, Han et al. proposed corneal vibration was rarely observed, the form followed the schematic amplitude shown in figure 1. Also, the ABM model was built without incorporating the effect of whole eye movement during air-puff applanation.<sup>61, 71</sup> Our team introduced a whole waveform-based ABM model in 2016,<sup>72</sup> which quantify corneal and extra-corneal stiffness along with extra-corneal viscoelasticity (described in **chapter 2**).<sup>65, 72-74</sup> The model was used in interpreting biomechanics of normal pediatric and adult eyes as well as post LVC and post CXL changes.<sup>65, 72-74</sup> ABM produces faster solutions

while using less computational resources to approximate an otherwise complex problem. ABM also enables the easy representation of biomechanical properties. However, this speed comes with compromises. The ABM reduced a 3-dimensional event to a one-dimensional problem with material being represented as a simple spring-dashpot network and is unable to calculate strain within the tissue due to deformation.

FEM is a numerical analysis method that derives an approximate solution to a problem using partial differential equations. The analysis involves dividing a system into a finite number of elements to derive the solution. The technique is widely used in mechanical, aerospace and civil engineering domains to understand structures, heat transfer, fluid flow, mass, electromagnetic potential etc. The use of FEM modelling of the cornea can be traced back to early works by Kobayashi et al. in 1971 and Woo et al. in 1972.<sup>75, 76</sup> However, these initial studies considered the corneal material property to be isotropic (having the same value when measured in different directions).<sup>75, 76</sup> One of the first research studies to use FEM models in understanding surgical effects was proposed by Pinsky and Datye in 1991.<sup>77</sup> This study used a much more detailed 3-dimensional model including effects of cut collagen fibrils, but assumed cornea to be a linear elastic material.<sup>77</sup> Kling et al. in 2014 proposed the first inverse FEM model-based estimation of in-vivo corneal material property using the dynamic deformation measured by Corvis-ST.<sup>78</sup> The inverse estimation used a 2-dimensional axis-

symmetric geometry and a linear viscoelastic material model in the FEM construction.<sup>78</sup> Other 2-dimensional models using Neo-Hookean hyperelastic material and second-order Ogden material were proposed by Jannesari et al. and Lago et al. for inverse estimation of in-vivo material property.<sup>79, 80</sup> Newer studies propose an anisotropic hyperelastic fibre dependent material model for the cornea.<sup>61, 81-85</sup> Mostly, the constitutive formulation was derived using free energy density rather than free energy to avoid introducing mass density in the stress-strain relationship.<sup>86</sup> Free energy density of cornea was defined as the sum of free energy density for extracellular matrix, in-plane fibres and cross-plane fibres.<sup>61, 81-85</sup> Roy et al. detailed an anisotropic hyperelastic fibre dependent material based FEM model utilizing a patient-specific 3-dimensional corneal mesh design using anterior and posterior corneal elevation data from Pentacam HR (a Scheimpflug tomographer) that showed excellent capture of dynamic deformation measured by Corvis-ST.<sup>61</sup> This FEM incorporated non-linear fibre distribution dependent material property for the cornea and lumped parameter (mass, spring and dashpot) for the extra-cornea to model the deformation amplitude observed by Corvis-ST.<sup>61</sup> However, no predictive corneal simulation exists in the literature that can predict corneal stiffness after refractive surgery using planned surgery parameters and preoperative in-vivo corneal biomechanics.

Based on the background information detailed above, the problem statements for this dissertation are the following.

1. The patient screening was reported as an important part of post-LVC ectasia prevention in the literature. Can in-vivo corneal stiffness calculated from Corvis-ST be used in finding clinical and sub-clinical keratoconic cornea from normal corneas?
2. The cornea is a viscoelastic material. However, the cornea was modelled as purely elastic material in ABM as viscus lag was not observed in the Corvis-ST waveform. Can corneal viscous properties be determined from Corvis-ST air-puff applanation?
3. Many preoperative corneal biomechanical assessment methods exist in the clinic. However, no clinical device or algorithm can predict post-LVC corneal stiffness. Can postoperative corneal stiffness be predicted using preoperative information?
4. Could predicted postoperative corneal stiffness be used in post-LVC ectasia prevention and maximizing corneal stiffness conservation during LVC surgery?
5. Experimental setups have shown the existence of a localized corneal biomechanical degeneration zone in the ectatic eye. Can the size of the corneal biomechanical degeneration zone be estimated in-vivo for effective planning of customized CXL?
6. What could be the efficacy of such a customized CXL treatment using corneal degeneration zone-based planning relative to current treatment options?



The above problem statements were fulfilled by developing and validating a predictive simulation platform called AcuSimX™ (Trademark of Narayana Ophthalmic Research and Development LLP, India; used after obtaining necessary permission). AcuSimX™ has two taskings; the first is to develop surgery specific predictive simulation for post-LVC corneal stiffness (figure 2). The second is customized CXL based ectasia treatment planning using a predictive simulation derived corneal degeneration map (figure 2). Preoperative calculation of corneal stiffness to classify suspicious and early keratoconus using a novel ABM is described in **chapter 2**. **Chapter 3** investigates the question regarding the detection of corneal viscosity using the current configuration of air-puff applanation device Corvis-ST. To develop a surgery specific predictive simulation for corneal stiffness after surgery, **chapter 4** looks into the events involved in the in-vivo tissue healing and biomechanical recovery after surgery. **Chapter 5** describes the surgery specific predictive simulation model that allows users to perform virtual surgery. **Chapter 5** also describes how FEM based in-vivo preoperative material property assessment method is transformed into a predictive simulation. Thus, helping the surgeon to select the best surgical procedure and optimize the surgical parameters for maximum corneal stiffness conservation. **Chapter 6** showcases the validation of the above predictive model using a large multicentric dataset collected from around the world. AcuSimX™ also has a FEM driven corneal degeneration map estimation model for effective planning of customized CXL procedures, as described in **chapter 7**.

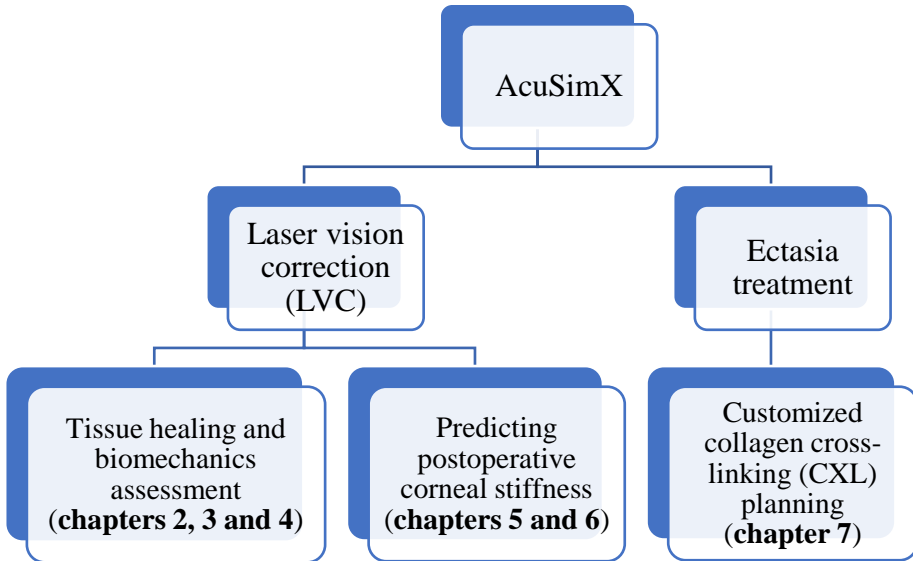


Figure 2: AcuSimX™ platform organization chart

## Reference

1. Levin LA, Kaufman PL. *Adler's physiology of the eye : clinical application*. 11th ed. Edinburgh ; New York: Saunders/Elsevier; 2011:xii, 795 p.
2. Koudouna E, Winkler M, Mikula E, Juhasz T, Brown DJ, Jester JV. Evolution of the vertebrate corneal stroma. *Prog Retin Eye Res* 2018;64:65-76.
3. Maurice DM. The structure and transparency of the cornea. *J Physiol* 1957;136:263-286.

4. Komai Y, Ushiki T. The three-dimensional organization of collagen fibrils in the human cornea and sclera. *Invest Ophthalmol Vis Sci* 1991;32:2244-2258.
5. Artal P. *Handbook of Visual Optics, Two-Volume Set*: CRC Press; 2017.
6. Alio JL, Soria FA, Abbouda A, Pena-Garcia P. Fifteen years follow-up of photorefractive keratectomy up to 10 D of myopia: outcomes and analysis of the refractive regression. *Br J Ophthalmol* 2016;100:626-632.
7. Seiler T, Wollensak J. Myopic photorefractive keratectomy with the excimer laser. One-year follow-up. *Ophthalmology* 1991;98:1156-1163.
8. Somani SN, Moshirfar M, Patel BC. Photorefractive Keratectomy. *StatPearls*. Treasure Island (FL); 2021.
9. Tomas-Juan J, Murueta-Goyena Larranaga A, Hanneken L. Corneal Regeneration After Photorefractive Keratectomy: A Review. *J Optom* 2015;8:149-169.
10. Pallikaris IG, Papatzanaki ME, Siganos DS, Tsilimbaris MK. A corneal flap technique for laser in situ keratomileusis. Human studies. *Arch Ophthalmol* 1991;109:1699-1702.
11. Buratto L, Ferrari M, Rama P. Excimer laser intrastromal keratomileusis. *Am J Ophthalmol* 1992;113:291-295.
12. Shah R. History and Results; Indications and Contraindications of SMILE Compared With LASIK. *Asia Pac J Ophthalmol (Phila)* 2019;8:371-376.

13. Kymionis GD, Kankariya VP, Plaka AD, Reinstein DZ. Femtosecond laser technology in corneal refractive surgery: a review. *J Refract Surg* 2012;28:912-920.
14. Perez-Straziota C, Randleman JB. Femtosecond-assisted LASIK: Complications and Management. *Int Ophthalmol Clin* 2016;56:59-66.
15. Chung SH, Mazur E. Surgical applications of femtosecond lasers. *J Biophotonics* 2009;2:557-572.
16. Sekundo W. *Small Incision Lenticule Extraction (SMILE): principles, techniques, complication management, and future concepts*: Springer; 2015.
17. Khamar P, Shetty R, Vaishnav R, Francis M, Nuijts R, Sinha Roy A. Biomechanics of LASIK Flap and SMILE Cap: A Prospective, Clinical Study. *J Refract Surg* 2019;35:324-332.
18. Randleman JB, Dawson DG, Grossniklaus HE, McCarey BE, Edelhauser HF. Depth-dependent cohesive tensile strength in human donor corneas: implications for refractive surgery. *J Refract Surg* 2008;24:S85-89.
19. Winkler M, Shoa G, Xie Y, et al. Three-dimensional distribution of transverse collagen fibers in the anterior human corneal stroma. *Invest Ophthalmol Vis Sci* 2013;54:7293-7301.
20. Reinstein DZ, Archer TJ, Randleman JB. Mathematical model to compare the relative tensile strength of the cornea after PRK, LASIK, and small incision lenticule extraction. *J Refract Surg* 2013;29:454-460.

21. Sinha Roy A, Dupps WJ, Jr., Roberts CJ. Comparison of biomechanical effects of small-incision lenticule extraction and laser in situ keratomileusis: finite-element analysis. *J Cataract Refract Surg* 2014;40:971-980.
22. Guarnieri FA. *Corneal biomechanics and refractive surgery*: Springer; 2015.
23. Ma J, Wang Y, Wei P, Jhanji V. Biomechanics and structure of the cornea: implications and association with corneal disorders. *Surv Ophthalmol* 2018;63:851-861.
24. Roberts CJ, Dupps WJ, Jr. Biomechanics of corneal ectasia and biomechanical treatments. *J Cataract Refract Surg* 2014;40:991-998.
25. Khamar P, Dalal R, Chandapura R, et al. Corneal tomographic features of postrefractive surgery ectasia. *J Biophotonics* 2019;12:e201800253.
26. Scarcelli G, Besner S, Pineda R, Kalout P, Yun SH. In vivo biomechanical mapping of normal and keratoconus corneas. *JAMA Ophthalmol* 2015;133:480-482.
27. Dupps WJ, Jr., Santhiago MR. Structural relationships in post-refractive surgery ectasia: What have we learned? *J Cataract Refract Surg* 2019;45:391-393.
28. Salomao MQ, Hofling-Lima AL, Gomes Esporcatte LP, et al. The Role of Corneal Biomechanics for the Evaluation of Ectasia Patients. *Int J Environ Res Public Health* 2020;17.

29. Chong J, Dupps WJ, Jr. Corneal biomechanics: Measurement and structural correlations. *Exp Eye Res* 2021;205:108508.
30. Randleman JB, Woodward M, Lynn MJ, Stulting RD. Risk assessment for ectasia after corneal refractive surgery. *Ophthalmology* 2008;115:37-50.
31. Bohac M, Koncarevic M, Pasalic A, et al. Incidence and Clinical Characteristics of Post LASIK Ectasia: A Review of over 30,000 LASIK Cases. *Semin Ophthalmol* 2018;33:869-877.
32. Moshirfar M, Albarracin JC, Desautels JD, Birdsong OC, Linn SH, Hoopes PC, Sr. Ectasia following small-incision lenticule extraction (SMILE): a review of the literature. *Clin Ophthalmol* 2017;11:1683-1688.
33. Kachanov AB, Nikulin S, Churakov T, Bauer SM, Kornikov VV, Zimin BA. Corneal ectasia after 10,000 ReLEx SMILE operations: 37 th CONGRESS OF THE ESCRS PROGRAMME 14–18 September 2019. 2019.
34. Sinha Roy A, Shetty R. Ectasia After SMILE: Correct Interpretation of Biomechanical Hypothesis. *J Refract Surg* 2017;33:66.
35. Herber R, Francis M, Spoerl E, Pillunat LE, Raiskup F, Sinha Roy A. Comparison of waveform-derived corneal stiffness and stress-strain extensometry-derived corneal stiffness using different cross-linking irradiances: an experimental study with air-puff applanation of ex vivo porcine eyes. *Graefes Arch Clin Exp Ophthalmol* 2020;258:2173-2184.

36. Spoerl E, Huhle M, Seiler T. Induction of cross-links in corneal tissue. *Exp Eye Res* 1998;66:97-103.
37. Wollensak G, Spoerl E, Seiler T. Riboflavin/ultraviolet-a-induced collagen crosslinking for the treatment of keratoconus. *Am J Ophthalmol* 2003;135:620-627.
38. Vinciguerra P, Camesasca FI, Albe E, Trazza S. Corneal collagen cross-linking for ectasia after excimer laser refractive surgery: 1-year results. *J Refract Surg* 2010;26:486-497.
39. Yildirim A, Cakir H, Kara N, et al. Corneal collagen crosslinking for ectasia after laser in situ keratomileusis: long-term results. *J Cataract Refract Surg* 2014;40:1591-1596.
40. Spoerl E, Mrochen M, Sliney D, Trokel S, Seiler T. Safety of UVA-riboflavin cross-linking of the cornea. *Cornea* 2007;26:385-389.
41. Wernli J, Schumacher S, Spoerl E, Mrochen M. The Efficacy of Corneal Cross-Linking Shows a Sudden Decrease with Very High Intensity UV Light and Short Treatment Time. *Investigative Ophthalmology & Visual Science* 2013;54:1176-1180.
42. Mazzotta C, Hafezi F, Kymionis G, et al. In Vivo Confocal Microscopy after Corneal Collagen Crosslinking. *Ocul Surf* 2015;13:298-314.
43. Sinha Roy A, Dupps WJ, Jr. Patient-specific computational modeling of keratoconus progression and differential responses

- to collagen cross-linking. *Invest Ophthalmol Vis Sci* 2011;52:9174-9187.
44. Center MUM, Research ZTNOfH, Development. Efficacy of Customized Corneal Cross-linking vs. Standard Corneal Cross-linking. <https://ClinicalTrials.gov/show/NCT04532788>; 2021.
  45. Seiler TG, Fischinger I, Koller T, Zapp D, Frueh BE, Seiler T. Customized Corneal Cross-linking: One-Year Results. *Am J Ophthalmol* 2016;166:14-21.
  46. Nordstrom M, Schiller M, Fredriksson A, Behndig A. Refractive improvements and safety with topography-guided corneal crosslinking for keratoconus: 1-year results. *Br J Ophthalmol* 2017;101:920-925.
  47. Cassagne M, Pierre K, Galiacy SD, Asfaux-Marfaing MP, Fournie P, Malecaze F. Customized Topography-Guided Corneal Collagen Cross-linking for Keratoconus. *J Refract Surg* 2017;33:290-297.
  48. Shetty R, Pahuja N, Roshan T, et al. Customized Corneal Cross-linking Using Different UVA Beam Profiles. *J Refract Surg* 2017;33:676-682.
  49. Scarcelli G, Yun SH. Confocal Brillouin microscopy for three-dimensional mechanical imaging. *Nat Photonics* 2007;2:39-43.
  50. De Vicente J. *Viscoelasticity: From Theory to Biological Applications*: BoD—Books on Demand; 2012.
  51. Roberts CJ, Mahmoud AM, Bons JP, et al. Introduction of Two Novel Stiffness Parameters and Interpretation of Air Puff-



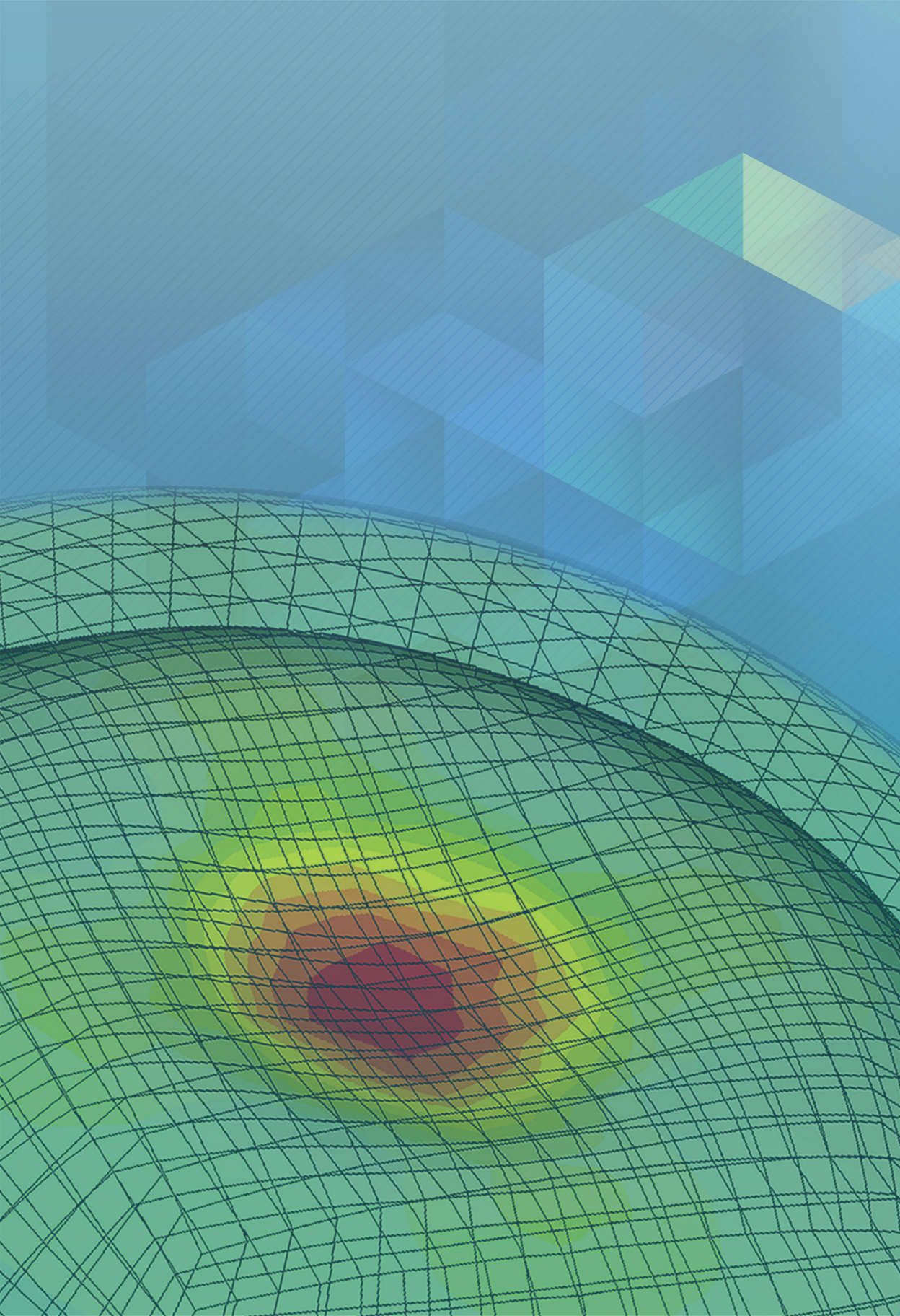
- Induced Biomechanical Deformation Parameters With a Dynamic Scheimpflug Analyzer. *J Refract Surg* 2017;33:266-273.
52. Hoeltzel DA, Altman P, Buzard K, Choe K. Strip extensimetry for comparison of the mechanical response of bovine, rabbit, and human corneas. *J Biomech Eng* 1992;114:202-215.
  53. Luce DA. Determining in vivo biomechanical properties of the cornea with an ocular response analyzer. *J Cataract Refract Surg* 2005;31:156-162.
  54. Pallikaris I, Tsilimbaris MK, Dastiridou AI. Ocular Rigidity, Biomechanics and Hydrodynamics of the Eye. Springer.
  55. Terai N, Raiskup F, Haustein M, Pillunat LE, Spoerl E. Identification of biomechanical properties of the cornea: the ocular response analyzer. *Curr Eye Res* 2012;37:553-562.
  56. Ruisenor Vazquez PR, Delrivo M, Bonthoux FF, Pfortner T, Galletti JG. Combining ocular response analyzer metrics for corneal biomechanical diagnosis. *J Refract Surg* 2013;29:596-602.
  57. Esporcatte LPG, Salomao MQ, Lopes BT, et al. Biomechanical diagnostics of the cornea. *Eye Vis (Lond)* 2020;7:9.
  58. Pinero DP, Alcon N. In vivo characterization of corneal biomechanics. *J Cataract Refract Surg* 2014;40:870-887.
  59. Dupps WJ, Jr. Hysteresis: new mechanospeak for the ophthalmologist. *J Cataract Refract Surg* 2007;33:1499-1501.

60. Glass DH, Roberts CJ, Litsky AS, Weber PA. A viscoelastic biomechanical model of the cornea describing the effect of viscosity and elasticity on hysteresis. *Invest Ophthalmol Vis Sci* 2008;49:3919-3926.
61. Sinha Roy A, Kurian M, Matalia H, Shetty R. Air-puff associated quantification of non-linear biomechanical properties of the human cornea in vivo. *J Mech Behav Biomed Mater* 2015;48:173-182.
62. Ambrosio R, Jr., Lopes BT, Faria-Correia F, et al. Integration of Scheimpflug-Based Corneal Tomography and Biomechanical Assessments for Enhancing Ectasia Detection. *J Refract Surg* 2017;33:434-443.
63. Jędzierowska M, Koprowski R. Corvis ST tonometer and the possibility of analysing corneal deformation dynamics during intraocular pressure measurement. *Air-Puff Tonometers Challenges and insights IOP Publishing Ltd* 2019.
64. Koprowski R. *Image analysis for ophthalmological diagnosis*: Springer; 2016.
65. Matalia J, Francis M, Tejwani S, Dudeja G, Rajappa N, Sinha Roy A. Role of Age and Myopia in Simultaneous Assessment of Corneal and Extraocular Tissue Stiffness by Air-Puff Applanation. *J Refract Surg* 2016;32:486-493.
66. Yu JG, Bao FJ, Feng YF, et al. Assessment of corneal biomechanical behavior under posterior and anterior pressure. *J Refract Surg* 2013;29:64-70.

67. Leão E, Ing Ren T, Lyra JM, et al. Corneal deformation amplitude analysis for keratoconus detection through compensation for intraocular pressure and integration with horizontal thickness profile. *Computers in biology and medicine* 2019;109:263-271.
68. Joda AA, Shervin MM, Kook D, Elsheikh A. Development and validation of a correction equation for Corvis tonometry. *Comput Methods Biomech Biomed Engin* 2016;19:943-953.
69. Vinciguerra R, Ambrosio R, Jr., Elsheikh A, et al. Detection of Keratoconus With a New Biomechanical Index. *J Refract Surg* 2016;32:803-810.
70. Özkaya N, Goldsheyder D, Leger D, Nordin M. Fundamentals of Biomechanics : Equilibrium, Motion, and Deformation. Cham: Springer International Publishing : Imprint: Springer,; 2017:1 online resource (XV, 454 pages).
71. Han Z, Tao C, Zhou D, et al. Air puff induced corneal vibrations: theoretical simulations and clinical observations. *J Refract Surg* 2014;30:208-213.
72. Pahuja N, Kumar NR, Francis M, et al. Correlation of Clinical and Biomechanical Outcomes of Accelerated Crosslinking (9 mW/cm<sup>2</sup>) in 10 minutes) in Keratoconus with Molecular Expression of Ectasia-Related Genes. *Curr Eye Res* 2016;41:1419-1423.
73. Shroff R, Francis M, Pahuja N, Veebooy L, Shetty R, Sinha Roy A. Quantitative Evaluation of Microdistortions in Bowman's

- Layer and Corneal Deformation after Small Incision Lenticule Extraction. *Transl Vis Sci Technol* 2016;5:12.
74. Matalia J, Francis M, Gogri P, Panmand P, Matalia H, Sinha Roy A. Correlation of Corneal Biomechanical Stiffness With Refractive Error and Ocular Biometry in a Pediatric Population. *Cornea* 2017;36:1221-1226.
75. Kobayashi AS, Woo SL, Lawrence C, Schlegel WA. Analysis of the corneo-scleral shell by the method of direct stiffness. *J Biomech* 1971;4:323-330.
76. Woo SL, Kobayashi AS, Schlegel WA, Lawrence C. Nonlinear material properties of intact cornea and sclera. *Exp Eye Res* 1972;14:29-39.
77. Pinsky PM, Datye DV. A microstructurally-based finite element model of the incised human cornea. *J Biomech* 1991;24:907-922.
78. Kling S, Bekesi N, Dorronsoro C, Pascual D, Marcos S. Corneal viscoelastic properties from finite-element analysis of in vivo air-puff deformation. *PLoS One* 2014;9:e104904.
79. Jannesari M, Kadkhodaei M, Mosaddegh P, Kasprzak H, Behrouz MJ. Assessment of corneal and fatty tissues biomechanical response in dynamic tonometry tests by using inverse models. *Acta of bioengineering and biomechanics* 2018;20.
80. Lago MA, Ruperez MJ, Martinez-Martinez F, et al. A new methodology for the in vivo estimation of the elastic constants

- that characterize the patient-specific biomechanical behavior of the human cornea. *J Biomech* 2015;48:38-43.
81. Pandolfi A, Manganiello F. A model for the human cornea: constitutive formulation and numerical analysis. *Biomech Model Mechanobiol* 2006;5:237-246.
  82. Pinsky PM, van der Heide D, Chernyak D. Computational modeling of mechanical anisotropy in the cornea and sclera. *J Cataract Refract Surg* 2005;31:136-145.
  83. Studer H, Larrea X, Riedwyl H, Buchler P. Biomechanical model of human cornea based on stromal microstructure. *J Biomech* 2010;43:836-842.
  84. Nguyen TD, Boyce BL. An inverse finite element method for determining the anisotropic properties of the cornea. *Biomech Model Mechanobiol* 2011;10:323-337.
  85. Petsche SJ, Pinsky PM. The role of 3-D collagen organization in stromal elasticity: a model based on X-ray diffraction data and second harmonic-generated images. *Biomech Model Mechanobiol* 2013;12:1101-1113.
  86. Bergstrom JS. *Mechanics of solid polymers: theory and computational modeling*: William Andrew; 2015.





## Chapter 2

---

# Waveform analysis of deformation amplitude and deflection amplitude in normal, suspect, and keratoconic eyes

Francis M, Pahuja N, Shroff R, Gowda R, Matalia H, Shetty R, Remington Nelson EJ, Sinha Roy A

J Cataract Refract Surg. 2017 Oct;43(10):1271-1280

This is a non-final version of an article published in final form in Francis, Mathew MTech; Pahuja, Natasha MD; Shroff, Rushad MD; Gowda, Roshan MD; Matalia, Himanshu MD; Shetty, Rohit MD, PhD, FRCS; Nelson, Everette J. Remington PhD; Roy, Abhijit Sinha PhD\*. Waveform analysis of deformation amplitude and deflection amplitude in normal, suspect, and keratoconic eyes. Journal of Cataract & Refractive Surgery 43(10):p 1271-1280, October 2017.

<https://doi.org/10.1016/j.jcrs.2017.10.012>

**Purpose:** To evaluate the performance of waveform-derived variables in distinguishing normal, suspect, and keratoconic eyes.

**Methods:** Scheimpflug tomography (Pentacam) and dynamic Scheimpflug analysis (Corvis ST) of 253 normal (253 patients) eyes and 205 keratoconic eyes (205 patients) were evaluated. Among the 205 patients, 62 had keratoconus in 1 eye, while the unaffected eye was suspect. From deformation amplitude, deflection amplitude and whole-eye movement were extracted. A biomechanical model was used to derive a linear (kc [constant]) and nonlinear measure (kc [mean]) of corneal stiffness. Multivariate logistic regression was performed to determine sensitivity and specificity. The analysis was validated in another dataset of 59 normal, 45 suspect, and 160 keratoconic eyes.

**Results:** Deformation amplitude maximum, applanation 1 time and deformation amplitude, applanation 2 time, kc (constant), kc (mean), and deflection amplitude maximum were significantly different between normal and keratoconic eyes ( $P < .001$ ). The deformation characteristics of the suspect eyes were similar to those of the keratoconic eyes, particularly grade 1 ( $P > .05$ ). The kc (constant) and kc (mean) had the highest area under curve ( $>0.98$ ), sensitivity, and specificity greater than 90% and 91%, respectively. Logistic regression using kc (constant) and kc (mean) improved the area to 1.0, with a sensitivity and specificity equal to 99.6% and 100%, respectively. In the



validation dataset, the same cutoff yielded a sensitivity, specificity, and accuracy of 99.5%, 100%, and 99.6%, respectively.

**Conclusion:** Corneal stiffness and waveform analyses could be reliable differentiators of suspect and keratoconic eyes from normal eyes.

## Introduction

Noncontact air-puff applanation is commonly used to measure intraocular pressure (IOP).<sup>1</sup> With this method, an air puff of short duration (~30 milliseconds) is applied to the cornea. The air pressure at which the cornea becomes flat can be correlated with the IOP of the eye.<sup>2</sup> Because this process also involves mechanical deformation, new devices have been designed to quantify this deformation as a measure of the biomechanical status of the cornea. The dynamic bidirectional applanation device (Ocular Response Analyzer, Reichert Technologies) was the first to quantify this deformation using indices such as corneal hysteresis (CH) and corneal resistance factor (CRF).<sup>3</sup> In keratoconus, biomechanical decompensation of the cornea is indicated by the dynamic bidirectional applanation device.<sup>3</sup> However, the device does not indicate biomechanical stiffening conclusively after corneal crosslinking (CXL) in keratoconus with manufacturer-specified and waveform-derived custom variables.<sup>4, 5</sup> This highlights the need for direct mechanical quantification of corneal deformation.<sup>6</sup>

The Corvis ST (Oculus Optikgeräte GmbH), a dynamic Scheimpflug analyzer, is another applanation device capable of quantifying the deformation of the cornea.<sup>6</sup> The device reports the deformation as mechanical displacement using high-speed Scheimpflug imaging, which is unlike the indirect indices, that is CH and CRF, used by the dynamic bidirectional applanation device.<sup>6</sup> Recent studies with

the dynamic Scheimpflug analyzer have also showed increased compliance of the cornea in keratoconus.<sup>7-9</sup> However, the current device does not report corneal stiffness exclusive of the extra-corneal tissue stiffness.<sup>10</sup> This would require decomposition of the deformation amplitude signal as a summation of the deflection amplitude and whole-eye movement.<sup>10, 11</sup> This is important because the kinetic energy of the air puff is absorbed by the cornea and the extra-corneal tissues (including sclera, fat, and muscle).

To analyze the decomposition of the deformation amplitude signal, new indices were derived from waveform analyses of the deflection amplitude and whole-eye movement in this study. These indices were subsequently applied to a cohort of normal and keratoconic eyes, and a classification scale was developed. A subset of the patients had clinical features of keratoconus in 1 eye and a tomographically normal fellow eye. These eyes were analyzed as a separate cohort since keratoconus is bilateral in many patients but its progression can be highly asymmetric between the eyes of a patient.<sup>12-14</sup> Thus, it is possible that the tomographically normal eye may progress to keratoconus in the future.<sup>12-14</sup> The classification scale based on these new indices was subsequently validated in another cohort of normal and keratoconus eyes.

## Methods

This retrospective observational cross-sectional study of patient records was approved by the ethics committee of Narayana Nethralaya Multispecialty Eye Hospital, Bangalore, India. It was conducted in accordance with the tenets of the Declaration of Helsinki. Two hundred fifty-three normal eyes (253 patients) and 205 keratoconic eyes (205 patients) were used initially as a training database to develop a diagnostic scale. Grading of the severity of keratoconus was based on mean keratometry (K), as described previously.<sup>15</sup> A mean K less than 48.0 diopters (D) was considered grade 1, less than 52.0 D but greater than 48.0 D grade 2, and greater than 52.0 D grade 3. Of the keratoconic eyes, 110 eyes, 56 eyes, and 39 eyes had a severity grade of 1, 2, and 3, respectively. One eye per patient was randomly selected for the study. In a few keratoconic patients, only 1 eye was affected with keratoconus and the fellow eye was tomographically normal on evaluation with slitlamp and Scheimpflug tomography. Keratoconus is usually a bilateral disease, so the fellow eye could progress to keratoconus over time.<sup>12-14</sup> Since keratoconus progression can take decades and the fellow eye was topographically normal at the time of examination, these fellow eyes (a subset of 62 eyes of 62 patients from the 205 keratoconic patients) were classified as suspect eyes for further analyses. All eyes had slitlamp examination and corneal Scheimpflug tomography measurement (Pentacam, Oculus Optikgeräte GmbH).

## Waveform analysis of normal, suspect, and keratoconic eyes

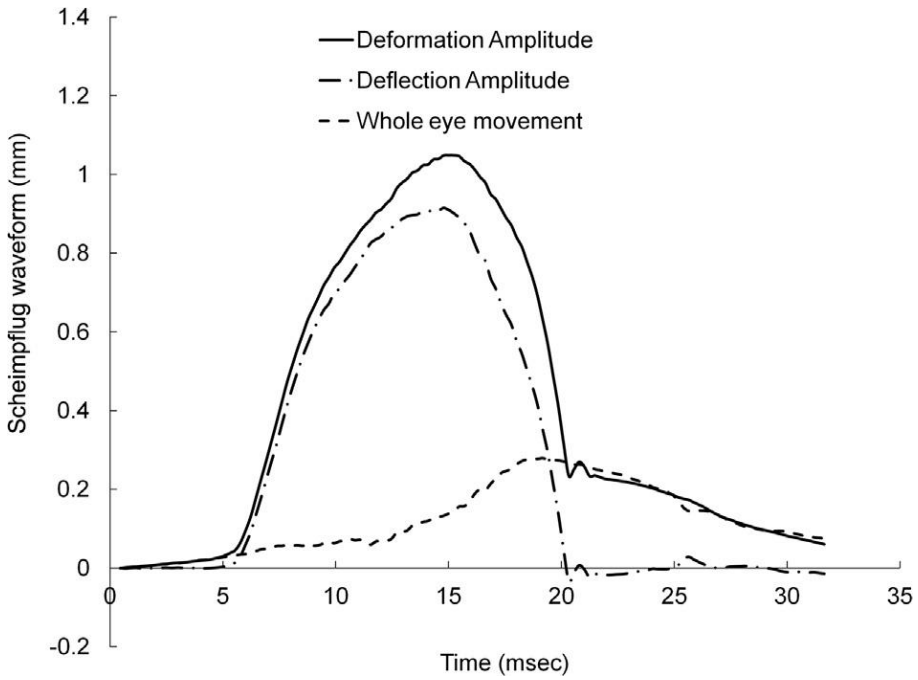


Figure 1: An overlay of deformation amplitude, deflection amplitude, and whole-eye movement.

Eyes with no clinical signs of keratoconus, such as Fleischer ring, Vogt striae, scissoring of the red reflex, an abnormal retinoscopy, thin corneas, and curvature asymmetry causing abnormal corneal astigmatism, were classified as normal. All the normal eyes had refractive surgery for myopia and stable refractive outcomes for 1 year. Eyes with corneal steepening, stromal thinning, asymmetric astigmatism, corneal scarring, and abnormal topography (asymmetric astigmatism, focal steepening) were classified as keratoconic. Exclusion

criteria were prior corneal surgery, ocular surgery, contact lens use, autoimmune disorders, pregnancy, corneal scarring, and allergy.

All eyes had biomechanical evaluation with the dynamic Scheimpflug analyzer. The dynamic Scheimpflug analyzer imaged a cross-section of the cornea along the horizontal meridian during deformation using a high-speed Scheimpflug camera to capture 140 frames of the deforming cornea over 30 milliseconds. After the measurement was completed, the dynamic Scheimpflug analyzer reported the displacement of the corneal apex along the segmented anterior corneal edge as the deformation amplitude (in millimeters). Deformation amplitude is the sum of the deflection amplitude and the whole-eye movement.<sup>10, 11</sup> The device also allowed export of the coordinates of the segmented anterior corneal edge as a comma-separated value (CSV) file. By a simple image-analysis procedure, the 2 deformations were extracted from deformation amplitude.<sup>10, 11</sup> The displacement of the detected points at the end of the anterior corneal edge were computed from the CSV file and used as whole-eye movement.<sup>10</sup> By subtracting this deformation from deformation amplitude, the deflection amplitude was computed. Figure 1 shows an overlay of deflection amplitude and whole-eye movement on deformation amplitude of a patient eye.

In a recent study, a viscoelastic model for the measured waveforms was described.<sup>16</sup> Mathematical representation of the model is as follows:

$$F_{\text{air-puff}} = kc(u_1 - u_2) + kg(u_2) + \mu g\left(\frac{du_2}{dt}\right) \quad (1)$$

In equation 1,  $kc(u_1 - u_2)$  was the portion of air-puff force absorbed by the cornea, which will be referred to as the corneal force.

In equation 1,  $kg(u_2) + \mu g\left(\frac{du_2}{dt}\right)$  was the portion of the air-puff force absorbed by the extra-corneal tissue, which will be referred to as the extra-corneal tissue force. The term *extra corneal* was used to describe the noncorneal contribution to the deformation amplitude. Equation 1 is a modification of another model, which did not delineate the explicit contribution of deflection amplitude and whole-eye movement.<sup>17</sup> In equation 1,  $F_{\text{air-puff}}$  was the force applied by the dynamic Scheimpflug analyzer air puff,  $kc$  was the corneal stiffness,  $kg$  was the extra-ocular tissue stiffness, and  $\mu g$  was the extra-corneal tissue viscosity. The variable  $u_1$  was deformation amplitude as a function of time.<sup>11, 16</sup>

Similarly,  $u_2$  was the whole eye movement as a function of the time.<sup>11,</sup>

<sup>16</sup> The difference between  $u_1$  and  $u_2$  was the deflection amplitude.<sup>11, 16</sup>

The time rate of change of  $u_2$  ( $\frac{du_2}{dt}$ ) was necessary to model the delay in the whole-eye movement similar to viscous dissipation.

Two variants of equation 1 were solved, one in which  $k_c$  was a constant and a second in which  $k_c$  was assumed to be an air-puff pressure ( $P_{\text{air-puff}}$ ) dependent parameter:

$$k_c = \beta e^{\alpha P_{\text{air-puff}}} \quad (2)$$

In equation 2,  $\beta$  and  $\alpha$  were coefficients that described the exponential increase in corneal stiffness with an increase in air-puff pressure. Thus, the first variant of equation 1 approximated the cornea as a linear material (or  $\alpha$  was set to zero), whereas the second approximated it as a nonlinear material in which the cornea progressively stiffened as the stress increased during an increase in the air-puff pressure.<sup>10</sup> In the previous study, finite-element simulations showed a local increase in stress and strain in the central cornea during applanation.<sup>10</sup> This indicated a probable increase in corneal stiffness with increasing air-puff pressure and vice versa because the cornea naturally stiffens with an increase in induced stress. Neither stress nor strain can be estimated by equation 2. Hence,  $k_c$  was modeled as a function of air-puff pressure (equation 2) as it had a direct correlation with variation in stress and strain during deformation. The  $P_{\text{air-puff}}$  was the pressure applied by the dynamic Scheimpflug analyzer on the anterior corneal surface.



## Waveform analysis of normal, suspect, and keratoconic eyes

- Deformation amplitude maximum (mm): Maximum magnitude of deformation amplitude
- Applanation 1 Deformation Amplitude (mm): Deformation at first applanation
- Applanation 1 Time (msec): Time of first applanation
- Applanation 2 Deformation Amplitude (mm): Deformation at second applanation
- Applanation 2 Time (msec): Time of second applanation
- $k_c$  (constant; N/m): Corneal stiffness from the first version of equation 1
- $k_c$  (mean; N/m): Arithmetic average of corneal stiffness calculated from second version of equation 1 for a range of deformation pressures ranging from 0 to 180 mm Hg
- $k_g$  (N/m): Extra-corneal tissue stiffness
- $\mu g$  (Pa.s): Extra-corneal tissue viscosity
- Ratio of normalized  $k_c$  (constant) to  $k_g$ : Because keratoconus eyes varied in thickness,  $k_c$  of each cornea was normalized with its respective CCT to define its unit thickness stiffness. The ratio of normalized  $k_c$  (constant) to  $k_g$  was calculated to evaluate the relative changes in corneal and extra-corneal tissue stiffness with increasing severity of keratoconus.
- Ratio of normalized  $k_c$  (mean) to  $k_g$ : Normalization of  $k_c$  was performed similar to the method described above.
- Ratio of maximum corneal force to maximum extra-corneal tissue force: Similar to the concept described above, this ratio described the relative amount of force absorbed by the cornea to the force absorbed by the extra-corneal tissues.
- Ratio of mean corneal force to mean extra-corneal tissue force
- Deflection amplitude maximum (mm)
- Whole-eye movement maximum (mm)
- Ratio of deflection amplitude maximum to whole-eye movement maximum

Figure 2: Biomechanical variables analyzed in the study (CCT = central corneal thickness).

Computational fluid dynamics simulations of the air puff showed that the positive-pressure air jet immediately in front of the cornea was almost 2.5 mm in diameter.<sup>10</sup> By multiplying the cross-sectional area of the air jet ( $\pi \times 2.5 \times 2.5$ ) with  $P_{\text{air-puff}}$ ,  $F_{\text{air-puff}}$  was calculated. In equation 1, air pressure at the nozzle was used directly. In our previous study,<sup>10</sup> the magnitude of air pressure at the corneal surface was compared to the air pressure measured inside the nozzle with computational fluid dynamics simulations. The magnitude of the 2 pressures was almost the same. For the sake of simplicity, the nozzle air-puff pressure was used as was reported by the device and additional computational fluid dynamics simulations were not required to solve equation 1. Both equations 1 and 2 were solved simultaneously using the Newton-Raphson method (Mathworks, Inc.). Solving equations 1 and 2 provided the stiffness and viscosity unique to the tested eye. These values were used in equations 1 and 2 along with the measured waveforms (Figure 1) to calculate the predicted force ( $f_{\text{air-puff}}$ ) acting on the corneal surface. The root mean square error (RMSE) of difference between  $f_{\text{air-puff}}$  and  $F_{\text{air-puff}}$  was used as the optimized function for the Newton-Raphson method, where  $n$  was the number of time points:

$$RMSE = \sqrt{\frac{\sum(f_{\text{air-puff}} - F_{\text{air-puff}})^2}{n}} \quad (3)$$

Figure 2 shows the biomechanical variables that were analyzed. Several other variables were also analyzed. The K1 (flat axis), K2 (steep axis), mean K (mean of K1 and K2), and maximum K were compared between

normal, suspect, and grades of keratoconus. Axial and tangential cone location magnitude index (CLMI) of the anterior and posterior surfaces were also compared.<sup>18</sup> Patient demographics included age, IOP, central corneal thickness (CCT), minimum corneal thickness, and spherical equivalent (SE). The new indices, corneal biomechanical index<sup>18</sup> (CBI) and total biomechanical index (TBI), were also derived from a new analysis software that combined dynamic Scheimpflug analyzer waveforms (Corvis ST, version 1.03r1476) and Scheimpflug tomography (Pentacam, version 1.20r98). The CBI is a composite measure of several indices reported by the Corvis ST.<sup>11</sup> As per the manufacturer, TBI combines tomography indices and CBI to improve the detection of keratoconus.

In addition to the training dataset, a validation dataset of normal, fellow eyes, and keratoconus eyes was compiled from the clinical database of the hospital. All the normal eyes had refractive surgery for myopia and had stable refractive outcomes for a year. A statistical model for classification of the disease was derived from the training dataset. This model was applied to the validation dataset. The sensitivity, specificity, and accuracy of the statistical model were calculated with the validation dataset.

*Statistical Analyses*

All variables (CLMI and biomechanical) were evaluated for normality of distribution. If normally distributed, the group means with the standard error of the mean were calculated. The analysis of covariance (ANCOVA), with IOP and CCT as covariates, was used to assess the difference between normal, suspect, and grades of keratoconus. Corrected IOP was derived from dynamic Scheimpflug analyzer software. The analysis of covariance uses a multivariate generalized linear model to estimate adjusted values of the dependent variable, for example deformation amplitude. These adjusted variables from ANCOVA analyses were further analyzed with receiver-operator characteristics (ROC). Cutoff, area under the curve (AUC), sensitivity, and specificity of the top 4 biomechanical variables were evaluated. Stepwise logistic regression was also used to determine whether a linear combination of the top 4 variables could be used to distinguish between normal, suspect, and keratoconus eyes. The suspect eyes were included in the keratoconic eye group for ROC and logistic regression analyses, with the assumption that these eyes could progress to keratoconus.<sup>12-14</sup>

**Results**

Table 1 summarizes the demographics of the normal, suspect, and keratoconic eyes. Age and IOP were significantly different between normal and disease groups ( $P < .001$ ), but the differences were clinically

insignificant. The mean CCT and mean minimum corneal thickness were significantly different between all the groups (normal, suspect eyes, and grades of keratoconic eyes) ( $P < .001$ ). The mean K2 and maximum K were similar between normal and suspect groups, but varied between keratoconic groups ( $P < .001$ ). The mean K1 of normal, suspect, and grade 1 keratoconic eyes were similar ( $P > .05$ ), but significantly lower than the mean K1 of grades 2 and 3 keratoconus eyes ( $P < .001$ ). The SE of normal eyes was similar to that of grade 2 keratoconic eyes ( $P > .05$ ). Similarly, SE of suspect eyes and grade 1 keratoconic eyes were similar ( $P > .05$ ) and significantly lower in magnitude than in normal eyes ( $P < .001$ ). The highest mean SE was in grade 3 keratoconic eyes ( $P < .001$ ). The anterior and posterior surface mean CLMI were similar in normal and suspect eyes ( $P > .05$ ) but lower than the mean CLMI of keratoconus grades ( $P < .001$ ). The mean CLMI was significantly different between grades 1, 2, and 3 keratoconic eyes when they were compared pairwise ( $P < .001$ ).

Table 1: Demographics of study groups in the training data set.

Demographic	Normal eyes (n=253)	Fellow eyes (n=62)
Age (years)	26 ± 1	23 ± 1
IOP (mmHg)	16.96 ± 0.13	16.14 ± 0.17
Central corneal thickness (µm)	532.51 ± 1.6	511.65 ± 4.16
Minimum corneal thickness (µm)	528.37 ± 1.81	504.93 ± 4.42
K1 (D)	43.33 ± 0.11	43.34 ± 0.17
K2 (D)	44.46 ± 0.11	44.37 ± 0.15
Kmean (D)	43.89 ± 0.11	43.84 ± 0.15

Kmax (D)	44.96 ± 0.11	45.23 ± 0.19
Spherical equivalent (D)	-4.32 ± 0.17	-1.28 ± 0.31
Axial CLMI anterior (D)	0.76 ± 0.05	1.12 ± 0.11
Axial CLMI posterior (D)	0.2 ± 0.02	0.36 ± 0.04
Tangential CLMI anterior (D)	2.18 ± 0.12	2.64 ± 0.26
Tangential CLMI posterior (D)	0.41 ± 0.04	0.63 ± 0.05
Corvis Biomechanical Index (CBI)	0.12 ± 0.01	0.58 ± 0.05
Tomographic Biomechanical Index (TBI)	0.32 ± 0.02	0.83 ± 0.04

Table 1: continued

Keratoconus Grade 1 (n = 110)	Keratoconus Grade 2 (n = 56)	Keratoconus Grade 3 (n = 39)	p-value
25 ± 1	24 ± 1	23 ± 1	<0.001*
15.83 ± 0.16	15.78 ± 0.22	15.65 ± 0.33	<0.001*
487.65 ± 3.37	460.3 ± 4.07	418.18 ± 6.53	<0.001*
476.94 ± 3.4	448.27 ± 4.08	408.26 ± 6.42	<0.001*
43.79 ± 0.14	46.97 ± 0.21	53.33 ± 0.67	<0.001*
46.54 ± 0.21	51.92 ± 0.3	58.81 ± 0.71	<0.001*
45.1 ± 0.15	49.29 ± 0.18	55.91 ± 0.66	<0.001*
50.09 ± 0.37	57.86 ± 0.57	66.76 ± 0.94	<0.001*
-1.83 ± 0.22	-4.33 ± 0.53	-8.39 ± 1.2	<0.001*
5.41 ± 0.47	7.59 ± 0.76	9.55 ± 0.56	<0.001*
1.39 ± 0.1	1.62 ± 0.15	2.42 ± 0.17	<0.001*
7.3 ± 0.45	11.39 ± 0.76	16.6 ± 1.03	<0.001*
1.68 ± 0.09	2.42 ± 0.15	3.5 ± 0.24	<0.001*
0.78 ± 0.03	0.93 ± 0.03	0.9 ± 0.05	<0.001*
0.92 ± 0.02	0.97 ± 0.02	0.89 ± 0.05	<0.001*

CLMI = cone location magnitude indices; IOP = intraocular pressure;  
K1 = flat axis keratometry; K2 = steep axis keratometry; Kmax =

Waveform analysis of normal, suspect, and keratoconic eyes

maximum keratometry; Kmean = mean keratometry; \* Statistically significant difference

Table 2: Adjusted biomechanical parameters reported by dynamic Scheimpflug analyzer for the training dataset eyes.

	Normal eyes (n=253)	Fellow eyes (n=62)
Deformation amplitude maximum (mm)	1.08 ± 0.01	1.18 ± 0.02
Applanation 1 Deformation Amplitude (mm)	0.12 ± 0.001	0.116 ± 0.002*
Applanation 1 Time (msec)	7.55 ± 0.02	7.20 ± 0.01
Applanation 2 Deformation Amplitude (mm)	0.38 ± 0.004	0.39 ± 0.01
Applanation 2 Time (msec)	21.4 ± 0.02	21.67 ± 0.03*
RMSE (N)	4.19×10 <sup>-3</sup> ± 7.58×10 <sup>-4</sup>	3.59×10 <sup>-3</sup> ± 1.04×10 <sup>-4</sup>

Table 2: continued

Keratoconus Grade 1 (n=110)	Keratoconus Grade 2 (n=56)	Keratoconus Grade 3 (n=39)	p-value
1.16 ± 0.01	1.19 ± 0.02	1.26 ± 0.02	<0.001*
0.119 ± 0.001	0.125 ± 0.002	0.131 ± 0.003*	<0.001*
7.19 ± 0.001*	7.20 ± 0.01	7.15 ± 0.02*	<0.001*
0.37 ± 0.006	0.39 ± 0.009	0.40 ± 0.01	0.16
21.58 ± 0.02	21.59 ± 0.04	21.63 ± 0.05	<0.001*

Chapter 2

$3.76 \times 10^{-3} \pm 1.22 \times 10^{-4}$	$3.64 \times 10^{-3} \pm 7.9 \times 10^{-5}$	$3.84 \times 10^{-3} \pm 1.35 \times 10^{-4}$	<0.001*
---	--	---	---------

RMSE = root mean square error of calculation; Means  $\pm$  SD;

\*Statistically significant difference

Table 3: Adjusted biomechanical parameters of the training dataset eyes.

	Grouping based on Diagnosis	
	Normal (n=253)	Fellow eyes (n=62)
kc (constant) (N/m)	107.83 $\pm$ 0.78	100.79 $\pm$ 1.27
kc (mean) (N/m)	106.37 $\pm$ 0.98	96.8 $\pm$ 1.6
kg (N/m)	69.57 $\pm$ 2.23	68.25 $\pm$ 3.68
$\mu$ g (Pa.s)	0.37 $\pm$ 0.01	0.38 $\pm$ 0.02
Ratio of kc (mean) to kg normalized with CCT	3.69 $\pm$ 0.15	2.9 $\pm$ 0.25
Ratio of kc (linear) to kg normalized with CCT	3.76 $\pm$ 0.15	3.04 $\pm$ 0.25
Ratio of maximum corneal force to maximum extra-corneal tissue force	5 $\pm$ 0.14	4.37 $\pm$ 0.24
Ratio of mean corneal force to mean extra-corneal tissue force	6.96 $\pm$ 0.19	5.81 $\pm$ 0.32
Deflection amplitude maximum (mm)	0.96 $\pm$ 9.05 $\times 10^{-3}$	1.01 $\pm$ 1.5 $\times 10^{-2}$
Whole eye movement maximum (mm)	0.25 $\pm$ 7.06 $\times 10^{-3}$	0.28 $\times 10^{-1} \pm 1.17 \times 10^{-2}$



Waveform analysis of normal, suspect, and keratoconic eyes

Ratio of deflection amplitude to whole eye movement maximum	$4.38 \pm 0.16$	$4.5 \pm 0.27$
---	-----------------	----------------

Table 3: continued

Grouping based on Diagnosis			
KC Grade 1 (n=110)	KC Grade 2 (n=56)	KC Grade 3 (n=39)	P value
$101.88 \pm 0.99$	$98.71 \pm 1.48$	$96.35 \pm 2.04$	<0.001*
$97.94 \pm 1.24$	$95.62 \pm 1.86$	$92.61 \pm 2.55$	<0.001*
$71.75 \pm 2.89$	$70.2 \pm 4.26$	$66.82 \pm 5.83$	0.89
$0.41 \pm 0.02$	$0.39 \pm 0.02$	$0.35 \pm 0.03$	0.19
$3.05 \pm 0.19$	$3.01 \pm 0.29$	$2.84 \pm 0.4$	0.04*
$3.18 \pm 0.19$	$3.13 \pm 0.29$	$3 \pm 0.4$	0.07
$4.31 \pm 0.18$	$4.13 \pm 0.27$	$4.83 \pm 0.38$	0.005*
$5.57 \pm 0.25$	$5.22 \pm 0.37$	$5.5 \pm 0.51$	<0.001*
$0.99 \pm 1.15 \times 10^{-2}$	$1.02 \pm 1.71 \times 10^{-2}$	$1.09 \pm 2.37 \times 10^{-2}$	<0.001*
$0.26 \times 10^{-1} \pm 8.93 \times 10^{-3}$	$0.28 \times 10^{-1} \pm 1.33 \times 10^{-2}$	$0.26 \times 10^{-1} \pm 1.85 \times 10^{-2}$	0.09
$4.26 \pm 0.2$	$4.04 \pm 0.31$	$4.56 \pm 0.42$	0.71

CCT = central corneal thickness; kc = corneal stiffness; KC = keratoconus; kg = extra-corneal tissue stiffness;  $\mu g$  = extra-corneal tissue viscosity; \* Statistically significant difference

Table 4: Receiver-operating characteristic analyses of CLMI and select biomechanical parameters in training dataset eyes. Suspect eyes were included in the keratoconus population.

	Normal vs KC and FFKC			
	Area under the ROC curve	Cut-off	Sensitivity (%)	Specificity (%)
Axial CLMI anterior (D)	1.0 ± 0.0	1.02	100.0	100.0
Axial CLMI posterior (D)	1.0 ± 0.0	0.26	100.0	100.0
Tangential CLMI anterior (D)	1.0 ± 0.0	2.37	100.0	100.0
Tangential CLMI posterior (D)	1.0 ± 0.0	0.48	100.0	100.0
kc (constant) (N/m)	0.98 ± 0.005	104.74	92.9	93.4
kc (mean) (N/m)	0.97 ± 0.006	102.13	90.6	91.3
Ratio of maximum corneal force to maximum extra-corneal tissue force	0.58 ± 0.03	4.65	53.5	64.1
Deflection amplitude maximum (mm)	0.95 ± 0.009	0.986	85.7	91.1
Linear combination of kc (constant) and kc (mean)	1.0 ± 0.0	0.45	99.6	100.0

CLMI = cone location magnitude index; FFKC = forme fruste keratoconus; kc = corneal stiffness; KC = keratoconus

Table 5: Demographics of validation dataset eyes.

	Normal eyes (n=59)	Fellow eyes (n=45)
Age (years)	22 ± 1	24 ± 1
IOP (mmHg)	17.02 ± 0.19	16.38 ± 0.27
Central corneal thickness (µm)	529.82 ± 3.84	504.96 ± 4.4
Minimum corneal thickness (µm)	524.18 ± 3.9	495.67 ± 4.21
K1 (D)	43.42 ± 0.29	44.07 ± 0.27
K2 (D)	45.31 ± 0.29	46.01 ± 0.34
Kmean (D)	44.34 ± 0.27	45 ± 0.29
Kmax (D)	45.82 ± 0.34	48.08 ± 0.62
Spherical equivalent (D)	-2.05 ± 0.33	-2.21 ± 0.38
Axial CLMI anterior (D)	0.75 ± 0.07	2.83 ± 0.48
Axial CLMI posterior (D)	0.2 ± 0.02	0.83 ± 0.11
Tangential CLMI anterior (D)	1.73 ± 0.19	4.68 ± 0.71
Tangential CLMI posterior (D)	0.45 ± 0.07	1.1 ± 0.13
Corvis Biomechanical Index (CBI)	0.27 ± 0.04	0.65 ± 0.06
Tomographic Biomechanical Index (TBI)	0.5 ± 0.05	0.88 ± 0.03

Table 5: continued

Keratoconus Grade 1 (n = 85)	Keratoconus Grade 2 (n = 38)	Keratoconus Grade 3 (n = 37)	p-value
24 ± 1	22 ± 1	24 ± 1	0.42
16.56 ± 0.16	16.43 ± 0.23	14.86 ± 0.48	<0.001*
474.11 ± 3.57	443.7 ± 6.58	404.76 ± 6.51	<0.001*
462.14 ± 3.65	433.33 ± 6.6	395.91 ± 7.45	<0.001*

$43.99 \pm 0.15$	$47.44 \pm 0.23$	$54.91 \pm 0.88$	<0.001*
$47.2 \pm 0.22$	$51.89 \pm 0.31$	$59.38 \pm 0.88$	<0.001*
$45.53 \pm 0.16$	$49.55 \pm 0.22$	$57.03 \pm 0.86$	<0.001*
$51.04 \pm 0.36$	$56.83 \pm 0.53$	$68.08 \pm 1.74$	<0.001*
$-2.35 \pm 0.37$	$-3.26 \pm 0.35$	$-4.25 \pm 0.79$	0.01*
$6.03 \pm 0.44$	$6.5 \pm 0.77$	$9.97 \pm 1.36$	<0.001*
$1.34 \pm 0.09$	$1.41 \pm 0.1$	$2.3 \pm 0.2$	<0.001*
$8.5 \pm 0.51$	$10.89 \pm 0.82$	$17.97 \pm 1.51$	<0.001*
$1.8 \pm 0.1$	$2.14 \pm 0.12$	$3.48 \pm 0.31$	<0.001*
$0.88 \pm 0.03$	$0.94 \pm 0.04$	$0.92 \pm 0.05$	<0.001*
$0.98 \pm 0.02$	$1 \pm 0$	$0.92 \pm 0.06$	<0.001*

CLMI = cone location magnitude indices; IOP = intraocular pressure; K1 = Flat axis keratometry; K2 = Steep axis keratometry; Kmean = mean keratometry; Kmax = maximum keratometry; Means  $\pm$  standard error; \* Statistically significant

Table 6: Sensitivity, specificity, and accuracy of validation dataset.

	Normal vs KC and FFKC		
	Sensitivity (%)	Specificity (%)	Accuracy (%)
Axial CLMI anterior (D)	99.5	100	99.6
Axial CLMI posterior (D)	100	100	100
Tangential CLMI anterior (D)	100	100	100
Tangential CLMI posterior (D)	100	100	100
kc (constant) (N/m)	90.5	100	92.5
kc (mean) (N/m)	90.0	100	92.1

Waveform analysis of normal, suspect, and keratoconic eyes

Ratio of maximum corneal force to maximum extra-corneal tissue force	57.7	64.7	59.2
Deflection amplitude (mm)	90.0	94.1	90.8

CLMI = cone location magnitude indices; FFKC = forme fruste keratoconus; kc = corneal stiffness; KC = keratoconus

Table 2 shows the mean  $\pm$  SEM of some of the adjusted biomechanical variables directly reported by the dynamic Scheimpflug analyzer. The deformation amplitude maximum in suspect eyes and grade 1 and grade 2 keratoconic eyes was similar ( $P > .05$ ); the deformation amplitude in normal eyes was lower than that in all grades of keratoconic eyes ( $P < .001$ ). Similarly, the mean deformation amplitude of grade 3 keratoconus was significantly greater in grade 3 keratoconic eyes than in normal eyes and other grades of keratoconic eyes ( $P < .001$ ). The applanation 1 deformation amplitude was significantly lower in normal, suspect, and grade 1 keratoconic eyes than in grades 2 and 3 keratoconic eyes ( $P < .001$ ). The applanation 1 time was significantly greater in normal and suspect eyes than in grade 1 and grade 2 keratoconic eyes ( $P = .007$ ). The lowest applanation 1 time was in grade 3 keratoconic eyes ( $P < .001$ ). The applanation 2 deformation amplitude did not differ between the normal, suspect, and grades of keratoconic eyes ( $P = .16$ ). The mean applanation 2 time was significantly lower in normal eyes than in the other groups ( $P < .001$ ).

The mean RMSE was similar in suspect and grades of keratoconic eyes ( $P > .05$ ). The mean RMSE was significantly higher in normal eyes than in the grades of keratoconic eyes ( $P < .001$ ). The RMSE was around 0.4% of the force applied by the air puff.

Table 3 shows the mean  $\pm$  SEM of the adjusted biomechanical variables derived from the biomechanical model described by equations 1 and 2. The  $k_c$  (constant) and  $k_c$  (mean) were significantly greater in normal eyes than in suspect eyes and in grades of keratoconic eyes ( $P < .0001$ ). The  $k_g$  ( $P = .89$ ) and  $\mu g$  ( $P = .19$ ) were similar in normal, suspect, and grades of keratoconic eyes. There was no significant difference in the ratio of normalized  $k_c$  (constant) to  $k_g$  between normal eyes, suspect eyes, and grades of keratoconic eyes ( $P = .07$ ). The ratio of normalized  $k_c$  (mean) to  $k_g$  was significantly greater in normal eyes than in suspect eyes and grades of keratoconic eyes ( $P = .04$ ). The ratio of maximum corneal force to maximum extra-corneal force was significantly greater in normal eyes than in suspect eyes and grades of keratoconic eyes ( $P = .005$ ). The same was also observed with ratio of mean corneal force to mean extra-corneal tissue force ( $P < .001$ ). The deflection amplitude maximum was significantly lower in normal eyes than in grade 3 keratoconic eyes only ( $P < .001$ ). Both whole-eye movement maximum ( $P = .09$ ) and ratio of deflection amplitude to whole-eye movement maximum ( $P = .71$ ) were the same in all the groups.

Table 4 shows the results of the ROC analyses of CLMI and select biomechanical variables derived from the training dataset. Only biomechanical parameters that yielded an area under the ROC curve greater than 0.8 were included. All the CLMI variables had an excellent AUC, with 100% sensitivity and specificity. Among the biomechanical variables, the adjusted kc (linear), kc (mean), and deflection amplitude had an AUC greater than or equal to 0.95. These also had similar sensitivity and specificity ( $P > .05$ ). In a logistic regression model, stepwise regression with these biomechanical variables yielded a composite linear combination of kc (constant) and kc (mean) as the best indicator of suspect eyes and keratoconus eyes. The coefficients of the logistic regression model were  $-23.03 \pm 8.09$  and  $14.05 \pm 4.97$  for kc (constant) and kc (mean), respectively. The logistic regression model improved the AUC to  $1.0 \pm 0.0$  with a sensitivity and specificity of 99.6% and 100.0%, respectively (cutoff probability = 0.45).

Equation 4 is the logistic regression model derived from the training dataset to calculate the probability score (p) of the presence of keratoconus:

$$p = \frac{e^A}{1+e^A} \quad (4)$$

where  $A = 983.05 + 14.05 \times \text{kc (mean)} - 23.03 \times \text{kc (constant)}$ .

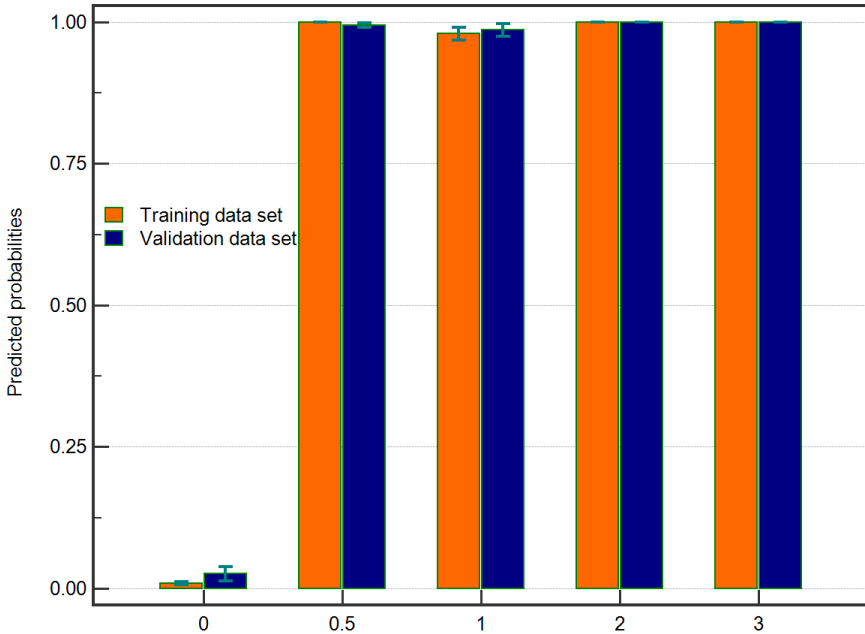


Figure 3: Mean  $\pm$  standard error of the predicted probabilities of the presence of disease in training and validation dataset. The predicted probabilities were calculated using equation 4 (described in Results).

The multivariate ANCOVA analyses of the training dataset eyes provided a regression equation (Appendix 1) that correlated  $k_c$  (constant) and  $k_c$  (mean) with the corrected IOP, CCT, and grade of the disease. These equations were used to derive  $k_c$  (constant) and  $k_c$  (mean) of the validation dataset eyes using the corrected IOP, CCT, and disease grades of the same eyes. When  $k_c$  (constant) of the validation dataset eyes derived from the ANCOVA equations (Appendix 1) of the training database was compared with  $k_c$  (constant) of the same eyes



calculated directly from equation 1, the intraclass correlation coefficient was 0.96, indicating excellent agreement. A similar result was obtained for kc (mean). Table 5 shows the demographics of the eyes included in the validation dataset. The differences between the group means (Table 5) were similar to those of the training dataset (Table 1) except for age.

The probability score of the eyes in the validation dataset was calculated with derived values of stiffness parameters (using equations in Appendix 1) and equation 4. The multivariate model and logistic regression equation 4 were able to achieve 99.5% sensitivity and 100% specificity with an accuracy of 99.6% in distinguishing normal and disease eyes (both fellow and keratoconic) belonging to the validation dataset. The newer CBI and TBI indices were also analyzed with the ROC method. For the training dataset, the sensitivity, specificity, AUC, and cutoff of the CBI index was 80.4%, 93.5%, 0.93, and 0.47, respectively, and of the TBI index, 89.3%, 96.4%, 0.96, and 0.86, respectively. For the validation dataset, the sensitivity, specificity, AUC, and cutoff of the CBI index was 84.1%, 84.5%, 0.89, and 0.62, respectively, and of the TBI index, 86.9%, 85.7%, 0.9, and 0.99, respectively. Table 6 shows the sensitivity, accuracy, and specificity of select variables from Table 4 when applied to the validation dataset. Figure 3 is a bar chart with mean  $\pm$  standard error of the predicted probabilities in each of the groups for training and validation datasets.

## Discussion

Analyses of waveforms obtained from the dynamic bidirectional applanation device and dynamic Scheimpflug analyzer have become of interest recently. The dynamic bidirectional applanation device indices, CH and CRF, were clearly lower in magnitude in keratoconic eyes.<sup>4, 14</sup> However, CH and CRF were not able to completely distinguish between normal eyes and eyes with early forms of keratoconus.<sup>19, 20</sup> They were associated with too much variability between normal, suspect, and confirmed cases of keratoconus.<sup>19, 20</sup> Thus, researchers studied other features of the dynamic bidirectional applanation device waveform to assess whether other metrics could distinguish better between normal, suspect, and confirmed cases of keratoconus.<sup>4, 14, 21, 22</sup> Additional waveform analyses yielded variables with higher sensitivity and specificity to detect keratoconic eyes, but detection of suspect eyes was relatively inferior to detection of confirmed keratoconic eyes.<sup>4, 14, 21, 22</sup> The additional variables were relatively insensitive to the possible effects of collagen CXL, which is expected to result in some biomechanical stiffening.<sup>5</sup> The previous studies analyzed distinct features of the waveform.<sup>4, 14, 21, 22</sup> This study uses the entire waveform to calculate stiffness parameters. This was similar to the concept of the hysteresis loop area, which used the entire waveform.<sup>4, 5</sup>

The Corvis ST is a relatively new device for assessing corneal biomechanical properties. Because it can image the corneal response

explicitly, we hypothesized that waveform analyses of the waveforms might result in better distinction between normal and suspect eyes. Several studies have introduced innovative waveform-derived approaches to quantify the corneal stiffness in some form. A recent study used linear discriminant function to improve the detection of subclinical keratoconus.<sup>23</sup> Among individual variables, deformation amplitude had the best AUC of  $0.775 \pm 0.044$  with a sensitivity and specificity of 53.6% and 79.3%, respectively.<sup>23</sup> Linear combination of deformation amplitude, time of first applanation, and CCT had an improved area of  $0.893 \pm 0.028$  with a sensitivity and specificity of 85.7% and 82.07%, respectively.<sup>23</sup> The linear discriminant function was similar to the ANCOVA analyses used in this study. Another study used the lateral displacement of the corneal apex during applanation to differentiate between normal eyes and keratoconic eyes.<sup>24</sup> The study reported a sensitivity and specificity of 85% and 98%, respectively, using multiple discriminant functions. However, no subclinical cases were considered in the same study.<sup>24</sup> Overall, the results from these waveform studies were marginally better than the results from independent analyses of the manufacturer-specified dynamic Scheimpflug analyzer variables.<sup>7-9</sup>

Another study aimed to estimate the elasticity and viscosity of the cornea from force versus deformation amplitude curve, which is essentially similar to a hysteresis curve.<sup>25</sup> The authors defined a tangent stiffness coefficient, which achieved a sensitivity and specificity of

88.0% and 85.29%, respectively, between normal and keratoconic eyes. A major limitation in that study was that the deflection amplitude was not extracted from the deformation amplitude. Therefore, the study associated viscous properties of the whole-eye movement with the cornea.<sup>25</sup> However, the explicit contribution of each ocular component (fat, sclera, and muscles) to  $u_2$  was not possible from the analytical model. It should be noted that the cornea is a viscoelastic tissue, but the magnitude of viscous dissipation is nonlinear; that is, it depends on the loading–unloading rate.<sup>26</sup> Thus, viscous dissipation was considered negligible in these patient measurements and in the model predictions for the duration of the dynamic Scheimpflug analyzer measurements. Another study using the dynamic bidirectional applanation device defined a variable called the hysteresis loop area.<sup>4</sup> The hysteresis loop area was the magnitude of the area enclosed by the loop obtained by plotting pressure (as raw units) against the intensity of the reflected infrared signal (as raw units). This infrared red signal may be considered a surrogate for deformation amplitude; that is, deflection amplitude plus whole-eye movement.<sup>4</sup> Thus, hysteresis loop area, by definition, does not describe the deflection amplitude explicitly. The analyses presented in this study improved on the hysteresis loop area. Furthermore, the pressure profiles using the dynamic Scheimpflug analyzer and the dynamic bidirectional applanation device were different. Direct comparison of the 2 profiles was not possible because the dynamic bidirectional applanation device pressure was exported in arbitrary raw

units, unlike the dynamic Scheimpflug analyzer device in which the unit of pressure was millimeters of mercury.<sup>4</sup>

Using the dynamic bidirectional applanation device waveform analyses, minimum concavity time and hysteresis loop area had the best AUC ( $0.985 \pm 0.002$  and  $0.967 \pm 0.002$ , respectively).<sup>4</sup> This was significantly better than the area for CH and CRF.<sup>4</sup> Another study compared normal eyes and forme fruste keratoconic eyes using waveform-derived dynamic bidirectional applanation device variables.<sup>14</sup> Variables such as first applanation peak and area under the first applanation waveform were significant discriminants of forme fruste keratoconic eyes with an AUC less than 0.75.<sup>14</sup> Only 2 of the 54 custom variables analyzed attained an AUC greater than 0.7.<sup>14</sup> The hysteresis loop area (0.694) was not among the top 2 variables in the study,<sup>14</sup> unlike in an earlier study.<sup>4</sup> Multivariate analyses of waveform-derived dynamic bidirectional applanation device variables also did not improve the AUC, sensitivity, and specificity significantly over the unadjusted variables.<sup>22</sup> Thus, the dynamic bidirectional applanation device-derived custom variables were unsuitable for early detection of keratoconus.

In this study, multivariate analyses were used to analyze new biomechanical variables. These variables used waveform analyses to distinguish between normal, suspect, and keratoconic eyes. A salient finding of the study was that kc or corneal stiffness performed well to distinguish suspect eyes and keratoconic eyes from normal eyes, with a

combined sensitivity and specificity greater than 90% and 91%, respectively. This study also showed that deflection amplitude (AUC = 0.95) was a better distinguisher of suspect and keratoconic eyes from normal eyes. Two versions of  $k_c$  were defined: a linear form and a nonlinear form. The hypothesis behind the 2 definitions followed the principles of soft tissue biomechanics in which a combination of linear and nonlinear terms was used to describe the strain energy of the tissue.<sup>10</sup> Therefore, logistic regression analyses were performed using a linear combination of  $k_c$  (constant) and  $k_c$  (mean). These analyses improved the AUC to  $1.0 \pm 0.0$  with a sensitivity and specificity of 99.6% and 100.0%, respectively. Furthermore, the multivariate analyses and logistic regression equation 4 achieved comparable segregation of normal and diseased eyes in the validation dataset. Overall, the performance of the stiffness-based segregation of normal and diseased eyes was better than the CBI and TBI indices. The sensitivity and specificity of CBI and TBI were better in a recent study.<sup>11</sup> However, the demographics of the eyes used were not included in that study. Therefore, an objective comparison between the earlier and the current study was not possible. An interesting feature of this study was that multivariate analyses of the CLMI variables were also useful in differentiating the suspect eyes from the normal eyes. Both IOP and CCT can affect curvature and therefore require adjustment using the ANCOVA method.<sup>27, 28</sup>

In summary, this study clearly showed that biomechanical analyses of the dynamic Scheimpflug analyzer waveforms (deflection amplitude and whole-eye movement) improved the differentiation of suspect and keratoconic eyes from normal eyes. However, the progression of the suspect eyes would have to be monitored over the long term to confirm the accuracy of the model. This is a limitation of the study. The analytical model also cannot derive strain in the tissue from the deformations. Advanced methods based on finite-element modeling might provide this information.<sup>10</sup> However, this study showed that the suspect eyes had an abnormal waveform relative to the normal eyes. Thus, there may be a compromised biomechanical trait in early keratoconus, unlike the conclusion from a recent study using the waveform variables from the dynamic bidirectional applanation device.<sup>22</sup> Further studies with larger sample sizes and different populations have to be performed to establish universal usefulness of the indices presented in this study.

## Appendix

The ANCOVA equation for kc (constant), using the training data set, was as follows:

$$\text{kc (constant)} = 34.36 + 2.19 \times \text{IOP} + 0.075 \times \text{CCT} + \rho_1$$

where  $\rho_1$  was -7.16, -6.11, -9.31 and -11.74 was suspect, grade 1, grade 2 and grade 3 eyes, respectively. For normal eyes,  $\rho_1$  was 0.0.

The ANCOVA equation for kc (mean), using the training data set, was as follows:

$$kc (\text{mean}) = -5.84 + 3.59 \times IOP + 0.107 \times CCT + \rho_2$$

where  $\rho_2$  was -9.73, -8.64, -11.02 and -14.12 was suspect, grade 1, grade 2 and grade 3 eyes, respectively. For normal eyes,  $\rho_2$  was 0.0.

The values of kc (constant) and kc (mean) from the above 2 equations were used in equation 4. In the equations above, IOP and CCT are expressed in millimeters of mercury (mm Hg) and microns ( $\mu\text{m}$ ), respectively.

### **Author Contributions**

**Francis M:** Concept and design, analysis and interpretation of data, drafting manuscript, and statistical analysis.

**Pahuja N:** Data acquisition, analysis and interpretation of data, and drafting manuscript.

**Shroff R:** Data acquisition, analysis and interpretation of data, and drafting manuscript.

**Gowda R:** Data acquisition, analysis and interpretation of data, and drafting manuscript.

**Matalia H:** Concept and design, critical revision of manuscript, and supervision.

**Shetty R:** Concept and design, critical revision of manuscript, securing funding, supervision, and final approval.



**Remington Nelson EJ:** Concept and design, analysis and interpretation of data, critical revision of manuscript, and securing funding.

**Sinha Roy A:** Concept and design, drafting manuscript, critical revision of manuscript, securing funding, supervision, and final approval.

## Disclosures

Dr. Sinha Roy has intellectual property on biomechanical modeling of the eye through Cleveland Clinic Innovations, Cleveland, Ohio, USA. None of the other authors has a financial or proprietary interest in any material or method mentioned.

## References

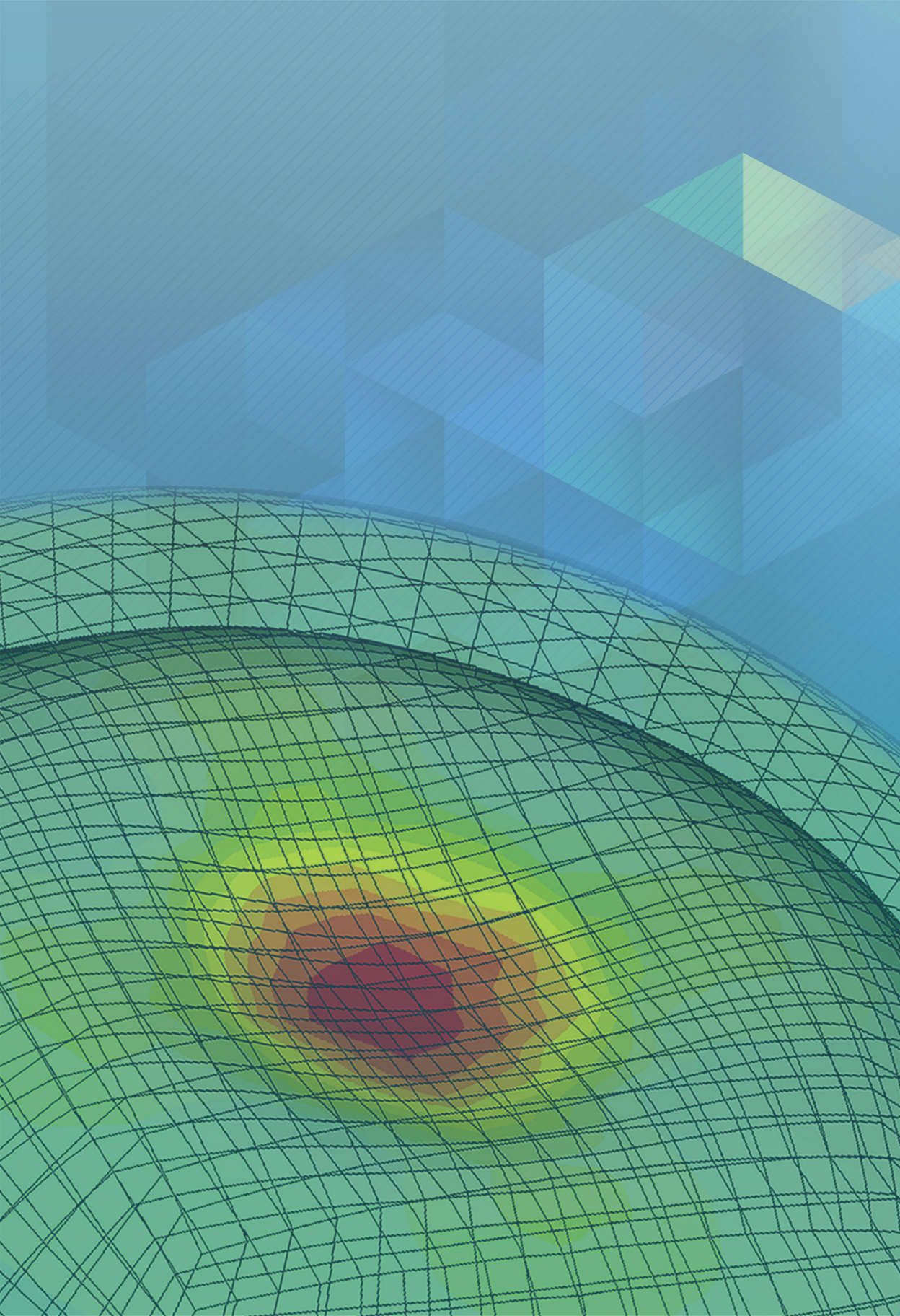
1. Tejwani S, Dinakaran S, Joshi A, Shetty R, Sinha Roy A. A cross-sectional study to compare intraocular pressure measurement by sequential use of Goldman applanation tonometry, dynamic contour tonometry, ocular response analyzer, and Corvis ST. *Indian J Ophthalmol* 2015;63:815-820.
2. Liu J, Roberts CJ. Influence of corneal biomechanical properties on intraocular pressure measurement: quantitative analysis. *J Cataract Refract Surg* 2005;31:146-155.
3. Terai N, Raiskup F, Haustein M, Pillunat LE, Spoerl E. Identification of biomechanical properties of the cornea: the ocular response analyzer. *Curr Eye Res* 2012;37:553-562.

4. Hallahan KM, Sinha Roy A, Ambrosio R, Jr., Salomao M, Dupps WJ, Jr. Discriminant value of custom ocular response analyzer waveform derivatives in keratoconus. *Ophthalmology* 2014;121:459-468.
5. Hallahan KM, Rocha K, Roy AS, Randleman JB, Stulting RD, Dupps WJ, Jr. Effects of corneal cross-linking on ocular response analyzer waveform-derived variables in keratoconus and postrefractive surgery ectasia. *Eye Contact Lens* 2014;40:339-344.
6. Hon Y, Lam AK. Corneal deformation measurement using Scheimpflug noncontact tonometry. *Optometry and Vision Science* 2013;90:e1-e8.
7. Tian L, Huang Y-F, Wang L-Q, et al. Corneal biomechanical assessment using corneal visualization scheimpflug technology in keratoconic and normal eyes. *Journal of Ophthalmology* 2014;2014.
8. Ali NQ, Patel DV, McGhee CN. Biomechanical responses of healthy and keratoconic corneas measured using a noncontact scheimpflug-based tonometer. *Investigative ophthalmology & visual science* 2014;55:3651-3659.
9. Shetty R, Nuijts RM, Srivatsa P, et al. Understanding the correlation between tomographic and biomechanical severity of keratoconic corneas. *BioMed research international* 2015;2015.
10. Sinha Roy A, Kurian M, Matalia H, Shetty R. Air-puff associated quantification of non-linear biomechanical properties

- of the human cornea in vivo. *J Mech Behav Biomed Mater* 2015;48:173-182.
11. Vinciguerra R, Ambrósio Jr R, Elsheikh A, et al. Detection of keratoconus with a new biomechanical index. *Journal of refractive surgery* 2016;32:803-810.
  12. Li X, Rabinowitz YS, Rasheed K, Yang H. Longitudinal study of the normal eyes in unilateral keratoconus patients. *Ophthalmology* 2004;111:440-446.
  13. Holland DR, Maeda N, Hannush SB, et al. Unilateral keratoconus: incidence and quantitative topographic analysis. *Ophthalmology* 1997;104:1409-1413.
  14. Luz A, Lopes B, Hallahan KM, et al. Discriminant value of custom ocular response analyzer waveform derivatives in forme fruste keratoconus. *American journal of ophthalmology* 2016;164:14-21.
  15. Pinero DP, Alio JL, Barraquer RI, Michael R, Jimenez R. Corneal biomechanics, refraction, and corneal aberrometry in keratoconus: an integrated study. *Invest Ophthalmol Vis Sci* 2010;51:1948-1955.
  16. Matalia J, Francis M, Tejwani S, Dudeja G, Rajappa N, Sinha Roy A. Role of Age and Myopia in Simultaneous Assessment of Corneal and Extraocular Tissue Stiffness by Air-Puff Applanation. *J Refract Surg* 2016;32:486-493.

17. Han Z, Tao C, Zhou D, et al. Air puff induced corneal vibrations: theoretical simulations and clinical observations. *J Refract Surg* 2014;30:208-213.
18. Mahmoud AM, Roberts CJ, Lembach RG, et al. CLMI: the cone location and magnitude index. *Cornea* 2008;27:480-487.
19. Kirwan C, O'Malley D, O'Keefe M. Corneal hysteresis and corneal resistance factor in keratoectasia: findings using the Reichert ocular response analyzer. *Ophthalmologica* 2008;222:334-337.
20. Shah S, Laiquzzaman M, Bhojwani R, Mantry S, Cunliffe I. Assessment of the biomechanical properties of the cornea with the ocular response analyzer in normal and keratoconic eyes. *Invest Ophthalmol Vis Sci* 2007;48:3026-3031.
21. Schweitzer C, Roberts CJ, Mahmoud AM, Colin J, Maurice-Tison S, Kerautret J. Screening of forme fruste keratoconus with the ocular response analyzer. *Invest Ophthalmol Vis Sci* 2010;51:2403-2410.
22. Galletti JD, Ruiseñor Vázquez PR, Fuentes Bonthoux F, Pfortner T, Galletti JG. Multivariate analysis of the ocular response analyzer's corneal deformation response curve for early keratoconus detection. *Journal of ophthalmology* 2015;2015.
23. Peña-García P, Peris-Martínez C, Abbouda A, Ruiz-Moreno JM. Detection of subclinical keratoconus through non-contact

- tonometry and the use of discriminant biomechanical functions. *Journal of Biomechanics* 2016;49:353-363.
24. Koprowski R, Ambrosio R, Jr. Quantitative assessment of corneal vibrations during intraocular pressure measurement with the air-puff method in patients with keratoconus. *Computers in biology and medicine* 2015;66:170-178.
  25. Wang LK, Tian L, Zheng YP. Determining in vivo elasticity and viscosity with dynamic Scheimpflug imaging analysis in keratoconic and healthy eyes. *J Biophotonics* 2016;9:454-463.
  26. Nguyen TD, Jones RE, Boyce BL. A nonlinear anisotropic viscoelastic model for the tensile behavior of the corneal stroma. *J Biomech Eng* 2008;130:041020.
  27. McMonnies CW, Boneham GC. Corneal responses to intraocular pressure elevations in keratoconus. *Cornea* 2010;29:764-770.
  28. Kocamis SI, Cakmak HB, Cagil N, Toklu Y. Investigation of the Efficacy of the Cone Location and Magnitude Index in the Diagnosis of Keratoconus. *Semin Ophthalmol* 2016;31:203-209.





# Corneal viscous properties cannot be determined from air-puff applanation

Francis M, Matalia H, Nuijts RMMA, Haex B, Shetty R, Sinha Roy A

J Refract Surg. 2019 Nov 1;35(11):730-736

Francis M, Matalia H, Nuijts RMMA, Haex B, Shetty R, Sinha Roy A. Corneal viscous properties cannot be determined from air-puff applanation. J Refract Surg. 2019;35(11):730-736. doi:10.3928/1081597X-20191010-03.

Reprinted with permission from SLACK Incorporated.  
See above for citation information.

**Purpose:** To assess whether corneal viscous properties are measurable with air-puff applanation in patients.

**Methods:** The study had 312 normal eyes, 107 fellow eyes of patients with keratoconus, and 289 keratoconic eyes. The Corvis ST (Oculus Optikgeräte GmbH, Wetzlar, Germany) deformation data for all eyes were analyzed using two models. First, a standard linear solid model (SLM) assumed the cornea was an elastic material only. Second, a two-compartment Kelvin-Voigt model (KVM) assumed the cornea was a viscoelastic material. Corneal stiffness and viscosity were calculated. Further, the deflection amplitude was phase shifted virtually relative to the air-puff applanation force to assess whether the KVM was capable of detecting corneal viscous properties from air-puff applanation. This was similar in concept to measured viscoelastic deformations in other soft tissues. The hysteresis area was also calculated with deformation (cornea and whole globe) and deflection (cornea only) amplitude. The greater the magnitude of the hysteresis area, the greater was the magnitude of corneal viscosity ( $\mu\text{c}$ ).

**Results:** Both the SLM and KVM reported similar magnitudes of corneal stiffnesses (correlation coefficient  $> 0.99$ ). However, for a given model, corneal stiffness was significantly different between normal, fellow, and keratoconic eyes ( $P = .001$ ). From the KVM, the corneal viscosity was different between groups ( $P = .001$ ) but was small in magnitude (order of  $10^{-9}$ ). The deflection hysteresis area was also small



Corneal viscous properties cannot be determined

in magnitude (order of  $10^{-6}$ ). In contrast, the KVM detected significant corneal viscosity only when the deflection amplitude was virtually phase shifted with respect to the air-puff applanation force.

**Conclusions:** No significant corneal viscous response was detected in patients who had air-puff applanation.

## Introduction

Corneal biomechanical properties have received significant attention in recent years due to their hypothesized role in predicting subclinical keratoconus and ectasia after refractive surgery.<sup>1-4</sup> This prediction is possible only if *in vivo* quantification of properties exists. However, the human cornea exhibits both viscous and elastic responses to induced stress,<sup>5-7</sup> and *in vivo* quantifications of both features in patients are challenging. The viscoelastic material assumption may be necessary to understand corneal deformation due to air-puff applanation.<sup>8</sup> Porcine corneas are naturally thicker and differ from human corneas in terms of *in situ* fiber distribution.<sup>8</sup> Thus, differences between the deformation of porcine and human corneas in response to the same air-puff applanation could be expected. Hence, we investigated whether a viscoelastic response can be determined from *in vivo* deformation of patient corneas in this study.

The Ocular Response Analyzer (Reichert Technologies, Depew, NY) and Corvis ST (Oculus Optikgeräte GmbH, Wetzlar, Germany) are the only current clinical devices for *in vivo* assessment of corneal biomechanical properties with air-puff applanation. Only the Corvis ST segregates the corneal deformation and whole globe movement during the applanation.<sup>7</sup> The Corvis ST can quantify the entire applanation process due to the capture of 140 image frames at a sampling rate of 4,330 frames per second with an ultra-high-speed Scheimpflug

camera.<sup>2</sup> Currently, two classes of mathematical approaches are available for the calculation of biomechanical properties from the deformation amplitude: rheological closed-form analytical<sup>2, 9, 10</sup> and inverse finite element methods.<sup>6, 7, 11</sup> The rheological models are simpler, computationally non-intensive, and fast.<sup>2, 9, 10</sup>

The current study used the rheological model to assess the in vivo corneal deformation. The method was applied to three groups of patients: normal eyes, topographically normal fellow eyes of patients with asymmetric keratoconus, and patients with clinical keratoconus.

## **Methods**

This study was a retrospective analysis of Corvis ST data (Asian-Indian eyes) collected at the Narayana Nethralaya Multi-specialty Eye Hospital, Bangalore, India. The study was conducted in accordance with the tenets of the Declaration of Helsinki, after obtaining institutional ethics committee approval. The study included 312 normal eyes (only one eye was chosen at random with a coin toss from 312 patients), 107 fellow eyes of patients with asymmetric keratoconus (a subset of 107 of 289 patients with keratoconus), and 289 keratoconic eyes (289 patients). These eyes formed the study population of an earlier study.<sup>2</sup> The corneal tomographic features were derived from Pentacam (Oculus Optikgeräte GmbH; software version 1.21b26) and Corvis ST (software version 1.5r1902). The Corvis ST data were exported in the form of a comma

separated value file, which included the deformation amplitude (total), deflection amplitude (corneal only), whole eye movement (extracorneal only), and air-puff pressure waveform.<sup>2, 9, 10</sup> Here, deformation amplitude was the arithmetic sum of deflection amplitude and whole eye movement.

Data were analyzed using two spring-dashpot models. The first one was a standard linear solid model (SLM), assuming the cornea was an elastic material and extracorneal tissue was a viscoelastic material (Figure AA, available in the online version of this article). This model has already been used in interpreting the corneal and extracorneal material properties in a variety of conditions, such as aging, myopia, autoimmune response, keratoconus, after refractive surgery, and after corneal cross-linking.<sup>2, 9, 10, 12-15</sup> The second model was a two-compartment Kelvin-Voigt model in which both the corneal and extracorneal tissue were modeled as viscoelastic materials (Figure AB). Both models were solved for every eye with a non-linear least square technique in MATLAB R2013a (MathWorks, Inc., Natick, MA).<sup>2, 9, 10, 12-15</sup> The following parameters were derived from the above models, as described in our previous publications<sup>2, 9, 10, 12-15</sup>:

1.  $k_c$ (constant): constant corneal stiffness (N/m), a measure of the linear elastic response of the cornea

2.  $k_c(\text{mean})$ : mean corneal stiffness (N/m), a measure of the non-linear elastic response of the cornea as a function of the applied air-puff pressure
3.  $\mu_c$ : corneal viscosity (Pa.sec), calculated only for the second model
4.  $k_g$ : extra-corneal stiffness (N/m)
5.  $\mu_g$ : extra-corneal viscosity (Pa.sec)
6. Deformation hysteresis area: the area enclosed by the applied air-puff force and DA (N.m) [calculated directly from measured patient data]. This area is a theoretical measure of the degree of viscous response of the whole-globe. Greater the area, greater will be the viscosity ( $\mu_g$ ) of the whole-globe.
7. Deflection hysteresis area: the area enclosed by the corneal force to deflection amplitude plot (N.m) [using the two spring-dashpot model only]. This area is a theoretical measure of the degree of viscous response of the cornea only. Greater the area, greater will be the viscosity ( $\mu_c$ ) of the cornea.

From fundamental mechanics, it is well known that the measured deformation of a viscoelastic material will lag in phase relative to the applied force (eg, the peak deformation will be reached after the peak force has passed). To assess whether the second model was able to sense any viscoelastic feature of the cornea, the deflection amplitude derived from the in vivo measurement was advanced in time by one frame (up to 6 frames) at a time and then added to the in vivo measurement of the

whole eye movement to obtain a modified deformation amplitude. The shift was performed in the direction of increasing time (Figure B, available in the online version of this article). Each shift by one frame led to an additional time difference of 0.231 msec between peak air-puff pressure and peak modified deformation amplitude. Physically, this would imply that  $\mu c$  would increase in magnitude with every frame shift. Figure B shows the schematic of the deformation amplitude waveform after shifts by 2, 4, and 6 frames for a normal eye (Figure BA), fellow eye (Figure BB), and keratoconic eye (Figure BC). The changes in the viscoelastic parameters after frame shift from the baseline were analyzed for each group.

Table 1: Median [95% confidence interval] of clinical parameters of the study eyes.

	Normal eye (NE)	Fellow eye of Keratoconus patient (FE)
Sample size (eyes)	300	102
Age (years)	25 [24 to 25]	24 [22 to 25]
IOP (mmHg)	16.7 [16.5 to 17]	16.1 [15.78 to 16.4]
CCT ( $\mu\text{m}$ )	528.5 [525 to 533.71]	505 [498 to 515]
TCT ( $\mu\text{m}$ )	525 [521 to 530.41]	502 [491.97 to 506.01]
K1 (D)	43.2 [42.96 to 43.5]	43.4 [43.2 to 43.88]
K2 (D)	44.4 [44.3 to 44.7]	44.7 [44.3 to 45]

Corneal viscous properties cannot be determined

Kmean (D)	43.8 [43.5 to 44.1]	44.05 [43.7 to 44.4]
Kmax (D)	44.9 [44.7 to 45.14]	45.6 [45.3 to 46.3]
CBI	0.02 [0.01 to 0.03]	0.79 [0.56 to 0.89]
TBI	0.29 [0.23 to 0.36]	0.99 [0.96 to 1]
LORMS aberration (µm)	1.58 [1.5 to 1.66]	1.93 [1.77 to 2.07]
HORMS aberration (µm)	0.37 [0.37 to 0.39]	0.51 [0.46 to 0.55]

Table 1: continued

Keratoconus eye (KE)	p-value	Conover post-hoc test of significance
293	-	NA
24 [23 to 25]	0.003	NE to FE and KE
16 [15.7 to 16.3]	0.001	NE to FE and KE
464 [458 to 471]	0.001	All
453 [447 to 459]	0.001	All
45.2 [45 to 45.7]	0.001	KE to NE and FE
49.2 [48.7 to 49.5]	0.001	KE to NE and FE
47.1 [46.6 to 47.53]	0.001	KE to NE and FE
53.5 [52.77 to 54.8]	0.001	All
1 [1 to 1]	0.001	All
1 [1 to 1]	0.001	All
8.05 [7.26 to 8.58]	0.001	All
2.03 [1.72 to 2.14]	0.001	All

NE = normal eyes; FE = fellow eye of patient with keratoconus; KE = keratoconic eyes; IOP = intraocular pressure; CCT = central corneal thickness; TCT = thinnest corneal thickness; K1 = flat keratometry; D

= diopters; K2 = steep keratometry; Kmean = mean keratometry; Kmax = maximum keratometry; CBI = Corvis Biomechanical Index; TBI = Tomographic Biomechanical Index; LORMS = lower order root mean square; HORMS = higher order root mean square; all = significant difference was observed between all groups

Table 2: Group-wise median [95% confidence interval] obtained from the 2 Models

Model	Parameters	Normal eye (NE)	Fellow eye of Keratoconic eye (FE)
Standard linear solid model (SLM)	kc (constant) (N/m)	107.37 [105.57 to 108.85]	100.87 [98.79 to 104.78]
	kc (mean) (N/m)	103.05 [101.34 to 104.71]	92.56 [90.5 to 95.62]
	kg (N/m)	71.46 [69.19 to 73.32]	59.28 [53.99 to 62.76]
	$\mu$ g (Pasec)	0.3 [0.29 to 0.31]	0.28 [0.26 to 0.31]
	Deflection hysteresis area (Nm)	$4.26 \times 10^{-6}$ [ $3.99 \times 10^{-6}$ to $4.66 \times 10^{-6}$ ]	$4.63 \times 10^{-6}$ [ $4.23 \times 10^{-6}$ to $5.04 \times 10^{-6}$ ]
2-compartment Kelvin-Voigt model (KVM)	kc (constant) (N/m)	106.99 [105.34 to 108.7]	100.87 [98.79 to 104.78]
	kc (mean) (N/m)	102.59 [100.64 to 104.15]	93.13 [89.99 to 95.6]
	$\mu$ c (Pasec)	$4.36 \times 10^{-9}$ [ $1.33 \times 10^{-10}$ to $1.8 \times 10^{-8}$ ]	$9.48 \times 10^{-12}$ [ $1.25 \times 10^{-13}$ to $1.03 \times 10^{-10}$ ]
	kg (N/m)	72.14 [70.26 to 75.86]	59.51 [55.17 to 63.26]



	$\mu g$ (Pasec)	0.31 [0.3 to 0.33]	0.29 [0.26 to 0.32]
	Deflection hysteresis area (Nm)	$4.69 \times 10^{-6}$ [ $4.26 \times 10^{-6}$ to $4.93 \times 10^{-6}$ ]	$4.62 \times 10^{-6}$ [ $4.15 \times 10^{-6}$ to $4.87 \times 10^{-6}$ ]
Deformation hysteresis area (Nm)		$2.07 \times 10^{-5}$ [ $1.94 \times 10^{-5}$ to $2.16 \times 10^{-5}$ ]	$2.22 \times 10^{-5}$ [ $2.02 \times 10^{-5}$ to $2.37 \times 10^{-5}$ ]

Table 2: continued

Keratoconic eye (KE)	P <sup>a</sup>	Conover post-hoc test of significance
94.85 [93.77 to 96.34]	0.001	All
85.8 [84.04 to 88.77]	0.001	All
59.38 [56.42 to 61.75]	0.001	NE to FE and KE
0.25 [0.24 to 0.26]	0.001	KE to NE and FE
$5.82 \times 10^{-6}$ [ $5.48 \times 10^{-6}$ to $6.22 \times 10^{-6}$ ]	0.001	KE to NE and FE
94.85 [93.77 to 96.34]	0.001	All
85.54 [83.97 to 89.17]	0.001	All
$4.29 \times 10^{-12}$ [ $1.04 \times 10^{-12}$ to $1.49 \times 10^{-11}$ ]	0.001	NE to FE and KE
59.82 [56.63 to 62.12]	0.001	NE to FE and KE
0.25 [0.24 to 0.27]	0.001	KE to NE and FE
$5.80 \times 10^{-6}$ [ $5.47 \times 10^{-6}$ to $6.14 \times 10^{-6}$ ]	0.001	KE to NE and FE
$2.14 \times 10^{-5}$ [ $2.06 \times 10^{-5}$ to $2.2 \times 10^{-5}$ ]	0.04	NE to FE

NE = normal eyes; FE = fellow eye of patient with keratoconus; KE = keratoconic eyes; SLM = standard linear solid model; kc = corneal stiffness; kg = extracorneal stiffness;  $\mu g$  = extracorneal viscosity; KVM

= 2-compartment Kelvin-Voigt model;  $\mu c$  = corneal viscosity; all = significant difference was observed between groups; <sup>a</sup>Kruskal–Wallis test.

Statistical analyses were performed using MedCalc software (version 19.0.3; MedCalc Inc., Ostend, Belgium). The statistical analyses were based on non-parametric assumptions as determined by the Shapiro-Wilk test. All reported values were median and 95% confidence interval. The Kruskal-Wallis test was used to determine the statistical differences between the groups. The statistical difference between parameters calculated before and after frame shift was done using the Friedman test. The Conover post-hoc test was used to account for multigroup comparisons. The agreement between parameters calculated from the two models was calculated using the concordance correlation coefficient (Cor). The Cor was defined without the assumptions of normal distribution.<sup>16</sup> Cor values of greater than 0.99, between 0.95 and 0.99, between 0.90 and 0.95, and less than 0.90 were considered as almost perfect, substantial, moderate, and poor, respectively.<sup>17</sup> A P value less than 0.05 was considered statistically significant.

## Results

Table 1 shows the demographics of eyes included in the study. Age (P = .003) and intraocular pressure (P = .001) showed significant

differences, but the magnitude of the observed difference was clinically insignificant (less than 1 mm Hg between the groups). All other parameters, such as central corneal thickness, thinnest corneal thickness, flat keratometry (K1), steep keratometry (K2), mean keratometry (Kmean), maximum keratometry (Kmax), Corvis Biomechanical Index (CBI), Tomographic Biomechanical Index (TBI), root mean square of lower order (LORMS), and higher order (HORMS) anterior aberrations, showed significant differences between the groups ( $P = .001$  for all). The groupwise significances of the above parameters are described in Table 1. The K1, K2, and Kmean were similar between normal eyes and fellow eyes, but differed from keratoconic eyes (Table 1). However, other parameters such as CBI, TBI, LORMS, and HORMS showed a significant difference between all groups when evaluated pairwise.

Table 2 shows the parameters calculated from the two models using the Corvis ST deformation amplitude. Both models segregate the deflection amplitude and whole eye movement to derive corneal and extracorneal biomechanical parameters. In both the SLM and KVM,  $k_c$  (constant) and  $k_c$  (mean) differed significantly between all groups ( $P < .001$ ). This indicated significant differences between the corneal stiffnesses of the three groups. In SLM,  $k_g$  of normal eyes differed significantly from fellow eyes and keratoconic eyes ( $P = .001$ ). Further,  $\mu_g$  of keratoconic eyes differed significantly from the normal eyes and fellow eyes ( $P = .001$ ). The same was observed with the KVM model

(Table 2). In the KVM,  $\mu c$  (corneal viscosity) of normal eyes differed significantly from that of fellow eyes and keratoconic eyes ( $P = .001$ ). However,  $\mu c$  was extremely small in magnitude (order of  $10^{-13}$ ) and this indicated no detectable viscosity of the cornea with air-puff applanation. This affected the measurement of both the deflection hysteresis and deformation hysteresis area, which were also small in magnitude (order of  $10^{-6}$ ). All variables were highly correlated between the SLM and KVM ( $Cor > 0.99$ ). This indicated virtually no difference between the magnitudes of the variables from the SLM and KVM models, and was also confirmed statistically ( $P > .05$  for all variables in Table 2).

Figure 1 shows the change in corneal and extracorneal parameters using the KVM when the deflection amplitude waveform was artificially frame shifted. Both  $k_c$  (constant) (Figure 1A) and  $k_c$  (mean) (Figure 1B) initially increased and then decreased with the increasing frame shift. However,  $\mu c$  increased nearly linearly with increasing frame shift (Figure 1C). A trend opposing the change in corneal stiffness was noted with the change in  $k_g$  (Figure 1D) and  $\mu g$  (Figure 1E). Interestingly, the finite magnitude of  $\mu c$  with increasing frame shift was several orders of magnitude (order of  $10^{-2}$ ) greater than the in vivo measurement (Table 2). Thus, true viscous response of the cornea was lacking under air-puff applanation because even a single frame shift, if present in vivo, changed the order of magnitude of corneal viscosity from  $10^{-13}$  to  $10^{-2}$ . Figure 1 also presented a visual description of

changes in the deformation amplitude, if corneal viscous effects truly existed during in vivo air-puff applanation.

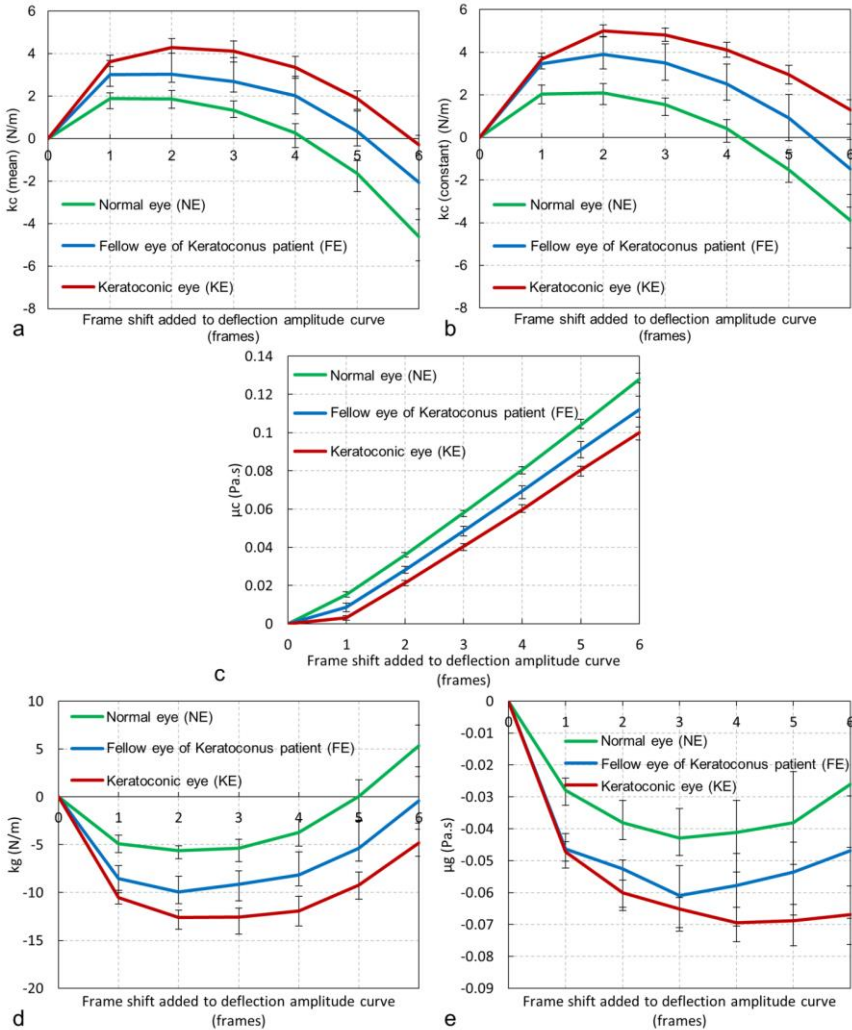


Figure 1. Relative change in corneal and extracorneal material property parameters due to frame shift (1 to 6 frames) with respect to in vivo data.

Material property parameters estimated after frame shift were (A) mean corneal stiffness:  $k_c$  (mean), (B) constant corneal stiffness:  $k_c$  (constant), (C) corneal viscosity:  $\mu_c$ , (D) extracorneal stiffness:  $k_g$ , and (E) extracorneal viscosity:  $\mu_g$ . With increasing virtual frame shift, corneal viscosity considerably increased in magnitude compared to the in vivo condition, where it was practically zero (Table 2).

### Discussion

In viscoelastic tissues, the measured deformation lags in phase relative to the applied force.<sup>18</sup> This phenomenon is well known among soft tissues. Further, the magnitude of tissue viscosity also depends on the time rate of change in the applied stress (ie, the loading rate).<sup>18</sup> In this study, no significant difference between the calculated parameters from the two models was noted (high magnitude of  $Cor$ ). Further, the order of magnitude of the calculated  $\mu_c$  from the KVM was insignificant and virtually zero (Table 2). We also investigated whether the KVM was capable of sensing viscous effects during the deformation of the cornea and whole globe. Hence, we conducted simulated perturbations where the deflection amplitude was artificially delayed in time to induce a lag in phase relative to the air-puff pressure pulse (Figure 1). This effect was analogous to inducing a “virtual” viscous effect.<sup>18</sup> Then, the KVM distinctly reported higher magnitudes of  $\mu_c$  (Figure 1C). This indicated that with the existing loading magnitude and loading rate (applied air-puff pressure profile), the cornea may not be able to

undergo any viscous deformation in vivo. Another recent study used the Burgers viscoelastic model to study corneal viscosity in normal and keratoconic corneas and concluded that that viscosity of the cornea does not contribute substantially to the deformation and deflection amplitude.<sup>19</sup>

Another study compared normal and keratoconic eyes using a stiffness model.<sup>20</sup> However, that study did not segregate the effect of deflection amplitude from the deformation amplitude in their stiffness model. Therefore, the study erroneously concluded that viscous properties of the cornea were detectable with air-puff applanation.<sup>20</sup> The study reported a mean deformation hysteresis area of  $6.06 \times 10^{-6}$  and  $7.78 \times 10^{-6}$  Nm in normal and keratoconic eyes, respectively.<sup>20</sup> Our results were smaller in magnitude due to the use of a patient-specific raw air-puff pressure profile instead of a smoothed average pressure curve in the earlier study.<sup>20</sup> In Figures 1A-1B, the change in corneal stiffness first increased and then decreased with increasing frame shift. This was because with the increasing “virtual” frame shift, the time difference between the peak air-puff pressure and peak deformation amplitude was increasing while the time difference between the peak deformation amplitude and the peak whole eye movement was decreasing. The interaction between these time differences for the solution of the SLM and KVM led to the trends shown in Figures 1A-1B. Likewise, the trends in Figures 1D-1E were opposite to Figures 1A-1B.

Keratoconus reduced the elastic modulus of the cornea.<sup>21</sup> However, the viscous properties of keratoconic corneas are unknown. The *in vivo* imaging of keratoconic corneas suggested local degeneration of biomechanical properties.<sup>22</sup> Therefore, this degeneration most likely was a combination of both elastic and viscous properties, although exact magnitudes of each property are unknown.<sup>22</sup> <sup>23</sup> Nonetheless, the air-puff applanation technique appeared inadequate to assess the viscous properties with the analytical models. An increase in the duration of the air-puff pulse and decrease in the magnitude of the air-puff pressure may assist *in vivo* quantification of viscous properties of the normal and diseased human cornea. The former will allow a greater time scale for viscous lag to occur and the latter will minimize the effects of whole globe movement. Figure 1 showed the changes expected in the stiffness and viscous parameters, if corneal viscous response truly existed during air-puff applanation. These data could serve as an important reference, if modifications were made to the device (eg, increase in duration of air-puff or decreased in magnitude of air-puff pressure).

A limitation of this study was that the model did not segregate the sclera contribution to the deformation amplitude. A recent finite element study concluded that the sclera could play a role in assessing corneal biomechanics.<sup>24</sup> The study showed that the corneal deformation differed under different *ex vivo* boundary conditions of fixed versus flexible limbus.<sup>24</sup> Despite this limitation, inverse finite element models of air-



puff applanation predicted accurately the postoperative deformation of patients' corneas after refractive surgery.<sup>7, 12</sup> Another limitation of the study was the lack of anisotropic properties in the biomechanical model. The SLM model formed the basis of our earlier studies using inverse finite elements.<sup>7, 12</sup> Hence, the findings of this study with respect to corneal viscoelastic properties were also applicable to the inverse finite element models. This study was limited to keratoconic eyes and fellow eyes. Future studies need to investigate whether other corneal degenerations enable detection of corneal viscosity with air-puff applanation. The viscous properties of the cornea may be below a measureable range with air-puff applanation under in vivo conditions. The conditions that could enable finite measurements of  $\mu c$  were simulated artificially by delaying the deflection amplitude in phase with respect to the applied air-puff pressure. Further evaluation in eyes from other regional populations should be conducted in future studies.

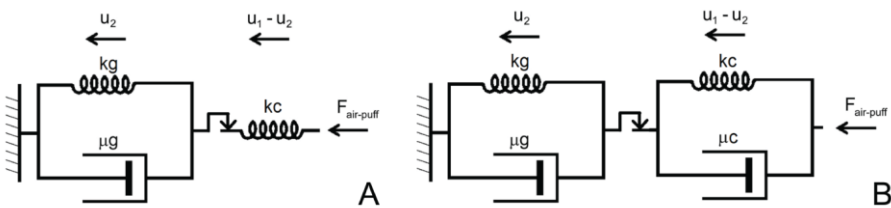


Figure A. (A) Standard linear solid model and (B) 2-compartment Kelvin-Voigt model describing deflection amplitude ( $u_1 - u_2$ ) and whole eye movement ( $u_2$ ) waveforms caused by air-puff applanation force ( $F_{\text{air-puff}}$ ). Here,  $u_1$  was deformation amplitude (DA) waveform.

Material property parameters calculated from the models were corneal stiffness (kc), corneal viscosity ( $\mu\text{c}$ ), extracorneal stiffness (kg), and extracorneal viscosity ( $\mu\text{g}$ ).

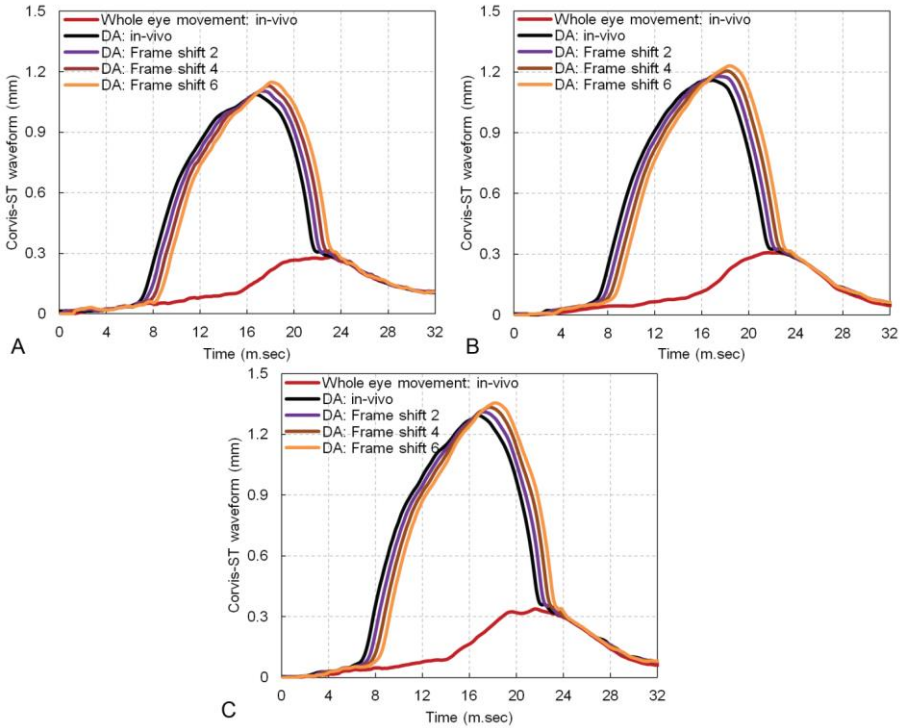


Figure B. Deformation amplitude (DA) curves after virtual frame shift (0, 2, 4, and 6, respectively) was introduced to the in vivo deflection amplitude curve in case of a selected (A) normal eye (NE), (B) fellow eye of a patient with keratoconus (FE), and (C) keratoconic eye (KE). Whole eye movement of the respective eye was also plotted for reference. The Corvis ST is manufactured by Oculus Optikgeräte GmbH, Wetzlar, Germany.

## **Author Contributions**

**Francis M:** Data collection, analysis and interpretation of data, writing the manuscript, and statistical expertise.

**Matalia H:** Data collection, analysis and interpretation of data, writing the manuscript, and statistical expertise.

**Nuijts RMMA:** Analysis and interpretation of data and critical revision of the manuscript.

**Haex B:** Analysis and interpretation of data and critical revision of the manuscript.

**Shetty R:** Analysis and interpretation of data and critical revision of the manuscript.

**Sinha Roy A:** Study concept and design, analysis and interpretation of data, writing the manuscript, critical revision of the manuscript, and statistical expertise.

## **Reference**

1. Ambrosio R, Jr. Post-LASIK Ectasia: Twenty Years of a Conundrum. *Semin Ophthalmol* 2019;34:66-68.
2. Francis M, Pahuja N, Shroff R, et al. Waveform analysis of deformation amplitude and deflection amplitude in normal, suspect, and keratoconic eyes. *J Cataract Refract Surg* 2017;43:1271-1280.

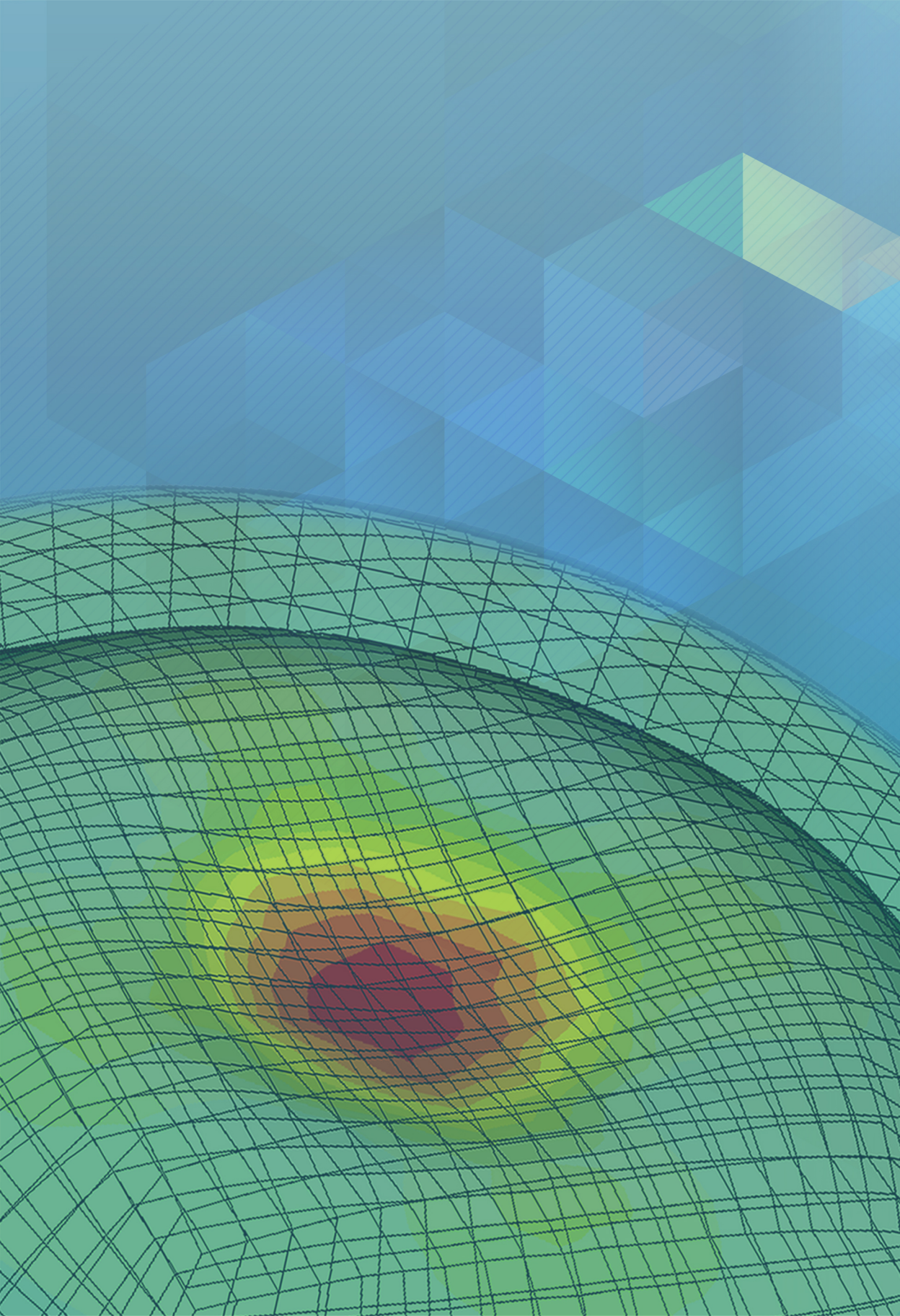
3. Vinciguerra R, Ambrosio R, Jr., Elsheikh A, et al. Detection of Keratoconus With a New Biomechanical Index. *J Refract Surg* 2016;32:803-810.
4. Ambrosio R, Jr., Correia FF, Lopes B, et al. Corneal Biomechanics in Ectatic Diseases: Refractive Surgery Implications. *Open Ophthalmol J* 2017;11:176-193.
5. Fraldi M, Cutolo A, Esposito L, Guarracino F. The role of viscoelasticity and stress gradients on the outcome of conductive keratoplasty. *Biomech Model Mechanobiol* 2011;10:397-412.
6. Kling S, Bekesi N, Dorransoro C, Pascual D, Marcos S. Corneal viscoelastic properties from finite-element analysis of in vivo air-puff deformation. *PLoS One* 2014;9:e104904.
7. Sinha Roy A, Kurian M, Matalia H, Shetty R. Air-puff associated quantification of non-linear biomechanical properties of the human cornea in vivo. *J Mech Behav Biomed Mater* 2015;48:173-182.
8. Maczynska E, Karnowski K, Szulzycki K, et al. Assessment of the influence of viscoelasticity of cornea in animal ex vivo model using air-puff optical coherence tomography and corneal hysteresis. *J Biophotonics* 2019;12:e201800154.
9. Matalia J, Francis M, Gogri P, Panmand P, Matalia H, Sinha Roy A. Correlation of Corneal Biomechanical Stiffness With Refractive Error and Ocular Biometry in a Pediatric Population. *Cornea* 2017;36:1221-1226.

10. Matalia J, Francis M, Tejwani S, Dudeja G, Rajappa N, Sinha Roy A. Role of Age and Myopia in Simultaneous Assessment of Corneal and Extraocular Tissue Stiffness by Air-Puff Applanation. *J Refract Surg* 2016;32:486-493.
11. Nejad TM, Foster C, Gongal D. Finite element modelling of cornea mechanics: a review. *Arq Bras Oftalmol* 2014;77:60-65.
12. Francis M, Khamar P, Shetty R, et al. In Vivo Prediction of Air-Puff Induced Corneal Deformation Using LASIK, SMILE, and PRK Finite Element Simulations. *Invest Ophthalmol Vis Sci* 2018;59:5320-5328.
13. Mahendradas P, Francis M, Vala R, et al. Quantification of Ocular Biomechanics In Ocular Manifestations of Systemic Autoimmune Diseases. *Ocul Immunol Inflamm* 2018;1-11.
14. Pahuja N, Kumar NR, Francis M, et al. Correlation of Clinical and Biomechanical Outcomes of Accelerated Crosslinking (9 mW/cm<sup>2</sup>) in 10 minutes) in Keratoconus with Molecular Expression of Ectasia-Related Genes. *Curr Eye Res* 2016;41:1419-1423.
15. Shroff R, Francis M, Pahuja N, Veeboy L, Shetty R, Sinha Roy A. Quantitative Evaluation of Microdistortions in Bowman's Layer and Corneal Deformation after Small Incision Lenticule Extraction. *Transl Vis Sci Technol* 2016;5:12.
16. Chen C-C, Barnhart HX. Comparison of ICC and CCC for assessing agreement for data without and with replications. *Comput Stat Data Anal* 2008;53:554-564.

17. McBride G. A proposal for strength-of-agreement criteria for Lin's concordance correlation coefficient. *NIWA Client Report: HAM2005-062* 2005.
18. Boyce BL, Jones RE, Nguyen TD, Grazier JM. Stress-controlled viscoelastic tensile response of bovine cornea. *J Biomech* 2007;40:2367-2376.
19. Jannesari M, Mosaddegh P, Kadkhodaei M, Kasprzak H, Behrouz MJ. Numerical and clinical investigation on the material model of the cornea in Corvis tonometry tests: differentiation between hyperelasticity and viscoelasticity. *Mechanics of Time-Dependent Materials* 2018;1-12.
20. Wang LK, Tian L, Zheng YP. Determining in vivo elasticity and viscosity with dynamic Scheimpflug imaging analysis in keratoconic and healthy eyes. *J Biophotonics* 2016;9:454-463.
21. Nash IS, Greene PR, Foster CS. Comparison of mechanical properties of keratoconus and normal corneas. *Exp Eye Res* 1982;35:413-424.
22. Scarcelli G, Besner S, Pineda R, Kalout P, Yun SH. In vivo biomechanical mapping of normal and keratoconus corneas. *JAMA Ophthalmol* 2015;133:480-482.
23. Wu P-J, Kabakova IV, Ruberti JW, et al. Water content, not stiffness, dominates Brillouin spectroscopy measurements in hydrated materials. *Nature Methods* 2018;15:561-562.

24. Nguyen BA, Roberts CJ, Reilly MA. Biomechanical Impact of the Sclera on Corneal Deformation Response to an Air-Puff: A Finite-Element Study. *Front Bioeng Biotechnol* 2018;6:210.







## Chapter 4

---

# Corneal biomechanical changes and tissue remodeling after SMILE and LASIK

Shetty R, Francis M, Shroff R, Pahuja N, Khamar P, Girish M, Nuijts RMMA, Sinha Roy A

Invest Ophthalmol Vis Sci. 2017 Nov 1;58(13):5703-5712

**Purpose:** To evaluate transient corneal tissue healing and biomechanical changes between laser in situ keratomileusis (LASIK) and small incision lenticule extraction (SMILE) eyes

**Methods:** In each patient, one eye underwent LASIK and the other underwent SMILE. Optical coherence tomography (OCT) and dynamic Scheimpflug imaging (Corvis-ST) was used to assess tissue healing and biomechanics, respectively. Analyses of OCT scans yielded corneal speckle distribution (CSD) and Bowman's roughness index (BRI). Waveform analyses of deformation amplitude yielded corneal stiffness. Further, corneal force vs. corneal deformation data helped compare the two procedures.

**Results:** BRI increased and then decreased transiently after both treatments ( $p < 0.05$ ). However, SMILE eyes had similar BRI to their preoperative state compared to LASIK eyes at 6 month follow up. CSD indicated a marked increase in number of bright pixels and a decrease in the number of dark pixels after SMILE (1 month follow up) and LASIK eyes (3 month follow up), respectively. CSD returned to near preoperative state thereafter, respectively. Corneal stiffness change from preoperative state was similar between LASIK and SMILE eyes. However, deformation at discrete values of corneal force indicated some recovery of biomechanical strength after SMILE, but not in LASIK eyes.

**Conclusions:** BRI and CSD indicated earlier tissue healing in SMILE eyes than in LASIK. CSD results may indicate delayed cell death in LASIK eyes and increased light scatter due to interface fluid in SMILE eyes. Corneal biomechanical strength remodeled better in SMILE. This may indicate some hydration related recovery.

## Introduction

First reports of small incision lenticule extraction (SMILE) refractive surgery came in the year 2011<sup>1,2</sup>. The true implication of absence of a laser-assisted in situ keratomileusis (LASIK) flap in SMILE has been a subject of intense study. There were several clinical studies on biomechanical changes in the cornea after LASIK and SMILE<sup>3-6</sup>. A few reported similar biomechanical changes in the cornea after femtosecond LASIK and SMILE<sup>3-6</sup>. Other studies reported better biomechanical outcomes in SMILE eyes than in LASIK eyes<sup>7-10</sup>. Similarly, corneal tissue healing and Scheimpflug densitometry changes indicated a moderately better response in SMILE eyes<sup>11-13</sup>. These studies highlighted the need for improved analyses of information derived from current clinical devices to compare LASIK and SMILE outcomes.

Speckle distribution in optical coherence tomography (OCT) images of the cornea could assist in quantification of tissue level changes in patients<sup>14</sup>. The earlier studies used a probability distribution function (pdf) to describe the speckle distribution and then analyzed the change in pdf parameters as biomarkers of tissue response<sup>15,16</sup>. The OCT images were also a great source of corneal structural data. Micro-distortions in the Bowman's layer after SMILE indicated transient remodeling of the cornea<sup>17</sup>. We have developed the Bowman's roughness index (BRI) to quantitatively map the micro-distortions after

refractive surgery and in disease, e.g., keratoconus<sup>18,19</sup>. BRI indicated thinning of the Bowman's layer in keratoconus<sup>18,19</sup>. However, BRI indicated the presence of small amount of micro-distortions naturally before SMILE surgery and underwent a transient increase followed by decrease in magnitude postoperatively<sup>18,19</sup>. Since these tissue morphological changes occurred due to the surgery, these could also contribute to biomechanical changes in the cornea since ectasia may occur due to poor preoperative or lower residual biomechanical properties of the<sup>20</sup>. Current *in-vivo* biomechanical assessment options are the Corvis-ST (Oculus Optikgeräte GmbH, Wetzlar, Germany) and the Ocular Response Analyzer (ORA) (Reichert Ophthalmic Instruments, Buffalo, NY). Both the devices are air-puff applanation devices. However, correlation between ORA indices and mechanical corneal stiffness is unknown<sup>21,22</sup>. Using Corvis-ST, we can derive corneal stiffness, specific to the *in vivo* corneal deformation amplitude waveform<sup>23</sup>. Quantitative corneal stiffness was reported in myopic eyes<sup>23,24</sup>, keratoconic eyes before and after accelerated crosslinking<sup>25</sup>, and in eyes undergoing SMILE<sup>19</sup>. Therefore, the objectives of this study were: (1) to quantitatively map the biophysical changes in the cornea using OCT speckle distribution and BRI; (2) to quantitatively map the change in corneal stiffness with Corvis-ST and relate to biophysical changes. These quantifications were performed before and after refractive surgery, where one eye of the patient underwent LASIK and the other eye underwent SMILE. Thus, the study design was contralateral.

## Methods

The research study was longitudinal and prospective. The ethics committee of Narayana Nethralaya Multi-Specialty Eye Hospital, Bangalore, India approved the study. The study followed the tenets of Declaration of Helsinki. All participants provided written informed consent. The study included a total of 31 patients. One eye underwent SMILE while the other underwent LASIK. A random number generator assigned either SMILE or LASIK to an eye. Inclusion criteria were stable refraction (less than -10D equivalent refraction with astigmatism not more than -3D) for a period of one year (change less than 0.25D). Patients with less than 480  $\mu\text{m}$  central corneal thickness (CCT) or history of keratoconus, diabetes, collagen vascular disease, pregnancy, breastfeeding and any prior ocular surgery or trauma were excluded from the study. In all the eyes, calculated residual stromal thickness was greater than 250  $\mu\text{m}$ . All patients underwent refractive error assessment (sphere, cylinder and axis), Corvis-ST measurement and high resolution OCT imaging (Envisu, Leica Microsystems, Buffalo Grove, IL). If the patients were contact lens users, then contact lens use was discontinued for at least 2 weeks before measurements. Corvis-ST measurements were performed at preoperative, 1 month, 3 month and 6 month follow up. It was avoided at 1 week to avoid any patient discomfort. OCT imaging was performed at preoperative, 1 week, 1 month and once between the 3<sup>rd</sup> and 6<sup>th</sup> month follow up period. In our earlier study, OCT imaging had revealed near normalization of BRI by the 3<sup>rd</sup> month

follow up in SMILE patients<sup>18,19</sup>. Therefore, OCT imaging was repeated only once between the 3<sup>rd</sup> and 6<sup>th</sup> month follow up period to avoid unnecessary imaging.

### *Surgical procedure*

A single experienced surgeon performed all the surgeries under topical anesthesia using 0.5% proparacaine hydrochloride (Paracain, Sunways Pvt. Ltd., Mumbai, India) instilled 2–3 times. The WaveLight FS200 femtosecond laser and WaveLight EX500 excimer laser platform (Alcon Laboratories, Ft Worth, Texas, USA) cut the flap and ablated the tissue in one eye, respectively. The flap had a 9.0 mm diameter, 110  $\mu\text{m}$  thickness, a side cut angle of 70°, canal width of 1.5 mm and hinge position at 90°. Optical zone diameter was 6.0 mm. Targeted refractive error treatment reshaped the cornea with excimer laser after manual lifting of the flap. The VisuMax femtosecond laser system (Carl Zeiss Meditec AG, Germany) cut the cap and lenticule in the fellow eye. Cap thickness was 110  $\mu\text{m}$ . Lenticule and cap diameter was 6.0 mm and 7.7 mm, respectively. After creation of the refractive lenticule, it was dissected and extracted manually through a superior 3 mm side-cut. Cornea was remoistened with a wet merocel sponge at the end of the procedure. After the surgery, one drop of moxifloxacin hydro-chloride 0.5% (Vigamox®, Alcon Laboratories, Inc., Fort Worth, TX, USA) was applied to both eyes. Routine postoperative regimen was followed for both eyes. This included moxifloxacin hydrochloride 0.5% eye drops

(Vigamox®, Alcon Laboratories, Inc., Fort Worth, TX, USA) four times a day for 1 week, tapering doses of topical 1% Fluorometholone eye drops (Flarex®, Alcon Laboratories, Inc., Fort Worth, TX, USA) and topical lubricants (Optive, Allergan, Inc.) four times a day for three months.

### *Corneal biomechanical analyses*

An analytical biomechanical model analyzed the deformation amplitude waveform from Corvis-ST<sup>23,25</sup>. The analyses yielded the corneal stiffness<sup>23,25</sup>. The model reported two measures of stiffness: a linear corneal stiffness [Kc (constant), unit N/m] and a mean corneal stiffness [Kc (mean), unit N/m]<sup>23,25</sup>. In classical biomechanics, analyses of the *ex vivo* stress vs. strain curves provided the tissue biomechanical properties. Therefore, we analyzed the air-pressure force absorbed by the cornea, named as the corneal force, and the corneal deformation only<sup>23,25</sup>. Here, corneal force and corneal deformation were considered analogous to stress and strain, respectively. At each time point for a given eye, the data were regressed with a third order polynomial equation. All regressions achieved a minimum  $R^2=0.98$ . At each time point, the equations for all the eyes were averaged to obtain the mean corneal force vs. corneal deformation response for the two cohorts (LASIK and SMILE). Using the mean corneal force vs. corneal deformation data, the mean corneal deformation at a mean corneal force



of 0.10, 0.15, 0.20 and 0.25N was calculated at each time point. These were compared between the treatment cohorts.

### *OCT image analyses*

Analyses of the OCT images yielded BRI<sup>18,19</sup> and speckle distribution. BRI was a measure of roughness of the Bowman's layer<sup>18,19</sup>. Postoperatively, this roughness was expected to be higher in the acute healing phase after surgery<sup>18,19</sup>. To analyze the speckle distribution, only the raw OCT images were used. The scan size was limited to 3 mm in the high resolution mode. The procedure to acquire the OCT images was discussed previously<sup>18</sup>. The Bioptigen InVivoVue 2.2.22 reader software exported the raw images for further analyses. The aspect ratio of the exported images was maintained for the analyses. Preoperatively, the cornea had a healthy tear film. However, the postoperative dryness, along the anterior surface, caused additional scattering in the total image. Therefore, the analyses of the speckle distribution were performed by two methods.

In the 1<sup>st</sup> method, a probability distribution function (pdf), without any noise correction, mapped the speckle distribution. Figure 1a shows a gray scale representation of the uncorrected image. The image region within the anterior and posterior corneal edge was selected (Figure 1b). The regions above (air) and below (aqueous humor) the cornea are shown in Figure 1c with pseudo-coloring. The pdf's mapped

the speckle distribution of air, cornea and aqueous humor (Figures 1d, e and f, respectively). Here, the pdf calculated for the uncorrected corneal image was the 1<sup>st</sup> method. This method was applied to both pre and postoperative time points. In the 2<sup>nd</sup> method, a corrected corneal image resulted from subtraction of the speckle distribution of the air and aqueous humor from the “whole image” speckle distribution (Figure 6g and h in gray scale and pseudo-coloring, respectively). The same probability distribution function (pdf) mapped the speckle distribution of corrected corneal image (Figure 1i). From Figures 1g and h, it was evident that the air and aqueous humor had negligible speckle after correction. The 2<sup>nd</sup> method was also applied to both pre and postoperative states. Thus at any given time point, two pdf's for the cornea were calculated, one for the uncorrected and the other for the corrected OCT image.

The generalized extreme value (GEV) pdf (equation 1) captured the tails (i.e. speckle distribution at or near the highest intensity of 255) of different shapes accurately<sup>26</sup>. Pixel intensity ranged from 0 to 255 in the OCT images. Therefore, it was necessary to model both extremes of intensity with a suitable mathematic function. The GEV was a three parameter function:  $\mu$  ( $-\infty \leq \mu \leq \infty$ ),  $\sigma$  ( $\sigma \geq 0$ ) and  $k$  ( $-\infty \leq k \leq \infty$ ). Here, these parameters represent location, scale and shape, respectively<sup>26</sup>. The value of  $k$  described the shape of the distribution, e.g.,  $k=0$  represented the Gumbel distribution,  $k>0$  represented the Frechet distribution and  $k<0$  was the Weibull distribution. The tail of the pdf described the

number of the pixels with higher intensity. The Gumbel distribution, also known as GEV type 1 distribution, described an exponentially decreasing tail better, similar to a normal distribution. The Weibull distribution (type 3) described a tail of finite length. The Frechet distribution (type 2) was suited for distributions with very small tails. Scale parameter ( $\sigma$ ) influenced the maximum height of the pdf. When  $\sigma$  reduced, the number of high intensity pixels decreased and low intensity pixels increased. Location parameter ( $\mu$ ) influenced the location of the peak of the pdf along the x-axis of the distribution. If  $\mu$  increased, the peak moved towards the highest intensity (pixel value of 255) and vice versa.

$$f(x) = \begin{cases} \frac{1}{\sigma} \left( 1 + k \frac{(x-\mu)}{\sigma} \right)^{-1-\frac{1}{k}} e^{\left( -\left( 1+k \frac{(x-\mu)}{\sigma} \right)^{-\frac{1}{k}} \right)} & \text{for } k \neq 0 \\ \frac{1}{\sigma} e^{\left( -e^{\left( -\frac{(x-\mu)}{\sigma} \right)} \right)} - \frac{(x-\mu)}{\sigma} & \text{for } k = 0 \end{cases} \dots\dots (1)$$

The GEV distribution parameters ( $\sigma$ ,  $k$ ,  $\mu$ ) were computed using maximum likelihood estimation<sup>27</sup>. For each eye, 3 scans were acquired at each time point to assess repeatability of BRI<sup>18</sup>,  $\sigma$ ,  $k$  and  $\mu$ . To analyze the difference between the cohort of LASIK and SMILE eyes, the means of the GEV distribution parameters ( $\sigma$ ,  $k$  and  $\mu$ ) were used. These mean values yielded the mean speckle distributions for the LASIK and SMILE cohort at different time points.

The normality of the data was confirmed with Shapiro-Wilk test. Repeated measures analysis of variance (ANOVA) was used to study

the change after the surgery in the LASIK and SMILE cohorts. Repeatability of the data was analyzed with intra-class correlation coefficient (ICC). The mean  $\pm$  standard error of the parameters was calculated. A p-value less than 0.05 was considered statistically significant. All statistical calculations were performed using MedCalc v17.6 software (MedCalc Software, Ostend, Belgium).

## Results

The mean age of the patients was  $24 \pm 1$  years. The manifest refraction spherical equivalent (MRSE) [ $-7.22 \pm 1.32D$  and  $-6.18 \pm 0.41D$  for LASIK and SMILE respectively;  $p=0.45$ ], intraocular pressure (IOP) [ $13.5 \pm 0.46$  mmHg and  $13.0 \pm 0.45$  mmHg for LASIK and SMILE, respectively;  $p=0.41$ ] and central corneal thickness (CCT) [ $517 \pm 4.89$   $\mu$ m and  $514.18 \pm 4.5$   $\mu$ m for LASIK and SMILE respectively;  $p=0.67$ ] were similar between the eyes. The ratio of female to male patients was 1.21 (17 female and 14 male patients). The ICC of BRI,  $k$ ,  $\sigma$  and  $\mu$  for each zone (air, aqueous humor and cornea) were greater than 0.95, indicating high repeatability. Table 1 shows the mean  $\pm$  standard error of  $k$ ,  $\sigma$  and  $\mu$  of the cornea, before and after correction. Most parameters ( $k$ ,  $\sigma$  and  $\mu$ ) were similar ( $p>0.05$ ) between the time points, irrespective of the procedure (LASIK or SMILE). In the corrected corneal image, only  $\sigma$  showed a significant temporal decrease in the LASIK eyes at 1 month ( $p=0.03$  in Table 1). In SMILE, an

increase in  $\sigma$  was observed at 1 week after surgery but this increase wasn't statistically significant. Since most parameters in Table 1 did not achieve statistical significance, we used the mean values of  $k$ ,  $\sigma$  and  $\mu$  to plot the mean corneal speckle distributions for the LASIK and SMILE cohort eyes.

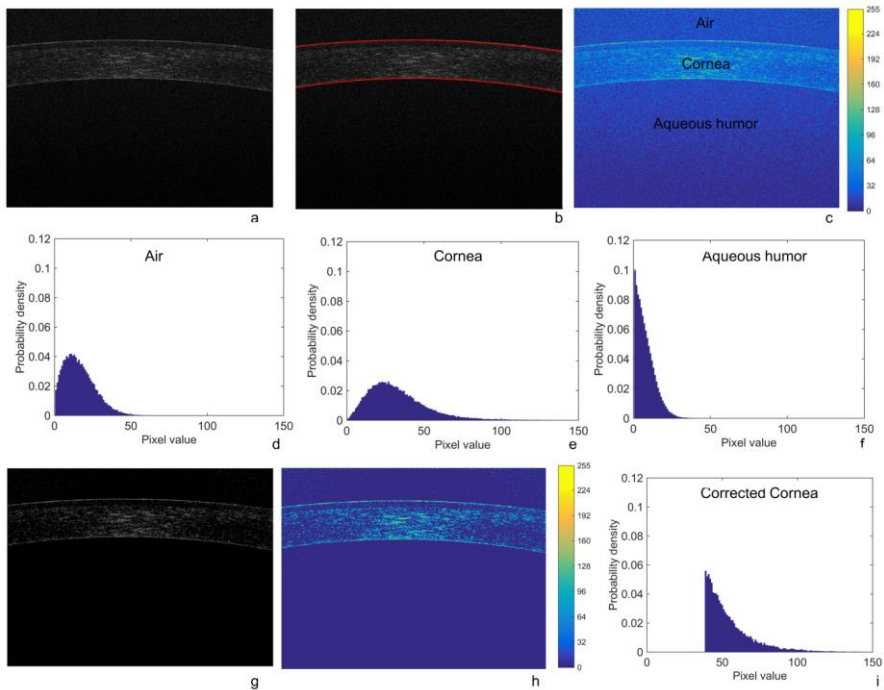


Figure 1: An OCT scan of the cornea without (a) and with (b) detected bounding edges. The same with pseudo colors is shown in (c) showing the air, cornea and aqueous humor. Figure (d), (e) and (f) show the speckle distribution of air, cornea and aqueous humor regions, respectively. Figure (e) and (f) shows the same image after correction and with pseudo coloring, respectively. Figure (g) shows the corneal speckle distribution after image correction.

Table 1: Optical coherence tomography (OCT) speckle parameters from uncorrected and corrected corneal images.

LASIK				
	Preoperative	1 week	1 month	3 month and beyond
Corneal probability density function parameters from uncorrected image				
k	$0.06 \pm 0.02$	$0.07 \pm 0.01$	$0.05 \pm 0.01$	$0.08 \pm 0.01$
$\sigma$	$14.37 \pm 0.68$	$14.69 \pm 0.82$	$13.22 \pm 0.69$	$15.28 \pm 0.92$
$\mu$	$25.29 \pm 1.44$	$25.8 \pm 1.62$	$22.35 \pm 1.1$	$24.28 \pm 1.38$
Corneal probability density function parameters from corrected image				
k	$0.41 \pm 0.02$	$0.42 \pm 0.02$	$0.44 \pm 0.02$	$0.44 \pm 0.03$
$\sigma$	$8.72 \pm 0.54$	$8.66 \pm 0.52$	$7.44 \pm 0.37$	$9.68 \pm 0.64$
$\mu$	$45.73 \pm 1.02$	$46.92 \pm 1.41$	$43.36 \pm 1.08$	$46.13 \pm 1.44$

Table 1: continued

SMILE					
Preoperative	1 week	1 month	3 month and beyond	p-value LASIK	p-value SMILE
Corneal probability density function parameters from uncorrected image					
$0.03 \pm 0.01$	$0.05 \pm 0.01$	$0.06 \pm 0.01$	$0.04 \pm 0.01$	0.64	0.39
$14.3 \pm 0.64$	$16.27 \pm 0.92$	$14.47 \pm 0.75$	$14.71 \pm 0.91$	0.30	0.33
$25.94 \pm 1.43$	$28.92 \pm 1.97$	$25.43 \pm 1.55$	$26.15 \pm 1.79$	0.32	0.49
Corneal probability density function parameters from corrected image					
$0.37 \pm 0.02$	$0.37 \pm 0.02$	$0.42 \pm 0.02$	$0.4 \pm 0.02$	0.64	0.19

Corneal biomechanical changes and tissue remodeling

$8.36 \pm 0.47$	$10.05 \pm 0.65$	$8.21 \pm 0.38$	$8.81 \pm 0.68$	0.03*	0.12
$44.82 \pm 1.29$	$48.31 \pm 1.50$	$45.06 \pm 0.9$	$44.47 \pm 1.19$	0.23	0.12

$\sigma$ ,  $k$ ,  $\mu$ : generalized extreme value distribution parameters; \*indicates statistically significant difference.

Table 2: Change (preoperative minus postoperative) in corneal deformation levels at different applied corneal force computed using the analytical biomechanical model.

Corneal force	LASIK		
	1 month (mm)	3 month (mm)	6 month (mm)
0.10N	$-0.07 \pm 0.01$	$-0.06 \pm 0.01$	$-0.06 \pm 0.02$
0.15N	$-0.06 \pm 0.01$	$-0.04 \pm 0.01$	$-0.04 \pm 0.02$
0.20N	$-0.07 \pm 0.02$	$-0.05 \pm 0.01$	$-0.04 \pm 0.02$
0.25N	$-0.09 \pm 0.02$	$-0.06 \pm 0.02$	$-0.05 \pm 0.02$

Table 2: continued

SMILE			p-value LASIK	p-value SMILE
1 month (mm)	3 month (mm)	6 month (mm)		
$-0.1 \pm 0.01$	$-0.08 \pm 0.01$	$-0.08 \pm 0.02$	0.71	0.47
$-0.08 \pm 0.01$	$-0.06 \pm 0.01$	$-0.04 \pm 0.02$	0.47	0.12
$-0.09 \pm 0.01$	$-0.05 \pm 0.02$	$-0.022 \pm 0.017$	0.41	0.03*
$-0.1 \pm 0.02$	$-0.06 \pm 0.02$	$-0.022 \pm 0.021$	0.43	0.03*

\*indicates statistically significant difference.

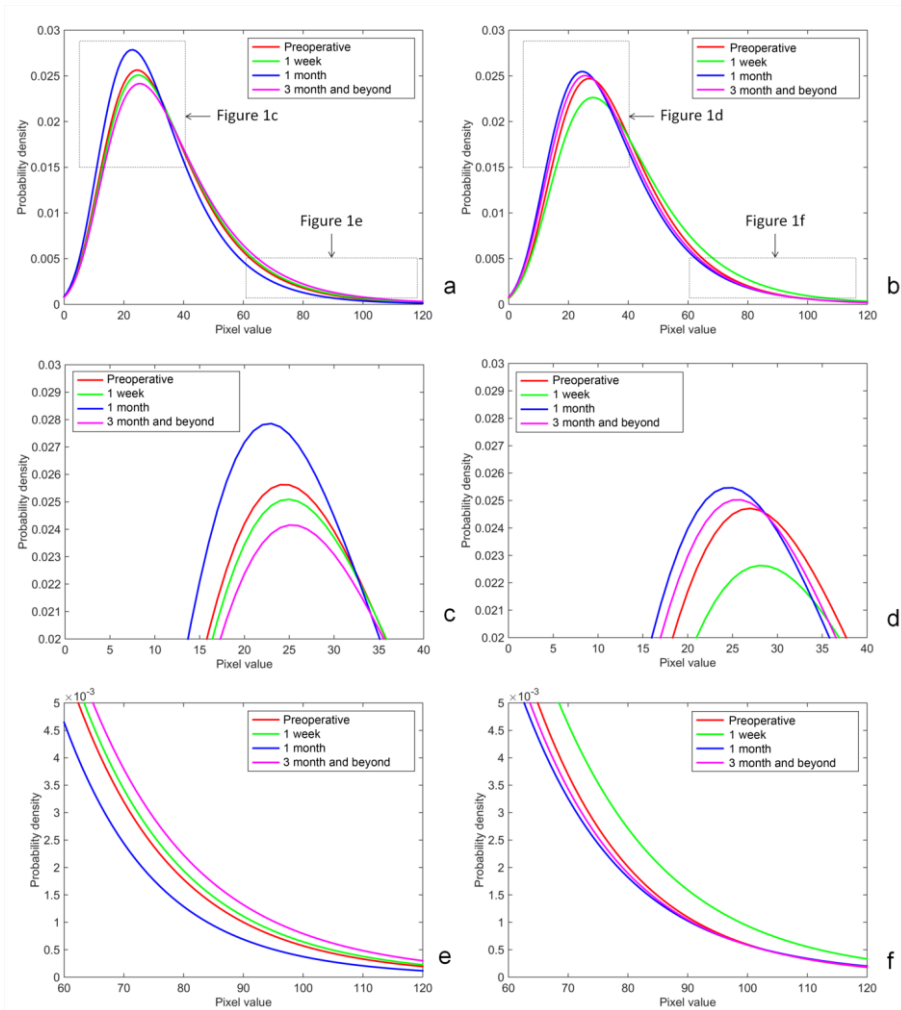


Figure 2: Uncorrected mean speckle probability distribution function (pdf) in LASIK (a) and SMILE (b) eyes. The magnified peak and tail section of LASIK (c and e, respectively) and SMILE (d and f, respectively) eyes are shown as well. Data for all time points are plotted



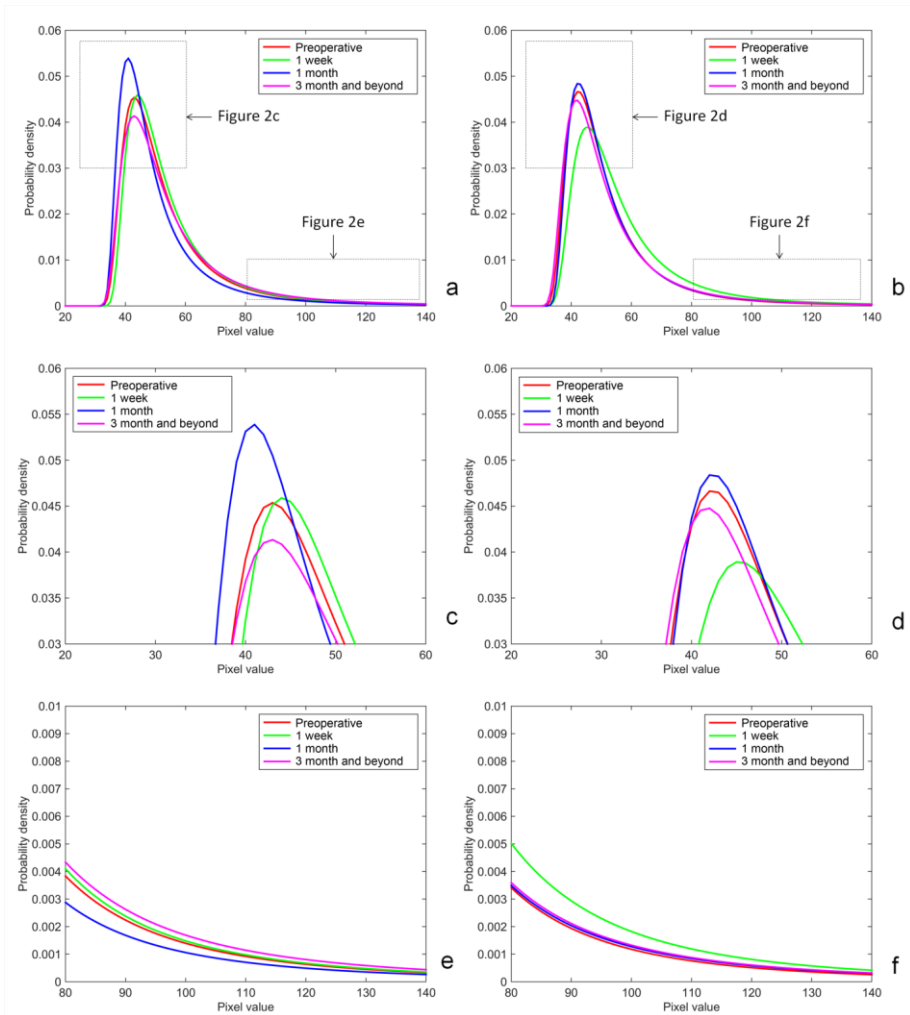


Figure 3: Corrected mean speckle probability distribution function (pdf) in LASIK (a) and SMILE (b) eyes. The magnified peak and tail section of LASIK (c and e, respectively) and SMILE (d and f, respectively) eyes are shown as well.

Using the uncorrected corneal images, Figures 2a and b show the mean distributions for LASIK and SMILE eyes, respectively. We focused on two regions of the distributions as shown in inset (Figures 2a and b). Figures 2c and e show the magnified regions of the distributions plotted in Figure 2a (LASIK eyes). Figures 2d and f show the magnified regions of the distributions plotted in Figure 2b (SMILE eyes). In LASIK eyes (Figure 2c), there was a sharp increase in peak of the distribution from preoperative (red line) to 1 month (blue line). At 3 month, the peak (purple line) reduced below the peak of the preoperative distribution (Figure 2c). An increase in peak of the distribution logically would indicate more pixels in the high intensity pixel range since the total number of pixels in each image was the same at all time points. This was evident in Figure 1e, where the number of pixels in the high intensity regions was the least at 1 month (blue line). At other time points (Figure 2e), the number of pixels was approximately the same [preoperative (red line), 1 week (green line) and beyond 3 month (purple line)]. In SMILE eyes, a marked decrease in peak of the distribution (green line in Figure 2d) and increase in the number of pixels in the high intensity region (green line in Figure 2f) at 1 week showed up postoperatively. Thereafter, the distributions at 1 month (blue line in Figures 2d and f) and beyond 3 months (purple line in Figures 2d and f) were similar to the preoperative distribution (red line in Figures 2d and f). Interestingly, the corrected corneal images showed the same trends as well (Figure 3). Thus, the speckle distribution indicated a longer duration remodeling of the cornea in LASIK eyes than in SMILE eyes.

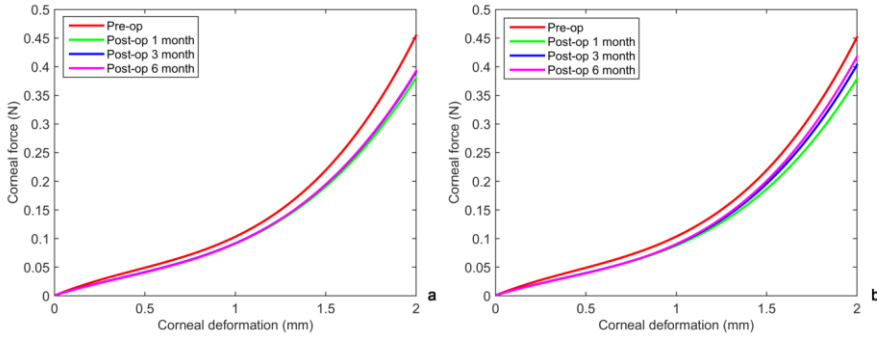


Figure 4: Mean corneal force vs. corneal deformation response of LASIK (a) and SMILE (b) eyes at different time points.

In LASIK eyes, mean BRI was  $1.72 \times 10^{-3} \pm 1.31 \times 10^{-4} \text{ mm}^2$ ,  $4.49 \times 10^{-3} \pm 1.35 \times 10^{-4} \text{ mm}^2$ ,  $3.21 \times 10^{-3} \pm 1.27 \times 10^{-4} \text{ mm}^2$  and  $2.49 \times 10^{-3} \pm 1.18 \times 10^{-4} \text{ mm}^2$  at preoperative, 1 week, 1 month and 3 month plus follow up, respectively. Further, mean BRI differed significantly between all the time points, when analyzed pair wise ( $p=0.001$ ). Interestingly in LASIK eyes, mean BRI beyond 3 months was still greater than the preoperative magnitude. In SMILE eyes, BRI was  $2.31 \times 10^{-3} \pm 1.29 \times 10^{-4} \text{ mm}^2$ ,  $4.52 \times 10^{-3} \pm 1.41 \times 10^{-4} \text{ mm}^2$ ,  $4.01 \times 10^{-3} \pm 1.29 \times 10^{-4} \text{ mm}^2$  and  $2.54 \times 10^{-3} \pm 1.18 \times 10^{-4} \text{ mm}^2$ , respectively. In SMILE eyes, the trends were similar between the time points ( $p=0.001$ ) except between preoperative and 3 month plus follow up ( $p>0.05$ ). In other words, BRI beyond 3 months had returned to preoperative magnitudes in most eyes. Thus, postoperative wound healing appeared to be better in SMILE eyes than in LASIK eyes.

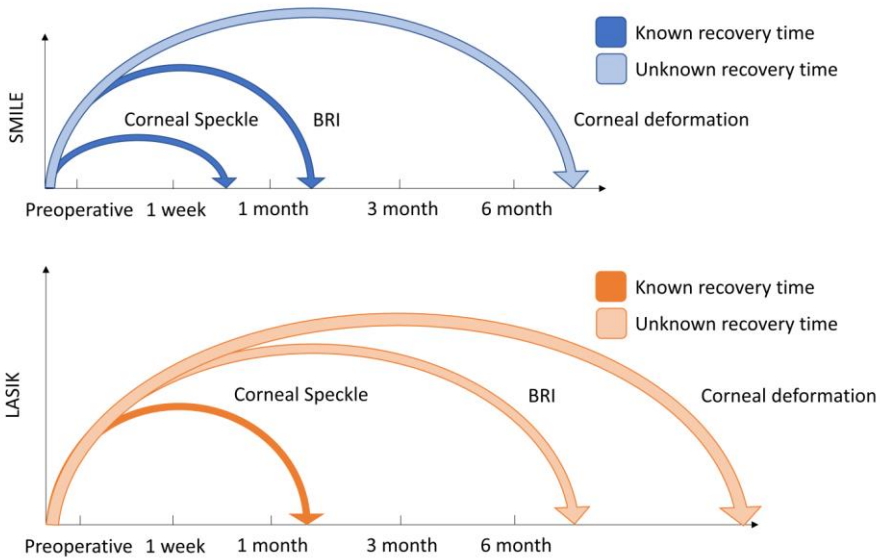


Figure 5: A schematic representation of transient changes in study parameters between SMILE and LASIK eyes.

Biomechanical analyses of the eyes yielded interesting results. In LASIK eyes, the  $k_c$  (constant) was  $103.87 \pm 1.55$  N/m,  $92.37 \pm 1.95$  N/m,  $93.67 \pm 1.48$  N/m and  $91.39 \pm 2.41$  N/m at preoperative, postoperative 1 month, postoperative 3 month and postoperative 6 month, respectively. In SMILE eyes, the same was  $102.75 \pm 1.39$  N/m,  $90.02 \pm 1.68$  N/m,  $92.14 \pm 1.66$  N/m and  $89.5 \pm 2.09$  N/m at preoperative, postoperative 1 month, postoperative 3 month and postoperative 6 month, respectively. In LASIK eyes,  $k_c$  (mean) was  $101.8 \pm 1.84$  N/m,  $85.85 \pm 2$  N/m,  $86.23 \pm 1.78$  N/m and  $84.03 \pm 2.29$  N/m at preoperative, postoperative 1 month, postoperative 3 month and postoperative 6 month, respectively. In SMILE eyes, the same was

$100.37 \pm 1.85$  N/m,  $83.04 \pm 1.82$  N/m,  $83.41 \pm 1.94$  N/m and  $79.64 \pm 2.09$  N/m at preoperative, postoperative 1 month, postoperative 3 month and postoperative 6 month, respectively. In LASIK eyes, there was significant decrease in stiffness between pre and postoperative states ( $p < 0.001$ ), but not between the postoperative time points ( $p > 0.05$ ). The SMILE eyes showed the same trends.

Since changes in stiffness parameters were similar between LASIK and SMILE, the mean values of derived biomechanical model parameters<sup>23,25</sup> yielded the mean corneal force vs. corneal deformation curves at all time points. Figures 4a and b show these plots for LASIK and SMILE eyes. We evaluated these plots at discrete values of force and the corresponding corneal deformation was derived from Figures 4a and b (Table 3). At a force of 0.10 and 0.15 N and in LASIK eyes, change (= preoperative – postoperative time point) in corneal deformation was similar at all postoperative time points (Table 3:  $p = 0.71$  and  $0.47$ , respectively). The SMILE eyes showed the same trends (Table 3:  $p = 0.47$  and  $0.12$ , respectively). In LASIK eyes, the trend was same at higher corneal forces of 0.20 and 0.25N. However in SMILE eyes, there was a significant decrease in change in corneal deformation from 1 month ( $\sim -0.1$  mm) to 6 month ( $\sim -0.022$  mm). This could indicate a better remodeling of the collagen matrix in SMILE eyes than in LASIK eyes (similar to BRI). These results were also evident upon careful visual examination of Figures 4a and b.

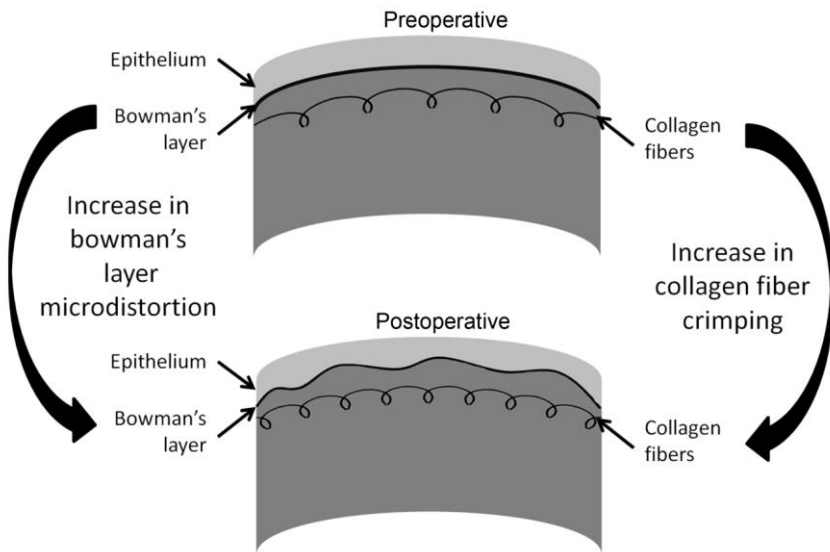


Figure 6: A schematic representation of remodeling of collagen fibers in the flap/cap region of the stroma showing the increase in microdistortions in Bowman's layer and crimping of collagen fibers.

## Discussion

The cornea is a complex tissue, where a delicate balance between mechanical and fluid stresses determines its shape and function. This complexity impacts the transient wound healing and deformation response after LASIK and SMILE. We presented novel applications of OCT imaging biomarkers to assess tissue level changes in the cornea. Based on BRI and corneal speckle distribution, both LASIK and SMILE caused structural changes. Figures 5a and b provide

a schematic representation of the transient wound healing and biomechanical changes in SMILE and LASIK eyes, respectively. In SMILE eyes, post operative corneal speckle changed up to 1 week and was nearly back to preoperative distribution by 1 month (Figure 5a). In case of BRI, the return to preoperative levels was achieved by the 3<sup>rd</sup> month. However, corneal deformation continued to remodel up to the 6<sup>th</sup> month follow up and possibly beyond (Figure 5a). In LASIK eyes, corneal speckle normalized by the 3<sup>rd</sup> month follow up (Figure 5b). However, BRI and corneal deformation possibly continued to remodel even after the 6<sup>th</sup> month follow up. This is the first study to present these interesting features of corneal wound healing and biomechanics.

A recent study used corneal densitometry from Scheimpflug imaging to analyze transient healing of the cornea after photorefractive keratectomy (PRK), LASIK and SMILE<sup>12</sup>. The mean postoperative total corneal densitometry values were  $15.53 \pm 1.65$ ,  $16.53 \pm 1.94$  and  $16.10 \pm 1.54$ , respectively<sup>12</sup>. Thus, the procedures caused similar densitometry changes<sup>12</sup>. Scheimpflug imaging uses visible light for densitometry and has lower axial resolution compared to OCT. In contrast, LASIK and SMILE caused different structural responses in this study. This could be due to differences between infrared light and tissue interaction coupled with better axial resolution of OCT. BRI was another novel index to quantify the micro-distortions in the Bowman's layer<sup>12</sup>. BRI was greater after both SMILE and LASIK due to surgical manipulations in LASIK and compression of the cap in SMILE.

Therefore, we hypothesized structural changes in the flap/cap region (Figure 6).

Preoperatively (Figure 6), the helical collagen fibers were under tension<sup>27</sup>. Under stress relaxation (due to surgical severance of collagen fibers), the fibers could undergo a crimping effect<sup>26</sup>. This is shown by the compression of the spring postoperatively (Figure 6a). In other words, this could possibly lead to an increase in BRI (Figure 6a). As the cornea remodeled further, the collagen fibers relaxed and possibly resulted in a lower BRI (Figure 6b). In SMILE, only a small number of fibers in the cap were cut. This could explain the faster relaxation of the fibers in SMILE. However, LASIK severed a much larger number of fibers. This could have significantly delayed the return of BRI to preoperative levels. It would be interesting to study if BRI recovered after LASIK in the long term, similar to SMILE (Figure 5). By design, SMILE was a less invasive procedure than LASIK. Therefore, it was logical to hypothesize significant biomechanical advantage of SMILE over LASIK. Studies have reported mixed results on change in corneal biomechanical parameters after SMILE and LASIK<sup>12</sup>. A contralateral eye study on SMILE vs. LASIK reported similar change in CH and CRF between the eyes<sup>12</sup>. In this study as well, change in corneal stiffness was similar between the eyes. However, stiffness was an aggregate marker of the non-linear stress vs. strain response of the patient cornea<sup>12</sup>. Therefore, discrete locations on the mean corneal force vs. corneal deformation curves (Figure 4) were analyzed. At low corneal forces



where the deformation response of the cornea may be linear, the change in deformation was barely different between the LASIK and SMILE eyes (Figure 4). However, at higher forces, the SMILE corneas showed a clear trend towards some recovery of the biomechanical strength at follow up (Figure 4). Interestingly at high forces, the collagen fibers bear some of the mechanical stress. This could be correlated to differences between SMILE and LASIK eyes with respect to transient changes in BRI.

Our analytical model revealed interesting results between myopic eyes from different populations<sup>12</sup>. In this study, transient changes in BRI, corneal speckle and corneal deformation in SMILE eyes indicated a strong inter-dependence between these corneal properties, e.g., BRI and cornea speckle returned to preoperative levels by the 3<sup>rd</sup> month and coupled with transient changes in corneal deformation in SMILE eyes. In LASIK, this wasn't observed. Thus, flap and excimer ablation in LASIK could have caused these observations. Excimer ablation may result in greater hydration changes. Transient decrease in number of high intensity pixels could indicate greater (detectable by OCT) keratocyte death in the stroma of LASIK eyes<sup>28</sup>. In contrast, transient increase in high intensity pixels in the SMILE eyes could indicate the presence of some interface fluid in the acute phase after surgery. This could lead to increased light scatter from the stroma and maybe transient complications after SMILE in few eyes<sup>29,30</sup>. These transient complications may not be visible on slit lamp<sup>29</sup> but OCT

speckle distribution may detect these changes. There is evidence in literature to support the speckle distribution results. SMILE generally caused less keratocytes apoptosis, less proliferation, less inflammation and faster regeneration of nerve density than LASIK and PRK<sup>31-33</sup>. Interestingly, keratocyte apoptosis was observed both above and below the flap interface deep in the tissue after LASIK<sup>31</sup>. However, the same was localized to the lenticular interfaces only after SMILE and the surrounding tissue showed minimal apoptic effect in the early phase of wound healing<sup>34</sup>. Thus, regional analyses of speckle distribution within the stroma could be useful in highlighting these changes since OCT was non-invasive compared to confocal microscopy. Further, speckle distribution analyses can be performed with any commercial OCT scanner since all have access to the raw (non-averaged) OCT images. Therefore, speckle distribution may have a role in the clinic. To conclude, this study introduced better understanding of the transient healing process after LASIK and SMILE using non-invasive imaging in patient eyes and showed a better recovery after SMILE than LASIK, biomechanically and biophysically. A longer follow up and analyses with advanced methods, such as inverse finite element models, could reveal more interesting features of wound healing<sup>12</sup>.

### **Author Contributions**

**Francis M** and **Girrish M** performed data analyses and writing of the manuscript. **Shroff R**, **Pahuja N**, **Khamar P** and **Shetty R** performed

the surgeries, clinical data collection and writing of the manuscript. **Nuijts RMMA** performed critical review of the manuscript. **Shetty R** and **Sinha Roy A** performed design of the study, writing and final review of the manuscript.

## References

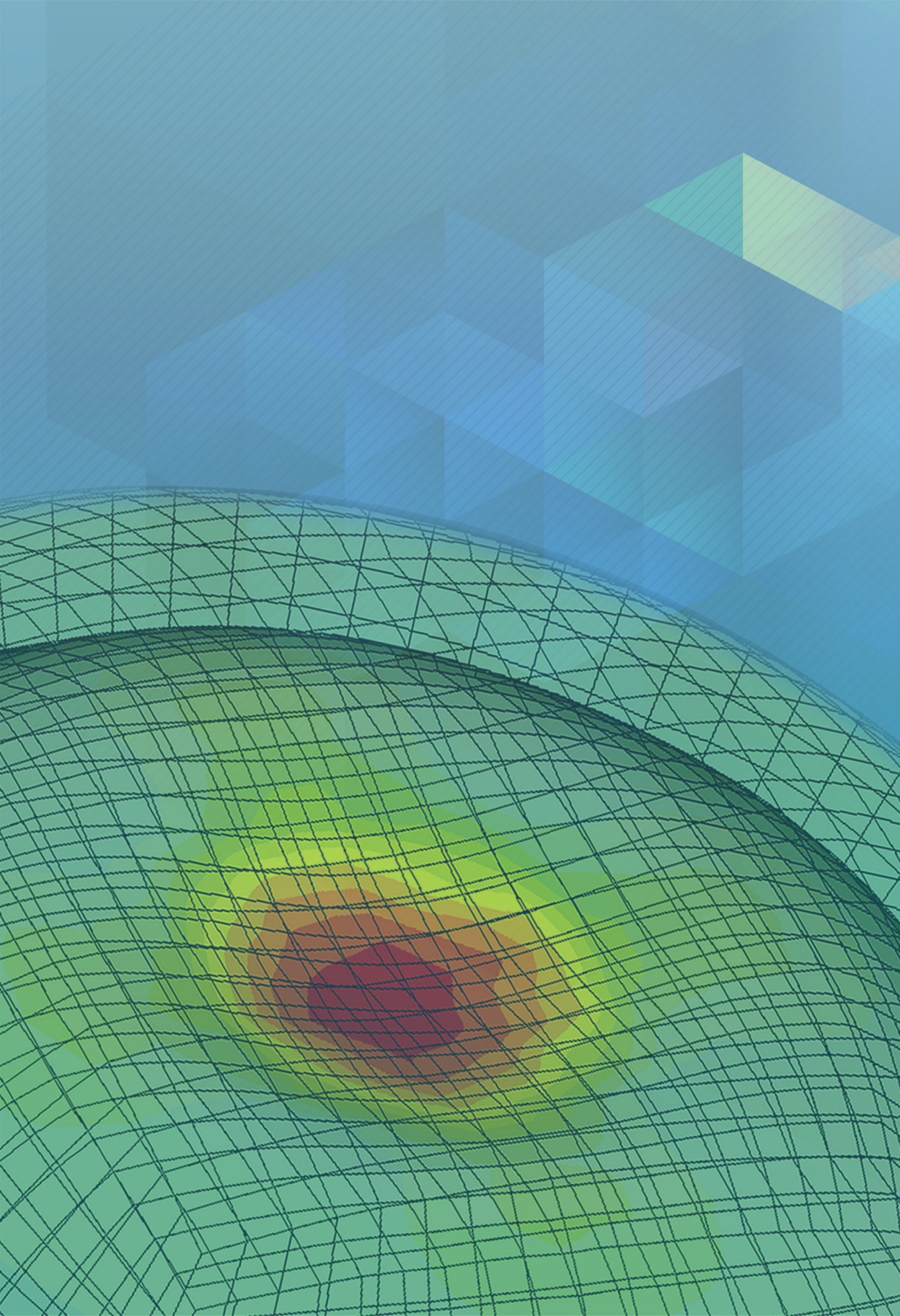
1. Shah, R., Shah, S. & Sengupta, S. Results of small incision lenticule extraction: All-in-one femtosecond laser refractive surgery. *J Cataract Refract Surg* **37**, 127-137, doi:10.1016/j.jcrs.2010.07.033 (2011).
2. Sekundo, W., Kunert, K. S. & Blum, M. Small incision corneal refractive surgery using the small incision lenticule extraction (SMILE) procedure for the correction of myopia and myopic astigmatism: results of a 6 month prospective study. *The British journal of ophthalmology* **95**, 335-339, doi:10.1136/bjo.2009.174284 (2011).
3. Zhang, J., Zheng, L., Zhao, X., Xu, Y. & Chen, S. Corneal biomechanics after small-incision lenticule extraction versus Q-value-guided femtosecond laser-assisted in situ keratomileusis. *Journal of current ophthalmology* **28**, 181-187, doi:10.1016/j.joco.2016.08.004 (2016).
4. Sefat, S. M. *et al.* Evaluation of Changes in Human Corneas After Femtosecond Laser-Assisted LASIK and Small-Incision Lenticule Extraction (SMILE) Using Non-Contact Tonometry

- and Ultra-High-Speed Camera (Corvis ST). *Current eye research* **41**, 917-922, doi:10.3109/02713683.2015.1082185 (2016).
5. Pedersen, I. B., Bak-Nielsen, S., Vestergaard, A. H., Ivarsen, A. & Hjortdal, J. Corneal biomechanical properties after LASIK, ReLEx flex, and ReLEx smile by Scheimpflug-based dynamic tonometry. *Graefe's archive for clinical and experimental ophthalmology = Albrecht von Graefes Archiv fur klinische und experimentelle Ophthalmologie* **252**, 1329-1335, doi:10.1007/s00417-014-2667-6 (2014).
  6. Agca, A. *et al.* Comparison of corneal hysteresis and corneal resistance factor after small incision lenticule extraction and femtosecond laser-assisted LASIK: a prospective fellow eye study. *Contact lens & anterior eye : the journal of the British Contact Lens Association* **37**, 77-80, doi:10.1016/j.clae.2013.05.003 (2014).
  7. Osman, I. M., Helaly, H. A., Abdalla, M. & Shousha, M. A. Corneal biomechanical changes in eyes with small incision lenticule extraction and laser assisted in situ keratomileusis. *BMC ophthalmology* **16**, 123, doi:10.1186/s12886-016-0304-3 (2016).
  8. Wang, B. *et al.* Comparison of the change in posterior corneal elevation and corneal biomechanical parameters after small incision lenticule extraction and femtosecond laser-assisted LASIK for high myopia correction. *Contact lens & anterior eye*

- : *the journal of the British Contact Lens Association* **39**, 191-196, doi:10.1016/j.clae.2016.01.007 (2016).
9. Wang, D. *et al.* Differences in the corneal biomechanical changes after SMILE and LASIK. *Journal of refractive surgery* **30**, 702-707, doi:10.3928/1081597X-20140903-09 (2014).
  10. Wu, D., Wang, Y., Zhang, L., Wei, S. & Tang, X. Corneal biomechanical effects: small-incision lenticule extraction versus femtosecond laser-assisted laser in situ keratomileusis. *Journal of cataract and refractive surgery* **40**, 954-962, doi:10.1016/j.jcrs.2013.07.056 (2014).
  11. Xia, L., Zhang, J., Wu, J. & Yu, K. Comparison of Corneal Biological Healing After Femtosecond LASIK and Small Incision Lenticule Extraction Procedure. *Current eye research* **41**, 1202-1208, doi:10.3109/02713683.2015.1107590 (2016).
  12. Poyales, F. *et al.* Corneal densitometry after photorefractive keratectomy, laser-assisted in situ keratomileusis, and small-incision lenticule extraction. *Eye*, doi:10.1038/eye.2017.107 (2017).
  13. Agca, A. *et al.* Fellow Eye Comparison of Nerve Fiber Regeneration After SMILE and Femtosecond Laser-assisted LASIK: A Confocal Microscopy Study. *J Refract Surg* **31**, 594-598, doi:10.3928/1081597x-20150820-04 (2015).
  14. Lindenmaier, A. A. *et al.* Texture analysis of optical coherence tomography speckle for characterizing biological tissues in vivo. *Opt Lett* **38**, 1280-1282, doi:10.1364/OL.38.001280 (2013).

15. Jesus, D. A. & Iskander, D. R. Assessment of corneal properties based on statistical modeling of OCT speckle. *Biomed Opt Express* **8**, 162-176, doi:10.1364/BOE.8.000162 (2017).
16. Sugita, M., Weatherbee, A., Bizheva, K., Popov, I. & Vitkin, A. Analysis of scattering statistics and governing distribution functions in optical coherence tomography. *Biomed Opt Express* **7**, 2551-2564, doi:10.1364/BOE.7.002551 (2016).
17. Yao, P. *et al.* Microdistortions in Bowman's layer following femtosecond laser small incision lenticule extraction observed by Fourier-Domain OCT. *J Refract Surg* **29**, 668-674, doi:10.3928/1081597X-20130806-01 (2013).
18. Pahuja, N. *et al.* Application of high resolution OCT to evaluate irregularity of Bowman's layer in asymmetric keratoconus. *Journal of biophotonics* **10**, 701-707, doi:10.1002/jbio.201600106 (2017).
19. Shroff, R. *et al.* Quantitative Evaluation of Microdistortions in Bowman's Layer and Corneal Deformation after Small Incision Lenticule Extraction. *Translational vision science & technology* **5**, 12, doi:10.1167/tvst.5.5.12 (2016).
20. Kling, S. & Hafezi, F. Corneal biomechanics - a review. *Ophthalmic Physiol Opt* **37**, 240-252, doi:10.1111/opo.12345 (2017).
21. Roy, A. S., Shetty, R. & Kummelil, M. K. Keratoconus: a biomechanical perspective on loss of corneal stiffness. *Indian*

- journal of ophthalmology* **61**, 392-393, doi:10.4103/0301-4738.116057 (2013).
22. Sinha Roy, A., Kurian, M., Matalia, H. & Shetty, R. Air-puff associated quantification of non-linear biomechanical properties of the human cornea in vivo. *Journal of the mechanical behavior of biomedical materials* **48**, 173-182, doi:10.1016/j.jmbbm.2015.04.010 (2015).
23. Matalia, J. *et al.* Role of Age and Myopia in Simultaneous Assessment of Corneal and Extraocular Tissue Stiffness by Air-Puff Applanation. *Journal of refractive surgery* **32**, 486-493, doi:10.3928/1081597X-20160512-02 (2016).
24. Matalia, J. *et al.* Correlation of Corneal Biomechanical Stiffness With Refractive Error and Ocular Biometry in a Pediatric Population. *Cornea*, doi:10.1097/ICO.0000000000001290 (2017).
25. Pahuja, N. *et al.* Correlation of Clinical and Biomechanical Outcomes of Accelerated Crosslinking (9 mW/cm<sup>2</sup> in 10 minutes) in Keratoconus with Molecular Expression of Ectasia-Related Genes. *Current eye research* **41**, 1419-1423, doi:10.3109/02713683.2015.1133831 (2016).
26. Kotz, S. & Nadarajah, S. *Extreme value distributions : theory and applications*. (Imperial College Press, 2000).
27. Prescott, P. & Walden, A. T. Maximum likelihood estimation of the parameters of the generalized extreme-value distribution. *Biometrika* **67**, 723-724, doi:10.1093/biomet/67.3.723 (1980).





## Chapter 5

---

# In vivo prediction of air-puff induced corneal deformation using LASIK, SMILE, and PRK finite element simulations

Francis M, Khamar P, Shetty R, Sainani K, Nuijts RMMA, Haex B, Sinha Roy A

Invest Ophthalmol Vis Sci. 2018 Nov 1;59(13):5320-5328

**Purpose:** To simulate deformation amplitude (DA) after LASIK, SMILE and PRK with finite element models

**Methods:** Finite element simulations of air-puff applanation on LASIK, SMILE and PRK models were performed on a cohort of normal eyes, which had undergone refractive treatments.

Short and long-term wound healing responses were considered for SMILE and LASIK models based on evidence of micro-distortions in Bowman's layer and crimping of collagen fibers. First, inverse simulations were performed to derive the preoperative properties of the cornea. Using these properties and planned refractive treatment, postoperative air-puff deformation amplitude was predicted and compared with the *in vivo* measurements

**Results:** The predicted postoperative corneal stiffness parameters agreed very well with *in vivo* values in SMILE, LASIK and PRK eyes. Intra-class correlations (ICC) were greatest in PRK eyes (ICC > 0.95). This agreement was lower for peak deformation amplitude and peak deflection amplitude in SMILE and LASIK eyes (ICC < 0.9). In PRK eyes, peak deformation and deflection amplitude predictions were the best relative to *in vivo* magnitudes. Also, linear correlation ( $r$ ) between *in vivo* measurement and predicted biomechanical parameters indicated strong agreement between them (SMILE:  $r \geq 0.89$ , LASIK:  $r \geq 0.83$ , PRK:  $r \geq 0.87$ ).

**Conclusions:** This is the first study to present predictive simulations of corneal deformation changes after different procedures. Patient specific preoperative corneal biomechanical properties and finite element models were a significant determinant of accurate postoperative deformation amplitude prediction.

## Introduction

The anterior stroma of the cornea has an interweaving network of collagen fibers around the collagen lamellae.<sup>1</sup> This interweaving progressively becomes less through the depth of the stroma.<sup>1</sup> These structural features could be responsible for the greater tensile strength of the anterior stroma relative to the posterior stroma.<sup>2</sup> There are procedures that significantly alter the anterior stroma such as laser-assisted in situ keratomileusis (LASIK) and photorefractive keratectomy (PRK). In PRK, a portion of the anterior stroma is ablated in comparison to LASIK. Small incision lenticule extraction (SMILE) is another refractive procedure, which leaves much of the anterior stroma intact compared to LASIK and PRK. Using theoretical models, it was concluded that corneas undergoing SMILE could be biomechanically stronger compared to LASIK and PRK postoperatively.<sup>3,4</sup>

Air-puff applanation is the only clinical method available to assess corneal biomechanics. However, clinical studies on biomechanical changes in the cornea after these procedures were inconclusive.<sup>5-7</sup> Using dynamic air-puff applanation, two studies indicated a better biomechanical result after PRK than after LASIK.<sup>5,6</sup> Another study reported similar outcomes between PRK and LASIK.<sup>3</sup> However, a theoretical model predicted better biomechanical outcomes after SMILE and LASIK than after PRK.<sup>3</sup> Recent clinical data demonstrated

equivalence between SMILE and LASIK with respect to biomechanical changes in the cornea after surgery.<sup>8-10</sup> Further, Corvis-ST (OCULUS Optikgerate GmbH, Germany) was an improved device over the Ocular response analyzer (Reichert Inc., NY) since it had a highly repeatable pressure profile and quantified the mechanical deformation of the cornea. Theoretical models showed that LASIK caused a greater increase in mechanical stress in the residual stromal bed than SMILE.<sup>4</sup> Therefore, this study investigated simulated air-puff applanation on LASIK, PRK and SMILE finite element models, using the pressure profile generated by Corvis-ST (OCULUS Optikgerate GmbH, Germany).<sup>11</sup> In the finite element models, the transient air-puff was exported from Corvis-ST dynamic Scheimpflug analyzer and spatially distributed on the anterior surface using fluid dynamics analysis.<sup>11</sup>

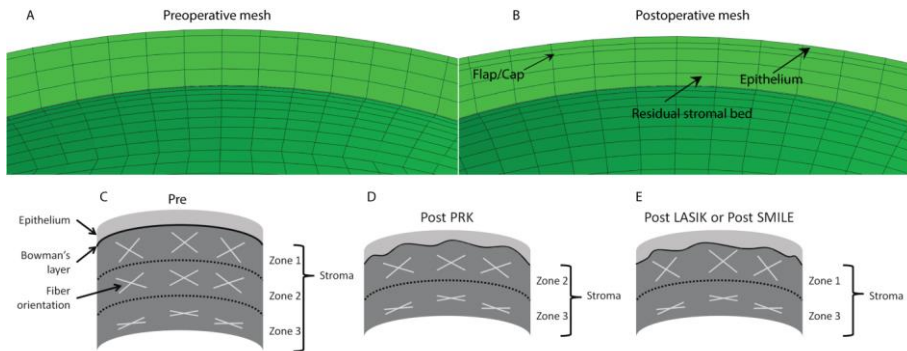


Figure 1: A cross-section of the finite element mesh: (A) preoperative and (B) postoperative. A schematic of pre-operative (C), post-PRK (D) and post-SMILE or LASIK (E) distribution of interweaving collagen fibers through the depth of the corneal stroma. For simplicity, zone 1

was considered as the flap and cap region of the central cornea in LASIK (E) and SMILE (E) models, respectively. Zone 2 was the zone of tissue removed (E) during simulated SMILE and LASIK. Zone 3 was the residual stromal bed. In PRK, zone 1 was the zone of tissue ablated leaving zones 2 and 3 as the residual stromal bed (D). These schematics show the differences in the fiber distributions through the depth of the stroma in the post-operative finite element models.

## Methods

This was a simulation study using finite element modeling. The method for the finite element model generation is briefly described here from another recent study.<sup>11</sup> 3-D geometry of a patient cornea was created from Pentacam (OCULUS Optikgerate GmbH, Wetzlar, Germany). The Pentacam provided Cartesian coordinates of the anterior and posterior corneal surface, which was used for creating a 3-D volume. Epithelium thickness of the cornea was measured with RTVue (Optovue Inc., USA). Finite element mesh was created with 8-noded linear hexahedral elements (TruGrid, XYZ Scientific Applications, Inc., Livermore, USA). A total of 3312 hexahedral elements were used to represent the corneal volume. Figures 1A and B show a cross-section of the pre and postoperative mesh (with flap/cap) of the central cornea, respectively. PRK finite element mesh did not have any flap/cap zone. An anisotropic, hyperelastic, fiber dependent material model with material incompressibility was chosen.<sup>1</sup> The material model accounted

for both the orthogonal arrangement of fibers in the central cornea, depth dependency of angular direction of the interweaving fibers and re-orientation of the *in plane* peripheral collagen fibers to circumferential direction.<sup>11</sup> The hyperelastic material model was represented by free energy density ( $\psi$ ):

$$\psi(\mathbf{C}) = \psi_m(\bar{\mathbf{I}}_1, \mathbf{I}_3) + \psi_{f\text{-plane}}(\mathbf{C}) + \psi_{f\text{-cross}}(\mathbf{C}) \quad (1)$$

where  $\mathbf{I}_1 = \mathbf{C} : \mathbf{1}$  and  $\mathbf{I}_3 = \det[\mathbf{C}]$  were the 1<sup>st</sup> and 3<sup>rd</sup> invariants of the deformation tensor.  $\mathbf{C}$  was the right Cauchy-Green deformation tensor and  $\det[\mathbf{C}]$  represented determinant of the tensor. The isotropic energy density of the matrix ( $\psi_m$ ) was described by:

$$\psi_m(\bar{\mathbf{I}}_1, \mathbf{I}_3) = \mathbf{C}_1(\bar{\mathbf{I}}_1 - 3) + \mathbf{C}_2(\bar{\mathbf{I}}_1 - 3)^2 + \frac{(\mathbf{I}_3 - 1)^2}{\mathbf{D}_1} \quad (2)$$

where  $\bar{\mathbf{I}}_1 = \mathbf{I}_3^{-1/3} \mathbf{I}_1$  was the distortional part of  $\mathbf{I}_1$ ,  $\mathbf{I}_3$  was the determinant of deformation gradient tensor and  $\mathbf{C}_i$ 's were the material constants.  $\mathbf{D}_1$  was the bulk modulus to enforce incompressibility and was assumed to be  $10^{-6}$ . The fiber energy density ( $\psi_{f\text{-plane}}$ ) was described by:

$$\psi_{f\text{-plane}}(\mathbf{C}) = \int_{-\pi}^{\pi} \mathbf{W}_f(\lambda_{f\text{-plane}}) \mathbf{D}_{\text{plane}}(\theta) d\theta \quad (3)$$

$$\mathbf{W}_{f\text{-plane}}(\lambda_{f\text{-plane}}) = \frac{\mathbf{k}_1}{2\mathbf{k}_2} \exp(\mathbf{k}_2 [\lambda_{f\text{-plane}} - 1]^2) - \frac{\mathbf{k}_1}{2\mathbf{k}_2} \quad (4)$$

$\psi_{f\text{-plane}}$  represented the energy density of in-plane lamellar collagen fibers with stretch,  $\lambda_{f\text{-plane}}$  equal to  $\sqrt{\mathbf{A} \cdot \mathbf{C} \mathbf{A}}$ , where  $\mathbf{A} = [\cos\theta, \sin\theta, 0]^T$  was the local direction vector of the fibers.  $\mathbf{k}_1$  and  $\mathbf{k}_2$  were the material

constants.  $D_{\text{plane}}(\theta)$  represented a weighted average of the energy density of the fiber families at each integration point of the element. It also represented the change in the preferred direction of the fibers from orthogonal in the central cornea to circumferential near the limbus.

$$\Psi_{\text{f-cross}}(C) = \int_{-\pi}^{\pi} W_{\text{f}}(\lambda_{\text{f-cross}}) D_{\text{cross}}(\theta) d\theta \quad (5)$$

$$W_{\text{f-cross}}(\lambda_{\text{f-cross}}) = \frac{k_1}{2k_2} \exp(k_2 [\lambda_{\text{f-cross}} - 1]^2) - \frac{k_1}{2k_2} \quad (6)$$

$\psi_{\text{f-cross}}$  represented the energy density of crosslink fibers between the lamellae with stretch,  $\lambda_{\text{f-cross}}$  equal to  $\sqrt{B \cdot CB}$ , where B was the direction vector of the crosslink fibers. B was determined by taking a cross-product of A with the surface normal and then rotating it out-of-plane around A by an angle  $\xi$ . The angle  $\xi$  was assumed to be a function of depth and was modeled as follows<sup>11</sup>:

$$\xi = 28.6^\circ \frac{\exp(3.19[1-s]) - 1}{\exp(3.19) - 1} \quad (7)$$

s was the non-dimensional local thickness. The angle  $\xi$  was evaluated at each element centroid.  $D_{\text{plane}}(\theta)$  was kept equal to  $D_{\text{cross}}(\theta)$ . From the above equations, the Cauchy stress was determined by:

$$\sigma = \frac{1}{\sqrt{I_3}} F \frac{\partial \Psi}{\partial C} F^T \quad (8)$$



where  $F$  was the deformation gradient tensor. The epithelium was modeled as an isotropic, hyperelastic, incompressible material [ $\psi(C) = \psi_m(I_1, I_3)$  only] with  $c_1 = 5$  kPa and  $c_2 = 0.0$  kPa

To derive the *in vivo* anisotropic material properties of the cornea, deformation amplitude measurement (from Corvis-ST) of the patient was coupled with an inverse finite element model.<sup>11</sup> The inverse finite element model derived the *in situ* corneal ( $C_1$ ,  $C_2$ ,  $k_1$  and  $k_2$ ) and extra-corneal [ $K_z$  (N/m),  $\mu$  (Pa.sec) and  $m$  (gm)] material properties. The inverse model minimized the difference between the measured displacements of the anterior edge of the cornea and calculated displacements of the same edge from the finite element simulations. The inverse model was designed such that the corneal and extra-corneal properties were governed by the corneal deformation (reported as deflection amplitude by Corvis-ST) and whole-eye movement, respectively.<sup>11</sup> Here, deformation amplitude was the arithmetic sum of corneal deformation and whole-eye movement.<sup>11</sup> An iterative method (Levenberg–Marquardt algorithm) for minimization was adopted. The finite element simulations were performed in ABAQUS (Dassault Systèmes Americas Corporation, Waltham, USA). The material model was incorporated in the simulations using ABAQUS material subroutine (UMAT). The inverse calculations were performed using a custom script written in Python (v2.7.3). ABAQUS simulations and Python scripts were executed simultaneously in a multi-threaded Intel Xeon workstation.

To simulate a myopic spherical power correction, the anterior surface of the corneal geometry was recomputed using an aspheric ablation profile.<sup>12</sup> Figure 1C shows a schematic of a cross-section of the cornea (epithelium and stroma). The figure shows the epithelium, flap in LASIK (or cap in SMILE), peripheral cornea outside the flap/cap and the residual stromal bed. For simplicity, the stroma was further subdivided into 3 zones in the axial direction for better visualization of the angular orientation of the interweaving fibers. As shown in Figure 1C, the angular direction of the interweaving fibers decreased through the depth of the stroma, i.e., zone 1 (anterior stroma) was the stiffest followed by zones 2 and 3.<sup>1</sup> Different surgical procedures were simulated as follows:

- a) PRK – In PRK, a significant portion of the anterior stroma was removed from the corneal 3-D geometry, which dependent on the magnitude of myopic correction. This can be visualized in Figure 1D, where zone 1 of the stroma was removed to simulate the refractive change. Thus, the corneal geometry had residual interweaving collagen fibers with angular orientation of zones 2 and 3 with reference to preoperative structure (Figure 1C). Also, it was assumed that epithelium remodeling was complete after the simulated surgery. It was also assumed that the pre and postoperative epithelium thicknesses were the same. The optical diameter of the ablation profile and the treatment zone was 6 and 9 mm, respectively.<sup>12</sup>

b) SMILE – Figure 1E shows a schematic of a cross-section of the cornea with simulated SMILE. The anterior surface of the cornea geometry was altered with aspheric ablation profile. For simplicity, let's assume that zone 1 was the cap and zone 2 was the region of the stroma corresponding to the SMILE lenticule. Thus, zone 2 would be absent after simulated SMILE. The corneal geometry would retain only zones 1 and 3 with corresponding angular directions of the interweaving fiber as shown in Figure 1C. Here, zone 3 was the residual stroma bed (RSB). In the simulated finite element model, the cap and RSB were modeled explicitly. Further, a discontinuity in the transition of the angular direction of interweaving fibers was modeled between the cap and RSB (as shown schematically in Figure 1B) in the ABAQUS user subroutine. The simulated optical and cap diameter was 6 mm and 7.8 mm, respectively.

To model the postoperative mechanics of the cap, a short and long-term wound healing response was hypothesized. While wound healing is a broad topic involving changes in hydration and keratocytes among other physiological components, we evaluated the recruitment of the collagen fibers to bear mechanical stress only in this study as wound healing response. Increased micro-distortions were detected in the Bowman's layer after SMILE, which didn't resolve even up to 3 months after the surgery.<sup>13</sup> This increase in micro-distortions could be indicative of compression of the cap due to mechanical

extraction of the lenticule and mismatch between the lenticular surfaces.<sup>13</sup> This directly implied that the collagen fibers in the cap were probably under reduced tensile stress and underwent some crimping<sup>14</sup> since the micro-distortions were greater than the preoperative state even 3 months after SMILE (Figure 2). Therefore, the cap was assumed to have only isotropic material properties ( $C_1$  and  $C_2$  were the same as pre-operative,  $k_1$  and  $k_2$  were set to zero) in the finite element model assuming short-term wound healing. In the long-term finite element model, the cap material properties were set the same as pre-operative anisotropic, hyperelastic properties with the assumption that incision in the anterior stroma did not cause a significant decrease in the cap's strength. Further, the postoperative material properties and fiber distributions of the peripheral cornea outside the cap zone were assumed to be the same as preoperative state.

- c) LASIK – The difference between SMILE and LASIK is the presence of the flap instead of a cap. The flap has an arc span of nearly 360 degrees. By extrapolating the effect of crimping of collagen fibers in the cap, it was logical to assume that the flap also should undergo a similar change, i.e., the collagen fibers were under reduced tension (Figure 2). In the finite element model, the angular orientation of the interweaving fibers in the LASIK model would be similar to the SMILE model (Figure 1C). However, the short and long-term finite element model of

LASIK assumed only isotropic material properties for the flap since the LASIK flap cut severed a significantly greater number of collagen fibers in the anterior stroma and it was unlikely that these severed fibers re-attach to the residual stromal bed. The simulated optical and cap diameter was 6 mm and 9.0 mm, respectively. The epithelium thickness in the LASIK model was assumed to be the same as pre-operative state. The postoperative material properties (including the fiber distributions) of peripheral cornea outside the flap zone and in the residual stromal bed were assumed to be the same as preoperative state.

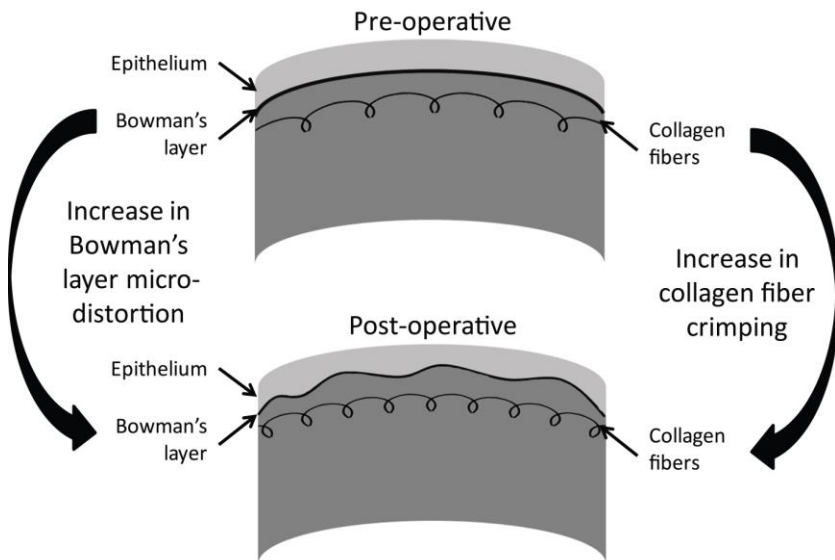


Figure 2: A model to describe pre and post-operative structure of Bowman's layer and collagen fiber in stroma. Due to surgery, micro-distortions in the Bowman's layer increase due to compression of the

cap/flap. This may result in crimping of the collagen fibers, i.e., fibers are not in tension and don't bear the stress due to intraocular pressure.

Table 1: Mean (95% confidence interval) of preoperative demographics of the cohorts.

	SMILE (n=12)	LASIK (n=12)	PRK (n=12)	p- value
<i>In vivo</i> preoperative CCT ( $\mu\text{m}$ )	504 [481.3 to 526.7]	511.9 [489.7 to 534.2]	515 [497 to 533]	0.90
<i>In vivo</i> postoperative CCT ( $\mu\text{m}$ )	452.8 [439.3 to 466.3]	460.8 [438.6 to 483]	459.3 [426 to 492.5]	0.87
Predicted CCT ( $\mu\text{m}$ )	457.4 [444.8 to 469.9]	464.8 [443.3 to 486.3]	465.5 [431.6 to 499.5]	0.85
Intraocular pressure (mmHg)	16.25 [15.55 to 16.95]	16.17 [15.41 to 16.93]	17.2 [15.83 to 18.51]	0.80
Manifest refraction spherical equivalent (D)	-4.75 [-5.66 to -3.84]	-4.67 [-5.58 to -3.75]	-4.27 [- 5.44 to - 3.1]	0.84

SMILE = small incision lenticule extraction, LASIK = laser-assisted in situ keratomileusis, PRK = photorefractive keratectomy, CCT = central corneal thickness

In vivo prediction of air-puff induced corneal deformation

Table 2: *In vivo* (pre and postoperative) and predicted (only postoperative) values of corneal stiffness, peak deformation and peak deflection amplitude for SMILE, LASIK and PRK eyes (n= 12 eyes per surgery). Values are reported as mean and 95% confidence interval of the mean.

Parameter	<i>In vivo</i> preoperative measurement	<i>In vivo</i> postoperative measurement*
<b>SMILE</b>		
Kc (mean) (N/m)	101.35 [92.83 to 109.86]	86.13 [80.98 to 91.28]
Kc (Constant) (N/m)	104.01 [97.72 to 110.3]	92.79 [88.63 to 96.95]
Peak deformation amplitude (mm)	1.15 [1.09 to 1.21]	1.23 [1.16 to 1.3]
Peak deflection amplitude (mm)	1.02 [0.96 to 1.07]	1.08 [1.03 to 1.14]
<b>LASIK</b>		
Kc (mean) (N/m)	101.05 [95.11 to 106.99]	91.32 [84.52 to 98.13]
Kc (Constant) (N/m)	104.9 [98.85 to 110.96]	96.01 [88.18 to 103.85]
Peak deformation amplitude (mm)	1.13 [1.07 to 1.19]	1.21 [1.12 to 1.31]
Peak deflection amplitude (mm)	1.03 [0.96 to 1.1]	1.08 [1.02 to 1.15]
<b>PRK</b>		
Kc (mean) (N/m)	96.78 [85.64 to 107.92]	90.43 [77.58 to 103.29]
Kc (Constant) (N/m)	101.28 [93.5 to 109.07]	96.24 [87.25 to 105.22]
Peak deformation amplitude (mm)	1.17 [1.05 to 1.29]	1.23 [1.12 to 1.33]
Peak deflection amplitude (mm)	1.02 [0.93 to 1.12]	1.07 [0.97 to 1.17]

Table 2: continued

Predicted postoperative value*	Intra-class correlation*	RMSE of prediction
<b>SMILE</b>		
87.9 [81.95 to 93.85]	0.95	3.53
90.26 [86.52 to 94]	0.93	3.15
1.29 [1.24 to 1.34]	0.81	0.08
1.16 [1.11 to 1.21]	0.72	0.09
<b>LASIK</b>		
91.56 [85.29 to 97.83]	0.95	3.55
93.83 [87.63 to 100.04]	0.96	3.37
1.26 [1.18 to 1.34]	0.91	0.07
1.18 [1.08 to 1.27]	0.73	0.11
<b>PRK</b>		
87.27 [73.86 to 100.69]	0.99	3.49
91.77 [81.77 to 101.77]	0.96	4.84
1.28 [1.15 to 1.41]	0.91	0.09
1.17 [1.03 to 1.3]	0.89	0.12

Kc = corneal stiffness, SMILE = small incision lenticule extraction, LASIK = laser-assisted in situ keratomileusis, PRK = photorefractive keratectomy, ICC = intraclass correlation coefficient, RMSE = root mean square error.



Table 3: Regression result between *in vivo* postoperative measurement (y) and predicted (x) postoperative value for corneal stiffness, peak deformation and peak deflection amplitude for surgical cohorts (SMILE, LASIK and PRK) and all eyes together. All the regression results tabulated below had p-value < 0.001.

	Parameter	Regression equation	r
SMILE (n=12)	Kc (mean) (N/m)	$y = 15.05 + 0.81 x$	0.93
	Kc (Constant) (N/m)	$y = -2.62 + 1.06 x$	0.95
	Peak deformation amplitude (mm)	$y = -0.34 + 1.21 x$	0.89
	Peak deflection amplitude (mm)	$y = -0.08 + 1.0 x$	0.89
LASIK (n=12)	Kc (mean) (N/m)	$y = 1.74 + 0.98 x$	0.90
	Kc (Constant) (N/m)	$y = -3.08 + 1.05 x$	0.93
	Peak deformation amplitude (mm)	$y = -0.05 + 1.0 x$	0.89
	Peak deflection amplitude (mm)	$y = 0.42 + 0.57 x$	0.83
PRK (n=12)	Kc (mean) (N/m)	$y = 7.92 + 0.95 x$	0.99
	Kc (Constant) (N/m)	$y = 16.93 + 0.86 x$	0.96
	Peak deformation amplitude (mm)	$y = 0.31 + 0.72 x$	0.89
	Peak deflection amplitude (mm)	$y = 0.24 + 0.71 x$	0.93
All eyes (n=36)	Kc (mean) (N/m)	$y = 7.03 + 0.93 x$	0.95
	Kc (Constant) (N/m)	$y = 11.11 + 0.91 x$	0.94
	Peak deformation amplitude (mm)	$y = 0.19 + 0.81 x$	0.87
	Peak deflection amplitude (mm)	$y = 0.26 + 0.70 x$	0.90

$K_c$  = corneal stiffness, SMILE = small incision lenticule extraction, LASIK = laser-assisted in situ keratomileusis, PRK = photorefractive keratectomy

Postoperatively, the peripheral lamellae, adjacent to the flap/cap, were assumed to be in continuum with the lamellae of the residual stromal bed similar to the preoperative state. Further, simulated flap/cap thicknesses included the epithelium thicknesses in it.

The validation of the surgical finite element simulations on the model eye was conducted in two phases. In the first phase, the model results were compared with clinical outcomes of cohort of eyes, which underwent LASIK, SMILE and PRK. The prediction of  $K_c$  (constant),  $K_c$  (mean), peak deformation amplitude and peak deflection amplitude were performed for the cohort of eyes. The corneal stiffnesses,  $K_c$  (constant) and  $K_c$  (mean), were calculated from the deformation amplitude using an analytical approach.<sup>15, 16</sup> First, the preoperative material properties of each eye were determined with the inverse finite element method described earlier. The programmed refractive error (sphere and cylindrical error) was simulated in the finite element mesh with aspheric profile. Then, postoperative deformation amplitude of each eye was simulated with its' respective surgical model, i.e., LASIK, PRK and SMILE. The peak deformation amplitude and  $K_c$  (constant) was determined from the computed postoperative deformation amplitude. The "short-term wound healing" assumption was applied to

the postoperative finite element simulations. These were compared with the same derived from *in vivo* measurement of postoperative deformation amplitude. In the second phase, a case example of one eye from each group with similar preoperative IOP and CCT was chosen. In other words, validation was conducted both for a cohort of eyes and a set of individual eyes. For the cohort of eyes, root mean square error (RMSE) was calculated for each parameter within a group, e.g., RMSE of Kc (constant) for SMILE eyes was square root of sum of squares of difference between *in vivo* and predicted magnitude of Kc (constant) divided by total number of eyes that underwent SMILE.

This was a retrospective analysis of data. The study was approved by ethics committee of the Narayana Nethralaya Eye Hospital, Bangalore, India. All the surgeries were performed by a single experienced surgeon under topical anesthesia using 0.5% proparacaine hydrochloride (Paracain, Sunways Pvt. Ltd., Mumbai, India) instilled 2–3 times. LASIK was performed with the WaveLight FS200 femtosecond laser and WaveLight EX500 excimer laser platform (Alcon Laboratories, Ft Worth, USA). A flap (9.0 mm diameter, 110  $\mu$ m thickness, a side cut angle of 70°, canal width of 1.5 mm and hinge position at 90°) was created. After the flap was created, the same was manually lifted and excimer ablation of targeted refraction was performed. SMILE was performed with the VisuMax femtosecond laser system (Carl Zeiss Meditec AG, Germany). Cap thickness was 110  $\mu$ m. Lenticule and cap diameter was 6.0 mm and 7.8 mm, respectively. These

flap and gap geometrical details were incorporated in the 3-D finite element model. After creation of the refractive lenticule, it was dissected and extracted manually through a superior 3 mm side-cut. Cornea was remoistened with a wet merocel sponge at the end of the procedure. After the surgery, one drop of moxifloxacin hydro-chloride 0.5% (Vigamox®, Alcon Laboratories, Inc., Fort Worth, TX, USA) was applied to both eyes.

All PRK procedures were done under 0.5% proparacaine hydrochloride under strict aseptic conditions. The epithelium was manually scraped in the central 8 mm diameter zone before ablation. Wavefront optimized PRK was performed with WaveLight Allegretto EX-500 laser (Alcon) using a 6 mm diameter optical zone. A bandage contact lens (Ciba Vision, Duluth, USA) was applied after the surgery. Routine postoperative regimen was followed for all eyes. This included moxifloxacin hydrochloride 0.5% eye drops (Vigamox®, Alcon) four times a day for 1 week, tapering doses of topical 1% Fluorometholone eye drops (Flarex®, Alcon) and topical lubricants (Optive®, Allergan Inc., Irvine, USA) four times a day for three months. All eyes underwent Corvis-ST measurement before and 3 months after surgery. The pre and post-operative deformation amplitude of each eye was analyzed to determine peak deformation amplitude and with the analytical model to determine  $K_c$  (constant). These were compared with the results of simulations on the model eye. Mean deformation amplitude of each cohort of eyes was compared between pre and postoperative time points.

Deformation amplitude was chosen as the primary comparator since it allowed easy visual comparison between *in vivo* and simulation results.

## Results

Table 1 shows the preoperative demographics of the 3 cohorts of eyes. A comparison of the *in vivo* postoperative and simulated central corneal thickness in the postoperative finite element geometry is also shown in Table 1. All groups were statistically similar preoperatively ( $p > 0.05$ ). Table 2 shows the *in vivo* pre and postoperative Kc (mean), Kc (constant), peak deformation amplitude and peak deflection amplitude. The predicted magnitudes of the above variables are also shown in Table 2. There was excellent agreement between measured and predicted magnitudes of Kc (mean) and Kc (constant) since intra-class correlation (ICC) was greater than 0.9 for all procedures. Overall, prediction of peak deformation amplitude and deflection amplitude was best in PRK eyes (ICC ~ 0.9), which could be due to absence of flap or cap in PRK. However, the difference between *in vivo* preoperative and *in vivo* postoperative peak deformation and deflection amplitude were similar between all the eye groups (Table 2). RMSE of Kc (mean) and Kc (constant) were significantly greater than the difference between the mean values of *in vivo* and predicted postoperative magnitudes (Table 2). This explained the high ICC for Kc (mean) and Kc (constant) for SMILE, LASIK and PRK eyes. Interestingly, RMSE of peak deformation and deflection amplitude were within repeatability of these

parameters.<sup>17, 18</sup> Further, PRK eyes had the least decrease in magnitude of  $K_c$  (mean) and  $K_c$  (constant) after surgery, e.g., *in vivo* mean  $K_c$  (mean) and mean  $K_c$  (constant) decreased by 6.35 and 5.04 N/m only (Table 2). In contrast, LASIK and SMILE caused a greater decrease in stiffnesses (Table 2).

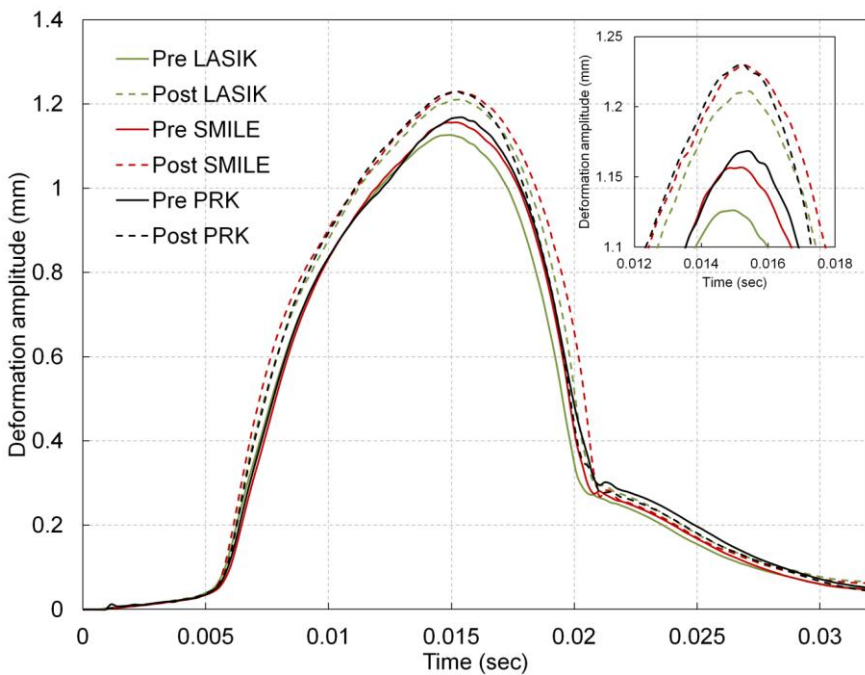


Figure 3: Mean deformation amplitude of a cohort of eyes, which underwent LASIK, SMILE and PRK. Solid and dotted lines indicate mean preoperative and postoperative measurement, respectively. The measurement near the peak deformation amplitude is magnified in the inset box.

## In vivo prediction of air-puff induced corneal deformation

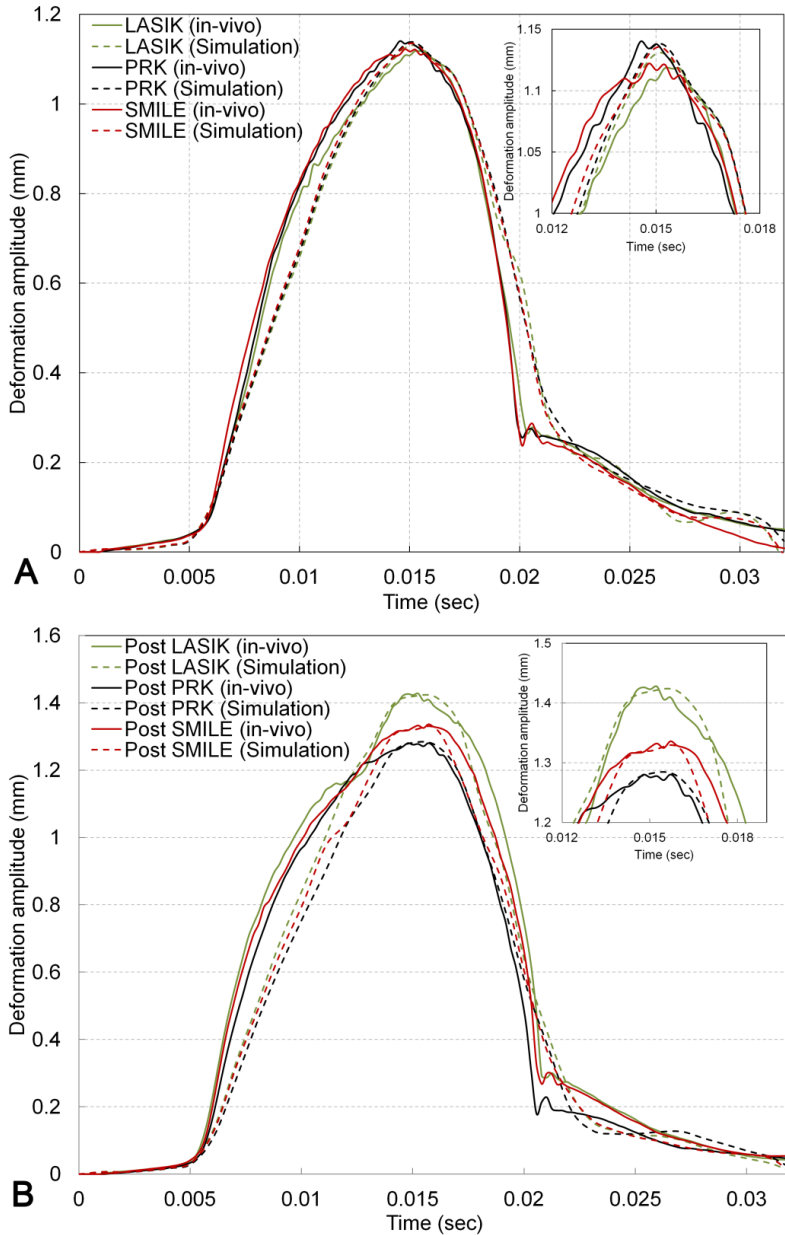


Figure 4: (A) Mean preoperative deformation amplitude of an individual eye from each cohort (Figure 3). Dotted line shows the computed result

of the inverse finite element method. (B) Mean pre and postoperative deformation amplitude for the same eyes. For the preoperative time points, dotted lines show the estimate of the inverse finite element method (same as Figure 4A). For the postoperative time points, dotted lines show the calculated deformation amplitude using the preoperative material properties and finite element simulations of the surgeries.

Overall, PRK eyes had the best agreement (ICC ~ 0.9 and above) between *in vivo* postoperative measurement and predicted postoperative value (Table 2). Figure 3 shows an overlay of the mean deformation amplitude of the eyes before and after surgery from LASIK, SMILE and PRK cohorts. These waveforms were derived by averaging the *in vivo* deformation amplitude waveforms of all the eyes at respective time points for a given treatment (LASIK, SMILE or PRK). Linear regression analyses (Table 3) were performed between the *in vivo* and predicted postoperative variables for all the 36 eyes (taken together) and separate cohorts. From Table 3, the correlation coefficients ( $r$ ) were 0.95, 0.94, 0.87 and 0.90 for  $K_c$  (mean),  $K_c$  (constant), peak deformation amplitude and peak deflection amplitude, respectively, for all eyes ( $n=36$ ). The slopes of the linear regressions were 0.93, 0.91, 0.81 and 0.70, respectively ( $p<0.001$  for all).

As a case example, one eye was chosen from each cohort (discussed above) to demonstrate the predictive ability of the surgical finite element simulations. The preoperative thickness of the LASIK,



SMILE and PRK eye was 515, 500 and 504  $\mu\text{m}$ , respectively. The preoperative IOP of the LASIK, SMILE and PRK eye was 16, 15 and 18.8 mmHg, respectively. The preoperative manifest refraction spherical equivalent of the LASIK, SMILE and PRK eye was -6.13, -6.63 and -7.25 D, respectively. Figure 4A shows the preoperative deformation amplitude of each eye reported by Corvis-ST. The dotted line represented the deformation estimated by the inverse finite element method. The optimized material properties are listed below:

- LASIK eye:  $C_1=80.13$  kPa,  $C_2=2.52$  MPa,  $k_1=25.1$  kPa,  $k_2 = 430.9$ ,  $K_z = 1267$  N/m,  $\mu = 4.61$  Pa.sec and  $m = 0.03$  gm.
- SMILE eye:  $C_1=82.75$  kPa,  $C_2=1.98$  MPa,  $k_1=55.3$  kPa,  $k_2 = 637.1$ ,  $K_z = 1775$  N/m,  $\mu = 3.07$  Pa.sec and  $m = 0.05$  gm.
- PRK eye:  $C_1=68.4$  kPa,  $C_2=2.62$  MPa,  $k_1=41.9$  kPa,  $k_2 = 706.4$ ,  $K_z = 1379$  N/m,  $\mu = 3.72$  Pa.sec and  $m = 0.04$  gm.

Preoperatively, peak deformation amplitude was 1.12 mm in the LASIK and SMILE eyes. In the PRK eye, it was 1.14 mm. In the LASIK eye, postoperative measured and calculated (finite element simulations) peak deformation amplitude were 1.42 and 1.42 mm, respectively. The same was 1.30 and 1.32 mm, respectively, in the SMILE eye. In the PRK eye, the same were 1.28 and 1.28 mm, respectively. Preoperatively,  $K_c$  (constant) was 105.3, 104.5 and 101.7 N/m, respectively. In the LASIK eye, postoperative measured (*in vivo*

deformation amplitude analyzed with the analytical method) and calculated (finite element simulations)  $K_c$  (constant) were 85.4 and 79.5 N/m, respectively. In the SMILE eye, the same were 95.4 and 90.5 N/m, respectively. In the PRK eye, the same were 96.5 and 93.1 N/m, respectively. Thus, the postoperative finite element simulations estimated the peak deformation amplitude better than  $K_c$  (constant). Figure 4B shows an overlay of pre and postoperative [both measured by Corvis-ST (solid lines) and prediction by surgical finite element models (dotted lines)] deformation amplitude.

## Discussion

These are exciting times for the field of refractive surgery since a diverse array of procedures are available to treat refractive error in patients. Biomechanics of the cornea is one of the key drivers of improved techniques.<sup>2-4</sup> SMILE leaves most of the anterior stroma intact, which incidentally is the stiffest region of the stroma. Thus, SMILE caused the least biomechanical changes in the cornea in theoretical models.<sup>3, 4</sup> However, clinical evaluation of biomechanical changes cannot be performed in terms of the mechanical stresses and displacements<sup>19</sup> as these parameters cannot be measured in patients yet. Air-puff applanation is the only available technique to clinically evaluate these procedures. Therefore, this study focused exclusively on expected deformation response of the cornea after simulated LASIK,

PRK and SMILE coupled with air-puff applanation. The following were the key outcomes from this study:

- When a cohort of eyes was measured with Corvis-ST before and after surgery, PRK eyes had the least decrease in stiffness parameters. Also, LASIK and SMILE caused a much greater decrease in stiffness parameters (Table 2). However, the change in *in vivo* peak deformation and deflection amplitude was similar between the cohorts (Table 2). This highlighted the need for patient specific prediction of deformation amplitude using patient specific finite element models since theoretical models, devoid of patient specific material properties, predicted SMILE to cause the least change in corneal stiffness.<sup>3,4</sup>
- PRK eyes had the best agreement between *in vivo* and predicted postoperative value of stiffness, peak deformation amplitude and peak deflection amplitude. SMILE and LASIK eyes also had excellent agreement for stiffness parameters (Table 2). Flap or cap could have reduced the level of agreement between *in vivo* and predicted postoperative value of peak deformation amplitude and peak deflection amplitude in LASIK and SMILE eyes.
- Figures 4A and B showed the accuracy of determination of deformation amplitude using the finite element simulations and assumptions of wound healing (crimping of collagen fibers) in

one eye from each cohort (SMILE, LASIK and PRK). Such modeling tools could be integrated with Corvis-ST in future versions of the device.

The study also introduced two variants of remodeling in the flap and cap, which were attributed to short and long-term response. These variants were derived from recent observations of patient corneas after surgery.<sup>13</sup> The results showed that air-puff deformation response of the cornea were highly dependent on the preoperative material properties of the cornea with the assumption of short-term wound healing response. Further for the same treatment, a thicker flap or cap and theoretical models predicted slightly greater stiffness post-operatively.<sup>3, 4</sup> Clinical results of comparative studies between LASIK and PRK with the Corvis-ST generally indicate a stiffer biomechanical response after PRK than predicted by the model.<sup>5-7</sup> This indicated the importance of greater degree of fibrotic scars and haze formation in PRK than in LASIK,<sup>20, 21</sup> which could have resulted in some biomechanical compensation to removal of the stiffest region of the stroma. Clinical results of comparative studies between LASIK and SMILE using the Corvis-ST indicated similar biomechanical changes.<sup>8-10</sup> This study provided an explanation to these observations and demonstrated the limitation in using device deformation variables such as peak deformation amplitude to compare SMILE and LASIK. Our inverse simulation method of comparing post-operative outcomes may yield better segregation of biomechanical responses after SMILE and LASIK. Future inverse

models could benefit with a continuum mechanics approach to simulate the biological stiffening effect after PRK, though this would be a challenging task.

An assumption made in this study was the temporal healing response. A significantly lesser number of collagen lamellae were cut in SMILE compared to LASIK. In a recent study, Bowman's layer distortions returned to preoperative magnitudes in the SMILE eyes within 6 months after surgery.<sup>22</sup> However, the distortions were greater than preoperative magnitudes in the LASIK eyes after surgery.<sup>22</sup> This led us to conclude that crimping in the collagen may not have returned to preoperative levels in the LASIK eyes even after longer healing time. Further long-term follow-up would be required to confirm this trend but the six month results lend credence to our modeling assumptions. Another limitation of the study was that the effect of hydration on the elastic strength of the cornea was not evaluated. The deformation amplitude was a dynamic but fast measurement. The deformation amplitude is primarily determined by elastic properties of the cornea.<sup>11, 15, 16, 23</sup> However, the net stress in the fiber would be a vector summation of the stress due to IOP and fluid pressure. If hydration was significantly altered after surgery, then postoperative deformation amplitude could differ significantly from the model predictions, i.e. ICC could be lower than 0.9 for all variables.

Another limitation was that a reduced eye model was implemented since patient specific geometrical data on globe, muscles and fat weren't available in routine clinic. A reduced eye model is also warranted from the perspective of reducing the computational cost without significantly effecting the reliability of the predictions.<sup>11</sup> Further, postoperative epithelium thickness is no longer as uniform as preoperative thickness and this introduced an approximation to the true thickness of the postoperative stroma. Most current OCT devices limit epithelium thickness reports to the central 6 mm cornea only. Thus, the data was insufficient for inclusion in patient specific simulations, where the corneal diameter was significantly greater. These limitations could also explain the difference between postoperative corneal stiffnesses derived from *in vivo* deformation amplitude and the same estimated from simulation results.

Further study with inverse finite element modeling and post-operative measurements on patient corneas can help understand this effect. In a previous study, it was shown that the magnitude and distribution of the mechanical stresses in the cap and residual stromal bed of the SMILE model were similar to the pre-operative equivalent thickness state.<sup>4</sup> The same wasn't observed in the LASIK model.<sup>4</sup> Thus, SMILE left the residual cornea biomechanically stiffer than LASIK.<sup>4</sup> However, the relation between stress and peak deformation amplitude wasn't linear, e.g., a 10% increase in the stress in the residual stromal bed cannot be considered as a 10% increase in peak deformation

amplitude. The results from this study show that the alteration in stresses in the post-operative models resulted in minor changes in simulated deformation amplitude. This was in agreement with recent clinical studies comparing biomechanics of SMILE and LASIK with Corvis-ST.<sup>8-10</sup> To conclude, this is the first simulation study to show the predicted deformation amplitude after simulated LASIK, SMILE and PRK, using novel structural perturbations that may be representative of *in vivo* state of the cornea after surgery. Future studies need to investigate alternate analyses techniques or newer measurement techniques to quantify the viscous contribution to *in vivo* tissue stiffness.

### **Acknowledgements**

This study was funded by in part by the SIBAC research grant from the Indo-German Science and Technology Center, Government of India and by Car Zeiss Meditec, Germany.

### **Author Contributions**

**Francis M:** Data acquisition, analysis and interpretation of data, and drafting manuscript.

**Khamar P:** Data acquisition, analysis and interpretation of data, and drafting manuscript.

**Shetty R:** Concept and design, data acquisition, analysis and interpretation of data, drafting manuscript, critical revision of manuscript, and final approval.

**Sainani K:** Data acquisition, analysis and interpretation of data, and drafting manuscript.

**Nuijts RMMA:** Concept and design, critical revision of manuscript, and final approval.

**Sinha Roy A:** Concept and design, critical revision of manuscript, securing funding and final approval.

## References

1. Winkler M, Shoa G, Xie Y, et al. Three-dimensional distribution of transverse collagen fibers in the anterior human corneal stroma. *Invest Ophthalmol Vis Sci* 2013;54:7293-7301.
2. Randleman JB, Dawson DG, Grossniklaus HE, McCarey BE, Edelhauser HF. Depth-dependent cohesive tensile strength in human donor corneas: implications for refractive surgery. *J Refract Surg* 2008;24:S85-89.
3. Reinstein DZ, Archer TJ, Randleman JB. Mathematical model to compare the relative tensile strength of the cornea after PRK, LASIK, and small incision lenticule extraction. *J Refract Surg* 2013;29:454-460.
4. Sinha Roy A, Dupps WJ, Jr., Roberts CJ. Comparison of biomechanical effects of small-incision lenticule extraction and



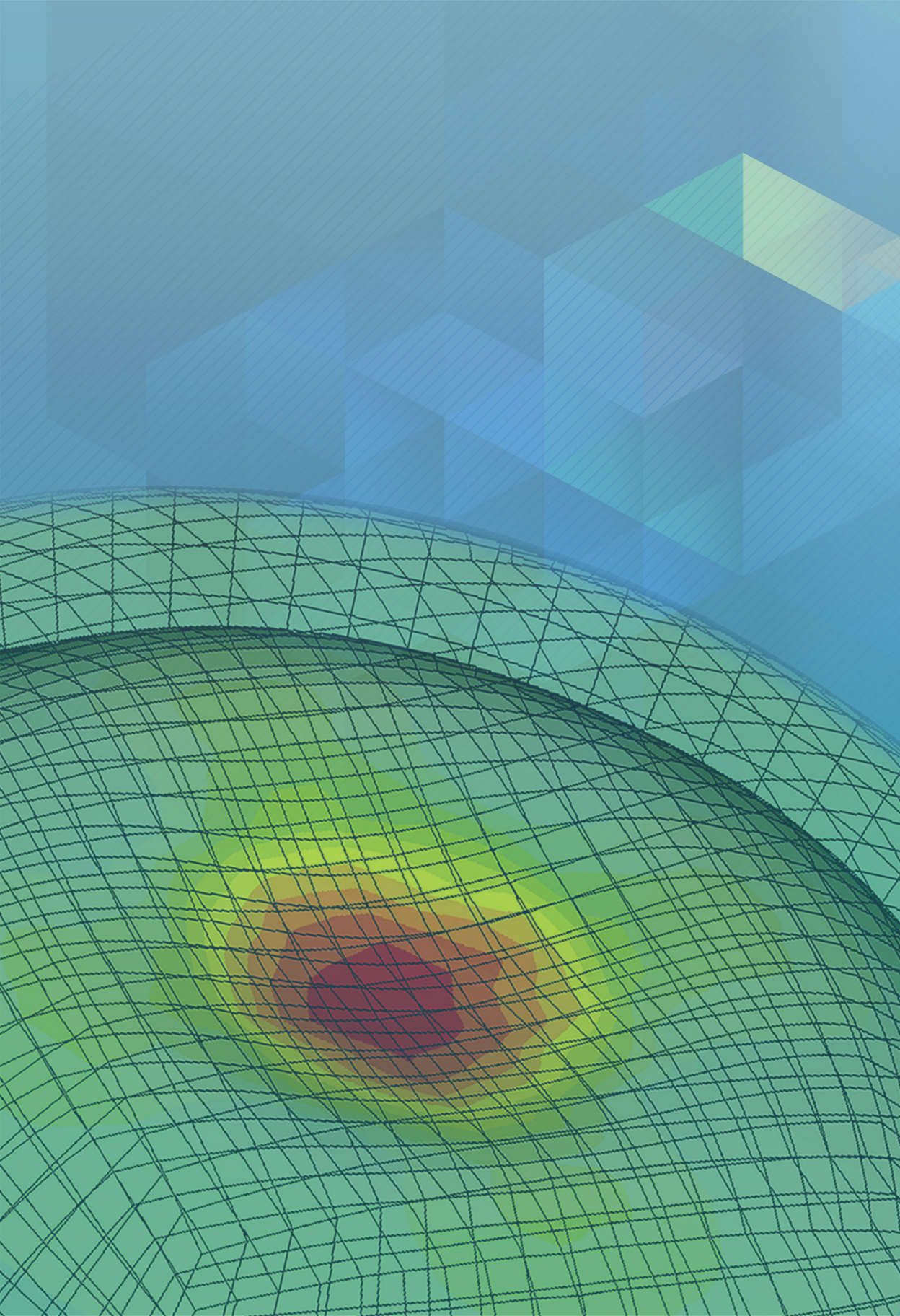
- laser in situ keratomileusis: finite-element analysis. *J Cataract Refract Surg* 2014;40:971-980.
5. Kamiya K, Shimizu K, Ohmoto F. Comparison of the changes in corneal biomechanical properties after photorefractive keratectomy and laser in situ keratomileusis. *Cornea* 2009;28:765-769.
  6. Hashemi H, Asgari S, Mortazavi M, Ghaffari R. Evaluation of Corneal Biomechanics After Excimer Laser Corneal Refractive Surgery in High Myopic Patients Using Dynamic Scheimpflug Technology. *Eye Contact Lens* 2017;43:371-377.
  7. Hassan Z, Modis L, Jr., Szalai E, Berta A, Nemeth G. Examination of ocular biomechanics with a new Scheimpflug technology after corneal refractive surgery. *Cont Lens Anterior Eye* 2014;37:337-341.
  8. Pedersen IB, Bak-Nielsen S, Vestergaard AH, Ivarsen A, Hjortdal J. Corneal biomechanical properties after LASIK, ReLEx flex, and ReLEx smile by Scheimpflug-based dynamic tonometry. *Graefes Arch Clin Exp Ophthalmol* 2014;252:1329-1335.
  9. Shen Y, Chen Z, Knorz MC, Li M, Zhao J, Zhou X. Comparison of corneal deformation parameters after SMILE, LASEK, and femtosecond laser-assisted LASIK. *J Refract Surg* 2014;30:310-318.
  10. Sefat SM, Wiltfang R, Bechmann M, Mayer WJ, Kampik A, Kook D. Evaluation of Changes in Human Corneas After

- Femtosecond Laser-Assisted LASIK and Small-Incision Lenticule Extraction (SMILE) Using Non-Contact Tonometry and Ultra-High-Speed Camera (Corvis ST). *Curr Eye Res* 2016;41:917-922.
11. Sinha Roy A, Kurian M, Matalia H, Shetty R. Air-puff associated quantification of non-linear biomechanical properties of the human cornea in vivo. *J Mech Behav Biomed Mater* 2015;48:173-182.
  12. Mrochen M, Donitzky C, Wullner C, Loffler J. Wavefront-optimized ablation profiles: theoretical background. *J Cataract Refract Surg* 2004;30:775-785.
  13. Shroff R, Francis M, Pahuja N, Veeboy L, Shetty R, Sinha Roy A. Quantitative Evaluation of Microdistortions in Bowman's Layer and Corneal Deformation after Small Incision Lenticule Extraction. *Transl Vis Sci Technol* 2016;5:12.
  14. Grytz R, Meschke G. A computational remodeling approach to predict the physiological architecture of the collagen fibril network in corneo-scleral shells. *Biomech Model Mechanobiol* 2010;9:225-235.
  15. Matalia J, Francis M, Tejwani S, Dudeja G, Rajappa N, Sinha Roy A. Role of Age and Myopia in Simultaneous Assessment of Corneal and Extraocular Tissue Stiffness by Air-Puff Applanation. *J Refract Surg* 2016;32:486-493.
  16. Matalia J, Francis M, Gogri P, Panmand P, Matalia H, Sinha Roy A. Correlation of Corneal Biomechanical Stiffness With

- Refractive Error and Ocular Biometry in a Pediatric Population. *Cornea* 2017;36:1221-1226.
17. Bak-Nielsen S, Pedersen IB, Ivarsen A, Hjortdal J. Repeatability, reproducibility, and age dependency of dynamic Scheimpflug-based pneumotonometer and its correlation with a dynamic bidirectional pneumotometry device. *Cornea* 2015;34:71-77.
  18. Lopes BT, Roberts CJ, Elsheikh A, et al. Repeatability and Reproducibility of Intraocular Pressure and Dynamic Corneal Response Parameters Assessed by the Corvis ST. *J Ophthalmol* 2017;2017:8515742.
  19. Seven I, Vahdati A, Pedersen IB, et al. Contralateral Eye Comparison of SMILE and Flap-Based Corneal Refractive Surgery: Computational Analysis of Biomechanical Impact. *J Refract Surg* 2017;33:444-453.
  20. Dupps WJ, Jr., Wilson SE. Biomechanics and wound healing in the cornea. *Exp Eye Res* 2006;83:709-720.
  21. Hjortdal JO, Moller-Pedersen T, Ivarsen A, Ehlers N. Corneal power, thickness, and stiffness: results of a prospective randomized controlled trial of PRK and LASIK for myopia. *J Cataract Refract Surg* 2005;31:21-29.
  22. Shetty R, Francis M, Shroff R, et al. Corneal Biomechanical Changes and Tissue Remodeling After SMILE and LASIK. *Invest Ophthalmol Vis Sci* 2017;58:5703-5712.

23. Simonini I, Pandolfi A. The influence of intraocular pressure and air jet pressure on corneal contactless tonometry tests. *J Mech Behav Biomed Mater* 2016;58:75-89.







# A novel simulation software to predict postoperative corneal stiffness prior to laser vision correction

Francis M, Shetty R, Padmanabhan P, Vinciguerra R,  
Vinciguerra P, Lippera M, Matalia H, Khamar P,  
Chinnappaiah N, Mukundan D, Nuijts RMMA, Sinha  
Roy A

Accepted for publication in J Cataract Refract Surg

**Purpose:** To develop a novel virtual surgery simulation platform to predict postoperative corneal stiffness ( $K_{C_{mean}}$ ) after laser vision correction (LVC) surgery

**Methods:** 529 eyes from 529 patients from three eye centres and 10 post-SMILE ectasia eyes were included. The software (called AcuSimX™) derived the anisotropic, fibril and extra-cellular matrix biomechanical properties (using finite element calculation) of the cornea using the preoperative Corvis-ST, Pentacam (OCULUS Optikgerate GmbH, Germany) measurement and inverse finite element method assuming published healthy collagen fibril orientations. Then, the software computed postoperative  $K_{C_{mean}}$  was adjusted with an artificial intelligence (AI) model (Orange AI, Slovenia) for measurement uncertainties. A decision tree was developed to classify ectasia from normal eyes using the software computed and preoperative parameters.

**Results:** In the training cohort ( $n = 371$ ), the mean absolute error (MAE) and intraclass correlation coefficient (ICC) were 6.24 N/m and 0.84 [95% CI: 0.80-0.87], respectively. Similarly in the test cohort ( $n = 158$ ), these were 6.47 N/m and 0.84 [0.78-0.89], respectively. In the 10 ectasia eyes, the measured *in vivo* (74.01 [70.01, 78.01]) and software computed (74.1 [69.03, 79.17])  $K_{C_{mean}}$  weren't statistically different ( $p=0.96$ ). The decision tree classification had an AUROC of 1.0.



**Conclusion:** The novel software provided an easy to use virtual surgery simulation platform for post-LVC corneal stiffness prediction and ectasia risk assessment by clinicians. Further assessments with ectasia after surgeries other than SMILE are required.

## Introduction

Corneal biomechanics has emerged as a significant determinant of planning and management of laser vision correction (LVC) surgery in recent years.<sup>1-7</sup> This highlights the need for finding the most biomechanically favorable LVC procedure, e.g., photorefractive keratectomy (PRK), femtosecond laser-assisted in situ keratomileusis (LASIK) and small incision lenticule extraction (SMILE), for a patient. However, the biomechanical alterations to the cornea differ among procedures and the occurrence of ectasia still continue to be reported.<sup>1, 5-7</sup> Ectasia after LVC results in visual degradation due to adverse changes in corneal shape, aberrations and corneal thickness.<sup>1, 8</sup> The risk factors of ectasia suggest that the preoperative quantification of corneal biomechanical properties could play an important role in the prevention of LVC induced ectasia.<sup>1, 3, 9</sup> Currently, the Corvis-ST (OCULUS Optikgerate GmbH, Wetzlar, Germany) is used for biomechanical assessment of the human cornea.<sup>10-12</sup> The Corvis-ST was a newer instrument which featured novel feature additions over the Ocular Response Analyser (Reichert, Inc., Depew, NY, USA) such as delineation of corneal deformation from the whole eye movement and a highly repeatable pressure pulse profile.<sup>10, 11, 13</sup>

The Corvis-ST reports empirical biomechanical parameters such as the Corneal biomechanical index (CBI) and Tomographic biomechanical Index (TBI).<sup>3, 14, 15</sup> The TBI also uses the Belin /

Ambrósio enhanced ectasia display deviation (BAD-D) score reported by Pentacam (OCULUS Optikgerate Gmbh, Wetzlar, Germany).<sup>15</sup> These parameters were designed primarily for preoperative evaluation of subclinical and clinical ectasia. However, these parameters did not include the effect of tissue ablation on preoperative corneal stiffness and resultant biomechanical change in corneal deformation. This may contribute to continued occurrence of ectasia after LVC despite preoperative evaluation by indices such as CBI and TBI. An alternative strategy was proposed where computational modelling using the preoperative *in vivo* measurement of Corvis-ST allowed prediction of the postoperative corneal stiffness and was validated in a small cohort of eyes.<sup>16</sup> However, setting up computational models of corneal biomechanics are technically very challenging for clinicians to use for routine decision making since these models use several open source and/or proprietary software and require specialized expertise.<sup>10, 16</sup> A similar application of computational modeling exists in the field of interventional cardiology called the HeartFlow FFR<sub>CT</sub> Analysis (HeartFlow Inc, USA).<sup>17</sup> The HeartFlow FFR<sub>CT</sub> Analysis uses coronary tomography images and computational fluid dynamics to calculate the fractional flow reserve (FFR) non-invasively before intervention.<sup>17, 18</sup> Thus, similar applications to predict post-refractive surgery corneal stiffness using preoperative measurements alone could be clinically very useful.

In this study, we developed and validated an easy and user-friendly single software package for preoperative prediction of postoperative corneal stiffness after LVC. The software performed computations using 3-dimensional finite element simulation of corneal biomechanics and artificial intelligence models. The software was tested retrospectively on a large cohort of LASIK, PRK and SMILE eyes to develop the artificial intelligence model. The software predicted the postoperative corneal stiffness relative to the preoperative corneal stiffness derived from the Corvis-ST. Further, the predictions of the software for ten eyes, which had developed ectasia after LVC and for which preoperative Corvis-ST measurement were available, were also analyzed.

### **Methods**

This study was a retrospective, observational case series approved by the ethics committees of participating institutions (Narayana Nethralaya eye hospital, Bangalore, India; Sankara Nethralaya, Chennai, India; and Humanitas Clinical and Research Center, Rozzano, Italy). The data set used in this study consisted of 529 eyes from 529 patients (237 eyes were from Narayana Nethralaya; 207 eyes were from Sankara Nethralaya; 85 eyes were from Humanitas Clinical and Research Center). The study was planned and conducted following the tenets of the Declaration of Helsinki. Additionally, a data set of 10 eyes with post-SMILE ectasia was also used ( $n = 7$  eyes operated in Narayana

Nethralaya eye hospital; n = 3 eyes operated in other eye clinics and referred to Narayana Nethralaya for further management). These 10 eyes had a preoperative and postoperative Corvis-ST measurement available. In this study, tomography and deformation data were processed using software versions 1.22r09, build: 8354 and 1.6r2036 of Pentacam HR and Corvis-ST, respectively. However, any software version of Pentacam HR and Corvis-ST could be used with our software in the clinics.

### *Software design*

The architecture of our software (AcuSimX, Narayana Ophthalmic Research and Development LLP, India) is described in Figure 1. It used the elevation co-ordinates comma separated value file from Pentacam HR to construct a 3-dimensional volumetric mesh of the cornea. This mesh included an epithelium layer of uniform thickness. Thus, patient specific corneal shape was used for every eye. The coordinates of the anterior edge of the deforming cornea at various time points (140 points, 32 msec approximately) during applanation were exported from the Corvis-ST. The 3-dimensional mesh and co-ordinates of the deforming anterior edge were used to construct an inverse finite element model (iFEM) having fibril reinforced hyperelastic material model for the human cornea.<sup>10, 16</sup> The iFEM calculated the biomechanical anisotropic material constants of the fibril reinforced material model (assuming previously reported collagen fibril directions

of a healthy human cornea) using the patient specific Corvis-ST corneal and whole eye deformation.<sup>16</sup> Once the iFEM computed the material constants of the material model, the same was used in a surgery specific FEM (sFEM) of the patient cornea to simulate the expected postoperative deformation of the cornea. The iFEM and sFEM models used by AcuSimX were described in our earlier publication.<sup>16</sup> The only difference was the use of an open-source mesh generator and large deformation finite element solver (Calculix), which were customized by us for patient-specific iFEM<sup>16</sup> and sFEM<sup>16</sup>. For customization, we used a combination of Python scripting, C++ and Fortran programming languages. Further, a patient interface was built to store and retrieve the results of simulations as a pdf report. In our earlier study, we had used a commercially available finite element solver (ABAQUS, Dassault Systèmes Americas Corporation, Waltham, MA, USA) and TrueGrid meshing (XYZ Scientific Applications, Inc., Pleasant Hill, USA).<sup>16</sup>

The simulated postoperative mesh was automatically generated by AcuSimX using the surgical parameters, e.g., refractive error (planned for surgery) at 12 mm vertex, type of surgery (LASIK, SMILE or PRK), flap/cap settings and optical zone diameter entered by the user. The software automatically used the preoperative Corvis-ST biomechanically corrected intraocular pressure (bIOP) for both iFEM and sFEM. The postoperative deformation amplitude was computed by AcuSimX using sFEM.<sup>16</sup> From the measured preoperative and predicted postoperative (sFEM) deformation amplitude, the mean corneal

A novel simulation software to predict postoperative corneal stiffness

stiffness ( $K_{C_{\text{mean}}}$ ) was computed by AcuSimX and henceforth, will be referred as sFEM postoperative  $K_{C_{\text{mean}}}$ .<sup>5, 11, 12, 19</sup> The  $K_{C_{\text{mean}}}$  was a stiffness parameter derived from an analytical model (spring and dashpot) of corneal deformation and whole-eye movement in response to the dynamic air-puff pressure pulse.<sup>11</sup> This parameter has been extensively studied as a function of age, myopia, in presence of keratoconus and in refractive surgery eyes.<sup>5, 11, 12, 19</sup> The postoperative corneal deformation (sFEM) computed was fed to this analytical model (encoded in AcuSimX) to derive the sFEM postoperative  $K_{C_{\text{mean}}}$ .

Since laser manufacturers use proprietary ablation profiles, some differences between the postoperative tomography are expected for the same magnitude of refractive correction and similar preoperative tomography of the cornea. Our earlier study used only the wavefront optimized ablation profile<sup>16, 20</sup> and the same was used by AcuSimX. Further, the exact registration of postoperative to preoperative Corvis-ST measurement could be a confounder in the analyses. To account for these variabilities, the retrospective data set of 529 eyes was split into two groups of mutually exclusive eyes randomly selected (while ensuring a replicable sampling pattern), one having 70% and the other having 30% of the total eyes. The distribution of eyes was 81, 219 and 229 for SMILE, LASIK, and PRK, respectively. The 70% group was used for training while the other group was used for testing. Using the training group, the sFEM postoperative  $K_{C_{\text{mean}}}$  was compared with the measured *in vivo* postoperative  $K_{C_{\text{mean}}}$  of the same eyes retrospectively.

This comparison was performed by an artificial intelligence (AI) module (lasso linear regression and cross-validation with the “leave one out” option<sup>21</sup>) using Orange AI package 3.28.0 (University of Ljubljana, Slovenia). Preoperative predictors such as surgical parameters, (measured)  $K_{c_{mean}}$ , Pentacam HR reported thinnest corneal thickness and iFEM estimated anisotropic material constants along with postoperative (computed by sFEM)  $K_{c_{mean}}$  were used for training the AI. Additionally, the preoperative velocity, deflection amplitude and deformation amplitude values at applanation 1, applanation 2 and high convex time points and other preoperative parameters reported by the Corvis-ST were also used for AI training. Once the model was built, the lasso linear regression and its coefficients were included in AcuSimX for prospective use in the test dataset. The software reported the final computed (see Figure 1)  $K_{c_{mean}}$  for prospective use and henceforth, will be referred as AcuSimX postoperative  $K_{c_{mean}}$ . Since preoperative optical coherence tomography measurements weren't available for all the eyes in the retrospective study, a uniform epithelium thickness of 53  $\mu\text{m}$  was assumed for all the study eyes.

The agreement between the AcuSimX postoperative  $K_{c_{mean}}$  versus *in vivo* (measured) postoperative  $K_{c_{mean}}$  was evaluated using the mean absolute error (MAE) and correlation coefficient ( $r$ ). Additionally, the intraclass correlation coefficient (ICC) of prediction was also calculated using MedCalc ver. 19.7.2 (MedCalc Inc., Ostend, Belgium). Reported parameters were represented as either mean and 95% confidence or



A novel simulation software to predict postoperative corneal stiffness

prediction interval<sup>22</sup> (as applicable) or as median and 95% confidence interval. The AcuSimX postoperative  $K_{c\text{mean}}$  was reported with the corresponding 95% prediction interval.<sup>22</sup>

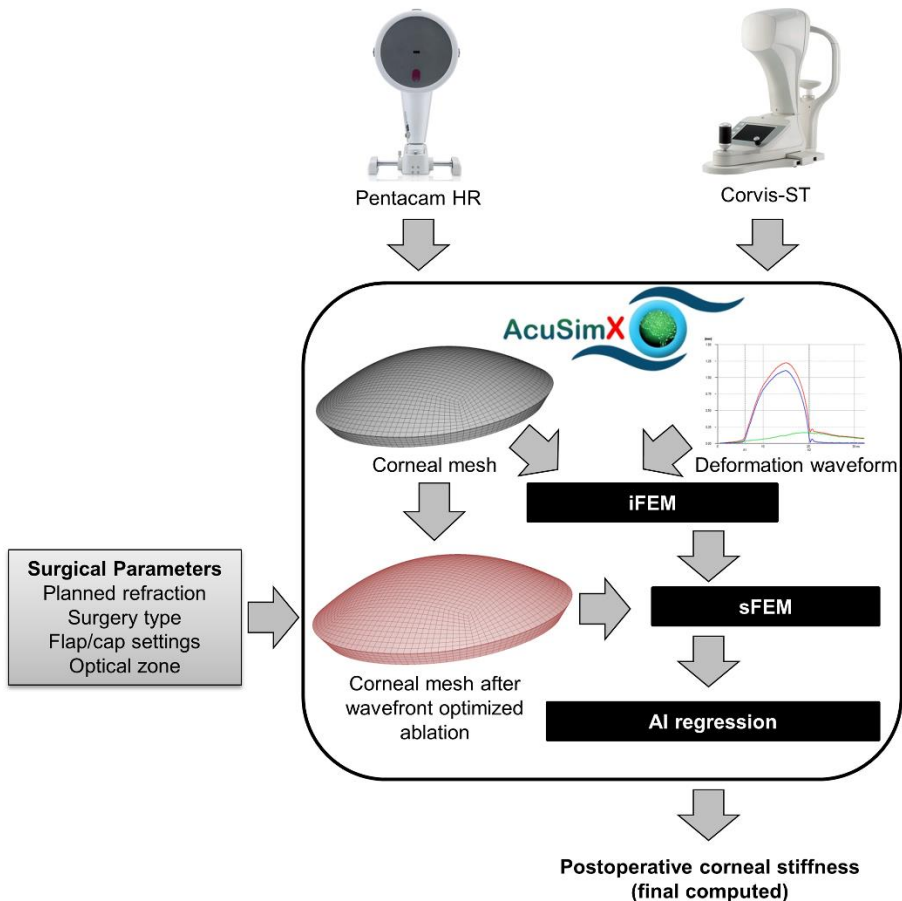


Figure 1: Schematic diagram of AcuSimX software with its key components: inverse finite element model (iFEM), surgery specific FEM (sFEM) and artificial intelligence (AI) regression. Only the name of the software “AcuSimX” is trademarked.

*Retrospective evaluation of post-SMILE ectasia*

The full version of AcuSimX (iFEM, sFEM and AI) was then used to evaluate a post-SMILE ectasia dataset. For these ten eyes, the median follow-up time was 20.5 [95% CI: 5, 37.05] months. In these 10 eyes, the AcuSimX postoperative  $K_{c_{\text{mean}}}$  was compared (ICC, MAE,  $r$  and paired sample t-test) with the measured postoperative  $K_{c_{\text{mean}}}$  by Corvis-ST to assess if there was any significant difference between them. Additionally, the SMILE eyes, which had normal postoperative refractive outcomes and had the AcuSimX postoperative  $K_{c_{\text{mean}}}$  in the range similar to the ectasia eyes, were identified from the group of 529 eyes. The preoperative parameters of these eyes were compared with those of the ectasia eyes using Kruskal–Wallis test based on pseudo-ranks to account for the sample size heterogeneity (PyNonpar 0.2.0 python package).<sup>23</sup> Further, a decision tree with sigmoid calibrated classifier (Orange AI, cross-validation with the “leave one out” option<sup>21</sup>) was used to identify which preoperative Corvis-ST parameters were able to segregate these eyes from the overall cohort of 529 eyes. The classification efficiency of this tree was assessed using area under the receiver operating characteristic curve (AUROC), precision and recall.

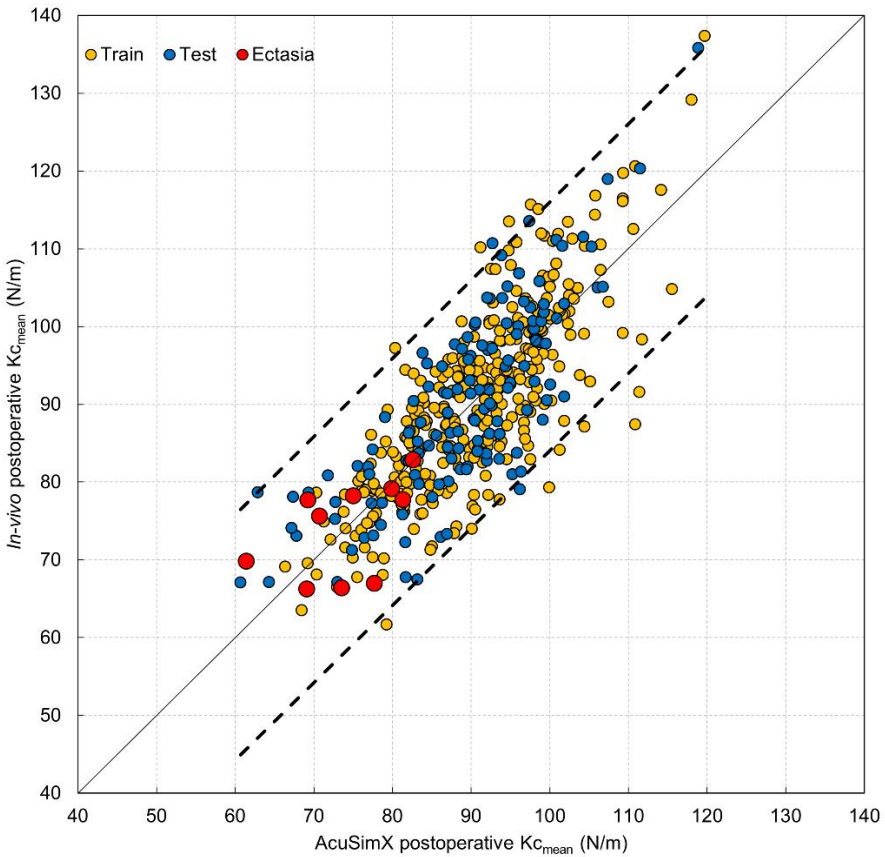


Figure 2: Dot plot of *in vivo* versus AcuSimX postoperative  $K_{c_{mean}}$ , along with its 95% prediction interval (dashed line). Solid continuous line was used to represent the equality line indicating  $y=x$ . All eyes from train, test and ectasia group were included in this figure. All ectasia eyes were after SMILE surgery.

## Results

Table 1 shows the demographics (mean and its' 95% confidence interval) of the training and test datasets. None of the distributions of Corvis-ST, refractive and other demographic data differed between the training and test dataset ( $p>0.05$ ) despite random splitting by the Orange AI package. The ratio of female to male subjects in the train and test cohorts was 1.26 and 1.12, respectively. Similarly, the mean follow-up time post-surgery was 7.19 [6.73, 7.65] and 7.05 [6.33, 7.77] months, respectively. Table 2 shows the agreement between the measured postoperative and AcuSimX postoperative  $K_{C_{mean}}$ . The data in Table 2 are segregated based on combination of iFEM and sFEM, AI alone and combination of all three. AI alone implied that only preoperative parameters were used and no postoperative predictions of stiffness from finite element modeling were included. The unit of corneal stiffness derived by the software was Newton/meter or N/m. It simply implied the force require by the air-puff to cause a unit change in corneal deformation. Higher the magnitude of stiffness, the stronger was the cornea and vice versa. Both the training and test cohorts had similar MAE. Both the eye groups had a strong positive correlation between the measured and AcuSimX postoperative  $K_{C_{mean}}$  ( $r>0.8$ ). Overall, the proposed prediction model (iFEM, sFEM and AI) had an ICC of 0.84 [0.78, 0.89]. A pure AI based prediction model had 0.74 [0.69, 0.79]. Hence, the combination of iFEM, sFEM and AI was implemented in AcuSimX. Figure 2 shows a regression plot of measured and AcuSimX

postoperative  $K_{C_{\text{mean}}}$ , along with its 95% prediction interval (dashed line). The regression (without ectasia eyes) showed a statistically significant linear relationship (slope was 1.0 and y-intercept was 0.51;  $p < 0.001$ ). In this figure, the train and test data are shown as yellow and blue coloured solid circles, respectively. Note the correlation ( $r = 0.79$  in train and test eyes) between the two about the equality line indicating  $y=x$  (solid continuous line). Further, 96.76% and 98.1% of the train and test eyes, respectively, were within the 95% prediction interval (indicated by solid dashed lines in Figure 2).

Table 3 shows the pre and postoperative measured and AcuSimX postoperative  $K_{C_{\text{mean}}}$  of 10 eyes. These 10 eyes developed post-surgery ectasia and had undergone SMILE. The follow-up month varied from 3 to 38 months. The AcuSimX postoperative  $K_{C_{\text{mean}}}$  is reported along with the measured *in vivo* postoperative  $K_{C_{\text{mean}}}$ . All computed values were within the 95% prediction interval (Figure 2) and the mean absolute error (red solid symbols in Figure 2). The MAE for the ectasia eyes was 5 N/m. In these 10 eyes, the measured *in vivo* (74.01 [70.01, 78.01]) and AcuSimX postoperative (74.1 [69.03, 79.17])  $K_{C_{\text{mean}}}$  weren't statistically different ( $p=0.96$ ). The mean difference (95% confidence interval) between the AcuSimX postoperative  $K_{C_{\text{mean}}}$  and measured *in vivo*  $K_{C_{\text{mean}}}$  was -0.09 [-4.65, 4.46] N/m. Similarly, the median difference (95% confidence interval) was -0.49 [-5.46, 6.76] N/m.

From Figure 2, we identified the SMILE eyes which had a normal outcome after surgery and had postoperative  $K_{C_{\text{mean}}}$  less than or equal to 82.85 N/m. This number was chosen since eye 8 (Table 3) had the greatest postoperative  $K_{C_{\text{mean}}}$  among the ectasia eyes. There was no statistically significant difference ( $p>0.05$ ) between the normal outcome and ectasia eyes (Table 4) except for  $DA_{\text{max}}$ . Moreover, the magnitude of preoperative CBI, TBI and BAB-D were marginally higher in the normal outcome eyes compared to the ectasia eyes though this wasn't statistically significant (Table 4). The absence of statistically significant differences between many of the parameters in Table 4 led us to explore discriminative statistical analysis using a decision tree classifier. The decision tree classifier showed that the ectasia eyes had an AcuSimX postoperative  $K_{C_{\text{mean}}}$  less than or equal to 82.85 N/m, Corvis-ST preoperative applanation 2 time less than or equal to 21.67 msec and an optical diameter greater than 6.5 mm (if preoperative  $DA_{\text{max}} \leq 1.187$  mm) or a spherical power correction (if preoperative  $DA_{\text{max}} > 1.187$  mm) greater than 6.5D. The decision tree classifier had an AUROC, precision and recall of 1, 0.99 and 0.99, respectively, for a threshold cut-off of 0.92. The mean run time (95% confidence interval) for an AcuSimX simulation (iFEM, sFEM and AI) on an Intel® Core™ i7-9700 processor computed with 8 GB RAM and Windows 10 64-bit operating system was ~1.47 hours [1.42, 1.52] though latest models of processors should reduce the time further by 25 to 50%.

Table 1: Clinical demographics data that was used in training and testing of the AI model summarized using mean and 95% confidence interval.

Parameters	Train cohort		
	SMILE	LASIK	PRK
n	56	154	161
Age (Years)	26 [24, 29]	25 [24, 26]	27 [25, 28]
bIOP (mmHg)	15.68 [15.17, 16.19]	16.39 [15.95, 16.83]	16.31 [15.9, 16.71]
DA <sub>max</sub> (mm)	1.09 [1.06, 1.11]	1.04 [1.02, 1.05]	1.05 [1.03, 1.06]
CCT ( $\mu\text{m}$ )	527.33 [521.46, 533.2]	543.81 [539.14, 548.47]	543.82 [538.83, 548.81]
<i>in-vivo</i> preoperative K <sub>Cmean</sub> (N/m)	100.45 [96.87, 104.03]	108.78 [106.22, 111.33]	110.31 [108.02, 112.6]
MRSE (D)	-5.24 [-4.69, -5.78]	-6.05 [-5.68, -6.42]	-4.26 [-3.97, -4.55]
OZD (mm)	6 [5.99, 6]	6.21 [6.17, 6.25]	6.86 [6.74, 6.98]
CBI	0.35 [0.29, 0.42]	0.27 [0.23, 0.31]	0.25 [0.21, 0.29]
TBI	0.29 [0.2, 0.37]	0.18 [0.14, 0.22]	0.18 [0.14, 0.21]
BAD-D	1.44 [1.23, 1.64]	1.34 [0.77, 1.9]	1.15 [1.02, 1.27]

Table 1: continued

Test cohort			p-value*
SMILE	LASIK	PRK	
25	65	68	NA
26 [25, 27]	25 [24, 25]	27 [26, 29]	0.88
15.59 [14.79, 16.39]	16.34 [15.6, 17.08]	15.9 [15.35, 16.45]	0.40
1.09 [1.05, 1.12]	1.03 [1.01, 1.06]	1.05 [1.03, 1.07]	0.97
525 [514.28, 535.72]	542.14 [534.69, 549.59]	539.48 [532.7, 546.26]	0.30
99.31 [92.95, 105.67]	108.42 [104.75, 112.09]	107.25 [103.89, 110.61]	0.26
-5.53 [-4.52, -6.54]	-5.77 [-5.19, -6.35]	-4.28 [-3.88, -4.68]	0.80
5.99 [5.97, 6.01]	6.22 [6.15, 6.29]	6.85 [6.65, 7.06]	0.96
0.3 [0.19, 0.42]	0.29 [0.23, 0.36]	0.29 [0.22, 0.36]	0.36
0.24 [0.13, 0.36]	0.16 [0.11, 0.21]	0.23 [0.17, 0.3]	0.65
1.23 [0.99, 1.48]	0.93 [0.8, 1.06]	1.19 [1.02, 1.37]	0.35

AI = artificial intelligence, n = number of eyes, PRK = photorefractive keratectomy, LASIK = laser-assisted in situ keratomileusis, SMILE = small incision lenticule extraction, bIOP = biomechanically corrected intraocular pressure,  $DA_{max}$  = maximum deformation amplitude, CCT = central corneal thickness, OZD = Optical zone diameter,  $K_{cmean}$  = mean corneal stiffness, MRSE = manifest refraction spherical equivalent, NA = not applicable, CBI = corneal biomechanical index, TBI = tomographic biomechanical index, BAD-D = Belin/Ambrósio enhanced



ectasia display; \* One-way analysis of variance test reported significant difference between training and test cohorts ( $p < 0.05$ ).

Table 2: Agreement between measured *in vivo* postoperative  $K_{c_{mean}}$  and predicted postoperative  $K_{c_{mean}}$ .

Parameters		Complete cohort (except ectasia eyes)			
iFEM and sFEM	MAE (N/m)	11.52			
	r	0.69			
	ICC with 95% CI	0.69 [0.06, 0.86]			
AI	MAE (N/m)	7.57			
	r	0.62			
	ICC with 95% CI	0.74 [0.69, 0.79]			
Parameters		Training cohort			
		SMILE	LASIK	PRK	Overall
Prediction model used in AcuSimX (iFEM, sFEM and AI)	MAE (N/m)	4.44	6.66	6.54	6.24
	r	0.8	0.73	0.7	0.74
	ICC with 95% CI	0.88 [0.8, 0.93]	0.83 [0.76, 0.88]	0.8 [0.73, 0.86]	0.84 [0.8, 0.87]

Table 2: continued

Complete cohort (except ectasia eyes)			
11.52			
0.69			
0.69 [0.06, 0.86]			
7.57			
0.62			
0.74 [0.69, 0.79]			
11.52			
Test cohort			
SMILE	LASIK	PRK	Overall
5.57	6.24	7.06	6.47
0.88	0.77	0.65	0.75
0.93 [0.85, 0.97]	0.84 [0.72, 0.91]	0.77 [0.62, 0.87]	0.84 [0.78, 0.89]

iFEM = inverse finite element model, sFEM = surgery specific FEM, AI = artificial intelligence, MAE = mean absolute error, r = correlation coefficient, ICC = intraclass correlation coefficient, CI = Confidence interval, PRK = photorefractive keratectomy, LASIK = laser-assisted in situ keratomileusis, SMILE = small incision lenticule extraction. For definitions of stiffnesses, refer to Figure 1.

Table 3: Preoperative and postoperative clinical demographics data along with AcuSimX postoperative  $K_{C_{mean}}$  of ectasia (post-SMILE surgery) eyes.

Parameter		Eye 1	Eye 2	Eye 3	Eye 4
<i>in-vivo</i> pre-operative parameters	Age at the time of surgery (years)	24	24	28	26
	Follow-up month after surgery	5	5	36	3
	Gender	Female	Female	Male	Female
	bIOP (mmHg)	15.5	17.1	17.6	16.9
	$DA_{max}$ (mm)	1.27	1.19	1.23	1.2
	CCT ( $\mu\text{m}$ )	545	543	507	533
	<i>in-vivo</i> pre-operative $K_{C_{mean}}$ (N/m)	79.81	86.43	81.93	94.9
	MRSE (D)	-9.25	-10.5	-6.5	-9.88
	Optical zone diameter (mm)	6	6	6	6
	CBI	0.21	0.07	0.09	0.14
	TBI	0	0	0.26	0.11
	BAD-D	0.47	0.93	1.21	1.21
Predicted post-operative parameter	sFEM post-operative $K_{C_{mean}}$ (N/m)	56.12	57.44	62.47	65.59
	AcuSimX post-operative $K_{C_{mean}}$ (N/m) with prediction interval	73.51 [57.34, 89.68]	77.67 [61.55, 93.79]	70.72 [54, 87.44]	81.33 [65.01, 97.64]
<i>in-vivo</i> post-operative parameter	<i>in-vivo</i> post-operative $K_{C_{mean}}$ (N/m)	66.38	66.96	75.63	77.72

Table 3: continued

Eye 5	Eye 6	Eye 7	Eye 8	Eye 9	Eye 10
26	24	24	24	24	30
5	26	26	38	38	15
Female	Female	Female	Male	Male	Male
16.7	18	17.9	15.8	15.2	10.9
1.2	1.27	1.29	1.06	1.06	1.21
531	491	505	515	501	533
91.18	79.85	73.93	107.22	99.62	85.68
-7.5	-7.88	-8.5	-4.7	-5.13	-2.3
6	6	6	6.8	6.8	7
0.23	0.69	0.29	0.69	0.73	0.84
0.11	0.28	0.18	0.2	0.99	0.41
0.98	1.4	1.31	1.39	2.0	2.4
65.26	58.31	52.62	75.26	68.38	68.36
79.89	69.23	61.38	82.85	78.2	66.22
[63.9, 95.88]	[53.45, 85.02]	[44.36, 78.4]	[67.72, 97.98]	[62.98, 93.43]	[51.19, 81.26]
79.15	77.69	69.82	82.62	75.01	69.08

sFEM = surgery specific FEM, bIOP = biomechanically corrected intraocular pressure,  $DA_{\max}$  = maximum deformation amplitude, CCT = central corneal thickness,  $K_{c_{\text{mean}}}$  = mean corneal stiffness, MRSE = manifest refraction spherical equivalent, CBI = corneal biomechanical index, TBI = tomographic Biomechanical Index, BAD D = Belin/Ambrósio enhanced ectasia display

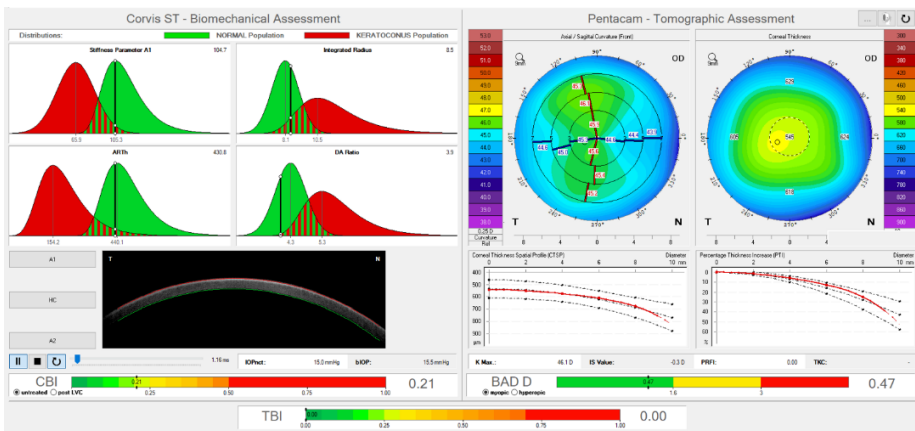
Table 4: Statistical comparison of preoperative parameters between post-SMILE ectasia eyes and a subset of eyes with normal refractive outcomes after SMILE surgery. The subset was defined as eyes which had AcuSimX postoperative  $K_{c_{mean}}$  in the range of ectasia eyes (less than or equal to 82.85 N/m). All values are reported as median and 95% confidence interval along with the p-value from Kruskal–Wallis test.

	Ectasia eyes	Post-SMILE eyes with normal outcomes (with AcuSimX postoperative $K_{c_{mean}} \leq 82.85$ N/m)	p-value*
n	10	32	NA
Age at the time of surgery (Years)	24 [24, 27]	24 [22, 26]	0.4
bIOP (mmHg)	16.8 [15.34, 17.76]	16.45 [15.3, 16.8]	0.4
DA <sub>max</sub> (mm)	1.21 [1.12, 1.27]	1.17 [1.12, 1.18]	0.03*
CCT (μm)	523 [502.9, 538.25]	517 [514, 522]	0.96
in-vivo preoperative $K_{c_{mean}}$ (N/m)	86.06 [79.83, 97.38]	87.44 [84.63, 92.45]	0.53
MRSE (D)	-7.69 [-4.9, -9.58]	-5.75 [-6.63, -5]	0.08
CBI	0.26 [0.11, 0.71]	0.4 [0.21, 0.51]	0.94
TBI	0.19 [0.05, 0.35]	0.2 [0.12, 0.34]	0.61
BAD-D	1.26 [0.95, 1.72]	1.49 [1.29, 1.75]	0.17

## Chapter 6

$n$  = number of eyes,  $\text{bIOP}$  = biomechanically corrected intraocular pressure,  $\text{DA}_{\text{max}}$  = maximum deformation amplitude,  $\text{CCT}$  = central corneal thickness,  $\text{Kc}_{\text{mean}}$  = mean corneal stiffness,  $\text{MRSE}$  = manifest refraction spherical equivalent,  $\text{CBI}$  = corneal biomechanical index,  $\text{TBI}$  = tomographic Biomechanical Index,  $\text{BAD D}$  = Belin/Ambrósio enhanced ectasia display

\* Kruskal–Wallis test reported significant difference between the groups based on pseudo-ranks ( $p < 0.05$ ).<sup>23</sup>



Supplemental Figure 1: Corvis-ST biomechanical/Tomographic assessment display for “Eye 1”. Here, the CBI, BAD-D and TBI magnitudes were within the range of magnitudes seen in healthy corneas.

## Discussion

A virtual simulation software should be able to accurately predict the biomechanical parameters used at the preoperative stage for selection of surgery. This study showed that AcuSimX had predictive value in estimating postoperative corneal stiffness of the cornea by simulating the postoperative Corvis-ST deformation amplitude using advanced computational modeling, biomechanical material models and tomography. AcuSimX realized this objective since a significant linear association between the measured and computed  $K_{C_{\text{mean}}}$  was obtained in regression analysis (Figure 2). The setup of a single predictive model (iFEM, sFEM and AI) took about 20 keyboard strokes and an average run time well suited for evaluating surgical candidates. The inputs to the software were known to refractive surgeons and did not require a steep learning curve. The lack of easy-to-use FEM tools in the clinic has been a hindrance since large sample sizes are required to develop nomograms for better identification of corneas at risk for ectasia, and the use of commercial FEM tools is not feasible for surgeons. Current science states that the ectatic eyes display lower corneal stiffness postoperatively than non-ectatic eyes.<sup>1, 3</sup> Thus, a predictive simulation that yields a low corneal stiffness postoperatively combined with preoperative parameters similar to the preoperative parameters of eyes, which progressed to ectasia after LVC, could significantly provide additional safeguard to both patients and surgeons. For example, case “Eye 1” (Supplemental Figure 1) belonged to a 24 year old female

subject with normal CBI, TBI and BAD-D but developed ectasia after a -9.25 D spherical equivalent correction. Here, the refractive error could be the primary reason for the onset of ectasia after surgery in this cornea with patient specific preoperative biomechanical stiffness and other parameters. In other words, two corneas with similar preoperative stiffnesses, other Corvis-ST and tomography parameters but with different refractive errors may have a differential outcome leading to ectasia in the eye with greater refractive error. By incorporating biomechanical simulation, the aim of AcuSimX is to improve upon current risk factors such as leaving a theoretical residual stromal bed thickness of 250  $\mu\text{m}$  or greater. Our prediction-based approach achieved an AUROC of 1.0. Nonetheless, a detailed prospective study would be required to validate these results for all types of surgeries (LASIK and PRK in addition to SMILE).

An important feature of the software was the incorporation of patient specific finite element modeling for determination of cornea specific biomechanical material constants and postoperative Corvis-ST deformation amplitude. The results of the finite element simulations were further refined by incorporating preoperative patient demographics, surgery specifications and AI. A notable use of finite element modeling for biomechanical assessment of the cornea was the Stress-Strain Index (SSI).<sup>24</sup> However, the Corvis-ST uses a regression approach to determine SSI of each cornea without performing patient specific finite element modeling.<sup>24</sup> To the best of our knowledge,



AcuSimX is one of a kind software in the field of ophthalmology that can perform advanced biomechanical computations while being deployed at clinical sites and with the use of conventional computers. The use of AI regression improved the prediction by AcuSimX. Our earlier publication had achieved an ICC  $> 0.95$  across all surgical categories (12 eyes per surgical technique).<sup>16</sup> However, the ICC was 0.84 [0.78, 0.89] when a larger dataset of 529 eyes across all surgeries was used (Table 2). One of the potential reasons for decrease in ICC could be the assumption of wavefront optimized ablation profile irrespective of the type of surgery. Our postoperative mesh generation for the planned surgical parameters was derived from wavefront optimized spherocylindrical correction formulation.<sup>16, 20</sup> However, actual ablation profiles will vary across platforms. In future, laser platform specific ablation profile could further improve the ICC and needs to be studied.

Additionally, laser ablation systems have to adjust for loss of efficiency from the mid to peripheral cornea.<sup>25, 26</sup> In a recent study, the difference between predicted and measured postoperative CCT reduction was  $13.20 \pm 9.34 \mu\text{m}$  and  $13.12 \pm 8.68 \mu\text{m}$  in LASIK and SMILE eyes, respectively, using ultrasound pachymetry.<sup>25</sup> Further, the SMILE eyes had a systematic overestimation of CCT on tomography and this overestimation was also influenced by the amount of refractive correction.<sup>25</sup> There was no direct relation of these overestimations on visual outcomes.<sup>25</sup> However, these overestimations may have

influenced the accuracy of sFEM computed  $K_{C_{\text{mean}}}$ . Another feature of the human cornea is that the epithelium thickness is generally non-uniform even preoperatively.<sup>27</sup> Improved estimates of postoperative thickness remodeling (epithelium<sup>27</sup> and stroma) in 3-D may improve the sFEM results and subsequent AI regressions further (Figure 1). Another confounding factor in the models was the unknown tissue healing effects.<sup>16</sup> Our models aimed to mitigate these effects by modeling long-term wound healing response similar to our previous study.<sup>16</sup> The Corvis-ST provides deformation of only a cross-section of the cornea and as such spatial variation in  $K_{C_{\text{mean}}}$  could not be assessed. Future versions of AcuSimX could include additional deformation data from additional image frames, if available from the device. Since data from different centers with varied clinical management practices was used, we incorporated real world scenario in the implementation of AI.

Currently, AcuSimX can include spatially varying epithelium thickness in the 3-dimensional mesh models of iFEM and sFEM models but cannot estimate the postoperative changes in epithelium thickness. Also, future FEM could incorporate patient-specific collagen fibril directions derived from techniques such as polarization-sensitive optical coherence tomography.<sup>28</sup> In this study, the sample size of post-SMILE ectasia eyes used for the decision tree classifier was small (Table 3). Hence, the risk interpretation of the decision tree may only apply to post-SMILE eyes. Additionally, the decision tree was built using “leave one out” cross-validation and not an independent sample set due to the

low sample size. Another limitation was that a single  $K_{C_{mean}}$  representing the whole cornea was assumed. Currently, we are limited to a single image frame in the Corvis-ST. In future developments, we can add more frames of the deforming cornea if the device acquires them in real time. This would allow us to map spatial variation in  $K_{C_{mean}}$ . This is the first time that  $K_{C_{mean}}$  was evaluated as one of the significant discriminator between eyes which may be ectatic after LVC and eyes which may be non-ectatic. The exact time frame of occurrence of ectasia after LVC is difficult to predict but this wasn't the objective of this study. Only the preoperative biomechanical risk assessment using corneal deformation measured by Corvis-ST and patient-specific corneal tomography was the primary goal of the simulation software. In summary, this study was able to develop and evaluate a FEM simulation-based software to predict postoperative corneal stiffness after LVC surgery. The model showed predictability of the same in normal as well as ectasia eyes and could be useful for planning of refractive surgeries.

*What was known*

- Ectasia is a rare complication after laser vision correction (LVC) surgery associated with low corneal stiffness. Predicting postoperative corneal stiffness could help prevent it.

- No predictive clinical approach currently exists that could predict postoperative corneal stiffness after LVC surgery using preoperative information.

*What this paper adds*

- Novel predictive simulation software was developed and evaluated to predict postoperative corneal stiffness. The agreement of computed and measured postoperative corneal stiffness was characterized in eyes with normal refractive outcomes and post-surgery ectasia.
- A LVC screening procedure with predicted corneal stiffness at the preoperative planning stage was introduced.

**Author Contributions**

**Francis M:** Concept and design, data acquisition, analysis and interpretation of data, drafting manuscript, and statistical analysis

**Shetty R:** Concept and design, critical revision of manuscript, securing funding, supervision and final approval.

**Padmanabhan P:** Concept and design, data acquisition, analysis and interpretation of data, drafting manuscript, and critical revision of manuscript.

**Vinciguerra R:** Concept and design, data acquisition, analysis and interpretation of data, drafting manuscript, and critical revision of manuscript.

**Vinciguerra P:** Critical revision of manuscript and final approval.

**Lipperera M:** Data acquisition, analysis and interpretation of data, and drafting manuscript.

**Matalia H:** Concept and design, data acquisition, analysis and interpretation of data, drafting manuscript, and critical revision of manuscript.

**Khamar P:** Data acquisition, analysis and interpretation of data, and drafting manuscript.

**Chinnappaiah N:** Data acquisition, analysis and interpretation of data, and drafting manuscript.

**Mukundan D:** Data acquisition, analysis and interpretation of data, and drafting manuscript.

**Nuijts RMMA:** Concept and design, critical revision of manuscript, supervision and final approval.

**Sinha Roy A:** Concept and design, critical revision of manuscript, securing funding, supervision and final approval.

## References

1. Dupps WJ, Jr. Structural relationships in post-refractive surgery ectasia: What have we learned? *J Cataract Refract Surg* 2021.

2. Chong J, Dupps WJ, Jr. Corneal biomechanics: Measurement and structural correlations. *Exp Eye Res* 2021;205:108508.
3. Salomao MQ, Hofling-Lima AL, Gomes Esporcatte LP, et al. The Role of Corneal Biomechanics for the Evaluation of Ectasia Patients. *Int J Environ Res Public Health* 2020;17.
4. Esporcatte LPG, Salomao MQ, Lopes BT, et al. Biomechanical diagnostics of the cornea. *Eye Vis (Lond)* 2020;7:9.
5. Shetty R, Francis M, Shroff R, et al. Corneal Biomechanical Changes and Tissue Remodeling After SMILE and LASIK. *Invest Ophthalmol Vis Sci* 2017;58:5703-5712.
6. Sinha Roy A, Dupps WJ, Jr., Roberts CJ. Comparison of biomechanical effects of small-incision lenticule extraction and laser in situ keratomileusis: finite-element analysis. *J Cataract Refract Surg* 2014;40:971-980.
7. Reinstein DZ, Archer TJ, Randleman JB. Mathematical model to compare the relative tensile strength of the cornea after PRK, LASIK, and small incision lenticule extraction. *J Refract Surg* 2013;29:454-460.
8. Khamar P, Dalal R, Chandapura R, et al. Corneal tomographic features of postrefractive surgery ectasia. *J Biophotonics* 2019;12:e201800253.

9. Roberts CJ, Dupps WJ, Jr. Biomechanics of corneal ectasia and biomechanical treatments. *J Cataract Refract Surg* 2014;40:991-998.
10. Sinha Roy A, Kurian M, Matalia H, Shetty R. Air-puff associated quantification of non-linear biomechanical properties of the human cornea in vivo. *J Mech Behav Biomed Mater* 2015;48:173-182.
11. Francis M, Pahuja N, Shroff R, et al. Waveform analysis of deformation amplitude and deflection amplitude in normal, suspect, and keratoconic eyes. *J Cataract Refract Surg* 2017;43:1271-1280.
12. Matalia J, Francis M, Tejwani S, Dudeja G, Rajappa N, Sinha Roy A. Role of Age and Myopia in Simultaneous Assessment of Corneal and Extraocular Tissue Stiffness by Air-Puff Applanation. *J Refract Surg* 2016;32:486-493.
13. Roberts CJ. Concepts and misconceptions in corneal biomechanics. *J Cataract Refract Surg* 2014;40:862-869.
14. Vinciguerra R, Ambrosio R, Jr., Elsheikh A, et al. Detection of Keratoconus With a New Biomechanical Index. *J Refract Surg* 2016;32:803-810.
15. Ambrosio R, Jr., Lopes BT, Faria-Correia F, et al. Integration of Scheimpflug-Based Corneal Tomography and Biomechanical Assessments for Enhancing Ectasia Detection. *J Refract Surg* 2017;33:434-443.

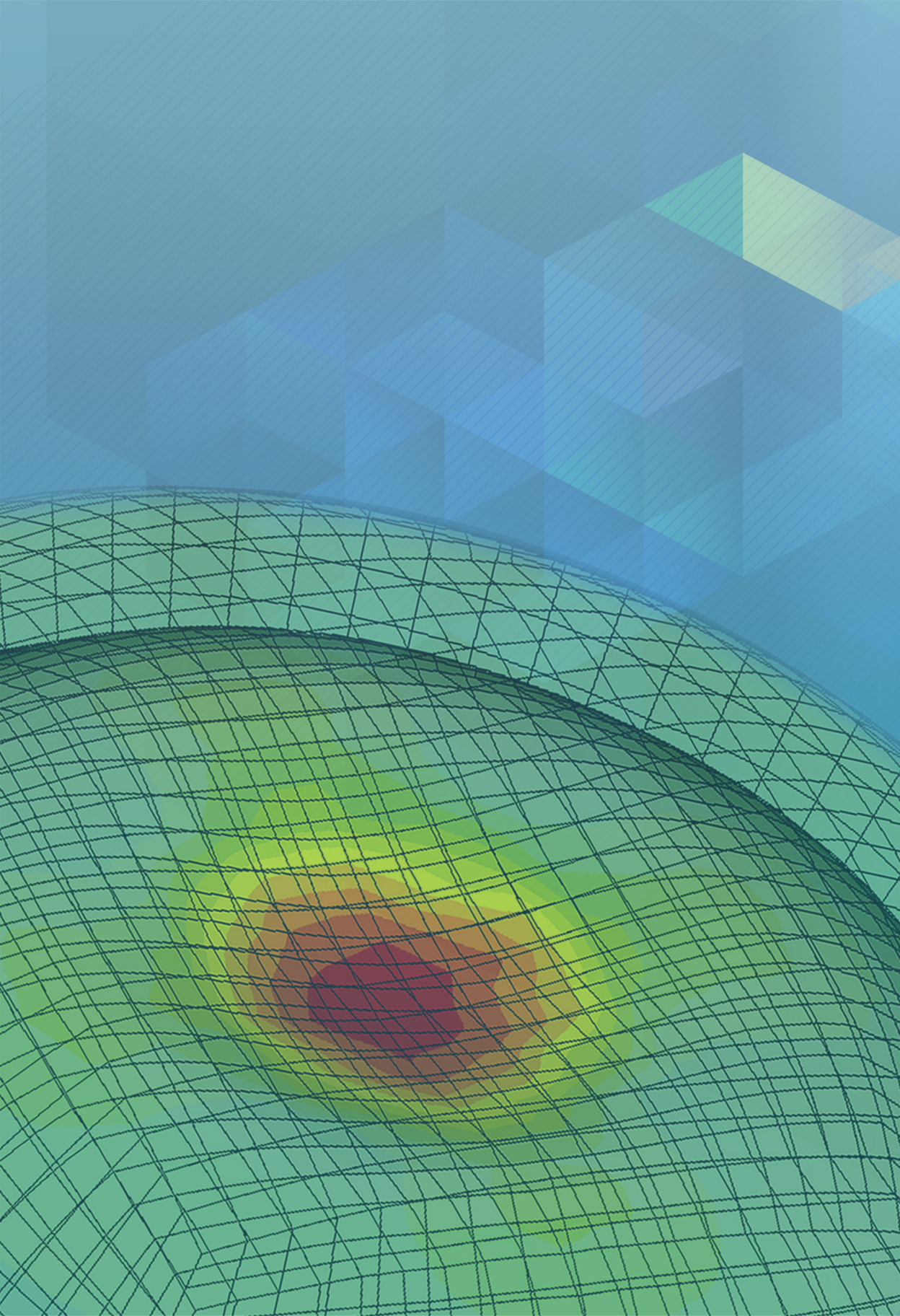
16. Francis M, Khamar P, Shetty R, et al. In Vivo Prediction of Air-Puff Induced Corneal Deformation Using LASIK, SMILE, and PRK Finite Element Simulations. *Invest Ophthalmol Vis Sci* 2018;59:5320-5328.
17. Taylor CA, Fonte TA, Min JK. Computational fluid dynamics applied to cardiac computed tomography for noninvasive quantification of fractional flow reserve: scientific basis. *J Am Coll Cardiol* 2013;61:2233-2241.
18. Norgaard BL, Leipsic J, Gaur S, et al. Diagnostic performance of noninvasive fractional flow reserve derived from coronary computed tomography angiography in suspected coronary artery disease: the NXT trial (Analysis of Coronary Blood Flow Using CT Angiography: Next Steps). *J Am Coll Cardiol* 2014;63:1145-1155.
19. Khamar P, Shetty R, Vaishnav R, Francis M, Nuijts R, Sinha Roy A. Biomechanics of LASIK Flap and SMILE Cap: A Prospective, Clinical Study. *J Refract Surg* 2019;35:324-332.
20. Mrochen M, Donitzky C, Wullner C, Loffler J. Wavefront-optimized ablation profiles: theoretical background. *J Cataract Refract Surg* 2004;30:775-785.
21. Demšar J, Curk T, Erjavec A, et al. Orange: data mining toolbox in Python. *The Journal of Machine Learning Research* 2013;14:2349-2353.



22. Searle SR. *Matrix algebra useful for statistics*. Second edition. ed. Hoboken, New Jersey: Wiley; 2017:xxxi, 480 pages.
23. Brunner E, Bathke A, Konietzschke F. Rank-and Pseudo-rank Procedures in Factorial Designs—Using R and SAS—Independent Observations Springer Series in Statistics. Springer: Heidelberg; 2019.
24. Eliasy A, Chen KJ, Vinciguerra R, et al. Determination of Corneal Biomechanical Behavior in-vivo for Healthy Eyes Using CorVis ST Tonometry: Stress-Strain Index. *Front Bioeng Biotechnol* 2019;7:105.
25. Wu F, Yin H, Yang Y. Evaluation of the Difference between Predicted and Measured Central Corneal Thickness Reduction after SMILE and Femtosecond Laser-assisted LASIK for Myopia. *Curr Eye Res* 2021;1-7.
26. Ahn J, Yang H, Lew HM, Kim EK. Comparison of the topographic ablation zone after photorefractive keratectomy for myopia using two different excimer lasers. *Eye (Lond)* 2010;24:553-557.
27. Khamar P, Chandapura R, Shetty R, et al. Epithelium Zernike Indices and Artificial Intelligence Can Differentiate Epithelial Remodeling Between Flap and Flapless Refractive Procedures. *J Refract Surg* 2020;36:97-103.
28. Beer F, Patil RP, Sinha-Roy A, Baumann B, Pircher M, Hitzenberger CK. Ultrahigh Resolution Polarization

Sensitive Optical Coherence Tomography of the Human Cornea with Conical Scanning Pattern and Variable Dispersion Compensation. *Appl Sci (Basel)* 2019;9:4245.







## Chapter 7

---

# Customization of corneal crosslinking in keratoconus using eye specific computational modeling

Francis M, Kundu G, Khamar P, Dadachanji Z, Shetty R, Nuijts RMMA, Sinha Roy A

Under Review

EMBARGO

# Chapter 8

---

## Discussion



Reports suggest that the market scope of refractive surgery would grow by 9.6% from 2020 to 2025 despite the Covid-19 pandemic, with annual surgery volume increasing to 5.8 million (report by Eyewire News on 19/01/2021, <https://eyewire.news/?p=13466>). While refractive surgery is generally a safe procedure, the incidence of ectasia is still not zero.<sup>1-5</sup> Advancements in screening protocols, treatment methodology and postoperative management have greatly reduced the incidence of ectasia, but have not prevented it.<sup>1-5</sup> The first problem statement being looked at in this dissertation was the calculation of corneal stiffness and its contribution to patient screening for laser vision correction (LVC) surgery. The ocular response analyser (ORA; Reichert Ophthalmic Instruments, Buffalo, NY) had been looked at by many research studies to understand corneal biomechanical properties. Literature had reported a reduced magnitude of the corneal hysteresis (CH) and the corneal resistance factor (CRF) in keratoconic eyes.<sup>6, 7</sup> However, the reduced magnitude of these parameters was not sensitive to differentiate between normal and suspect eyes (fellow eye of keratoconus eye) due to increased variability.<sup>8, 9</sup> Thus focus shifted to derive a new ORA waveform based parameters that could segregate the eyes into normal, suspect and keratoconic eyes.<sup>6, 7, 10, 11</sup> However, this search could not yield parameters with sufficient power to detect early keratoconic eyes.<sup>6, 7, 10, 11</sup> Further, the additional variables proposed along with the traditional CH and CRF could not pick up effects of collagen crosslinking,<sup>12</sup> which was shown to result in biomechanical stiffening of the cornea in both ex-vivo and in-vivo studies.<sup>13-17</sup> Corvis-ST

(OCULUS Optikgeräte GmbH, Wetzlar, Germany) is a relatively new air-puff corneal applanation tonometry device that can image the corneal response to air-puff, so it was hypothesized that Corvis-ST waveform analysis would result in better sensitivity and specificity in segregating these eyes. To test this hypothesis, **chapter 2** introduced a whole waveform analysis method to quantify corneal and extra-corneal biomechanical properties using an analytical biomechanical model (ABM).

**Chapter 2** defines the mean and the constant corneal stiffness respectively describing the non-linear and linear forms of corneal stiffness. The use of the non-linear and the linear form of corneal stiffness extends from our knowledge of soft tissue biomechanics, where the strain energy equation has both linear and non-linear terms.<sup>18-</sup>  
<sup>21</sup> The key finding of this study was that the above parameters individually achieved good sensitivity and specificity greater than 90% and 91% respectively while segregating normal eyes from suspect and keratoconus eyes (table 4, **chapter 2**). Further, the first-order combination of the above parameters using logistic regression analysis (equation 4, **chapter 2**) improved the area under the curve to  $1.0 \pm 0.0$  (sensitivity and specificity of 99.6% and 100.0%, respectively). The segregation performance of the new corneal stiffness parameters in the training data set was comparable to the mutually exclusive validation data set. The new corneal stiffness parameters overall achieved a better classification of normal eyes from disease eyes, in comparison to the



Corneal biomechanical index (CBI) and Tomographic and Biomechanical Index (TBI).<sup>22, 23</sup> The study also observed that the cone location magnitude index (CLMI) variables and deflection amplitude were good at segregating suspect eyes from the normal eyes (table 4, **chapter 2**).<sup>24</sup> The effects of intraocular pressure (IOP) and central corneal thickness (CCT) were adjusted using the analysis of covariance (ANCOVA) model due to its significant influence on all the above parameters. **Chapter 2** showed the whole Corvis-ST waveform analysis helped in the selection of eyes for LVC surgery. However, to fully understand the segregation capacity of the new parameters long-term follow-up of the suspect eyes would be required. Another point of interest was concerning whether modelling the cornea as a purely elastic material was accurate. Wang et al. proposed a “Tangent Stiffness Coefficient”, based on the hysteresis loop formed between corneal force and deformation amplitude to derive corneal viscoelasticity.<sup>25</sup> This study achieved sensitivity and specificity of 88.0% and 85.29% respectively segregating normal and keratoconus eyes.<sup>25</sup> The study however failed to use deflection amplitude waveform and erroneously associated the viscous properties of the whole eye movement with the cornea.<sup>25</sup> As mentioned before, almost all biological tissues are nonlinear, and the cornea is no exception.<sup>26, 27</sup> However, the magnitude of the viscous behaviour picked up during measurement depends on the loading-unloading rate.<sup>18, 19</sup>

**Chapter 3** looks into the possibility of detecting the corneal viscous dissipation during Corvis-ST measurement. The lag between measured deformation and applied force in the case of viscous materials is a well-known fact in soft tissue biomechanical analysis.<sup>26, 28</sup> The magnitude of the lag is proportional to the rate of change in the applied stress (loading rate).<sup>26, 28</sup> When corneal viscosity was estimated using a 2-compartment Kelvin-Voigt model (figure A-B, **chapter 3**) using Corvis-ST data the magnitude was virtually zero. Also, estimated parameters from the 2-compartment Kelvin-Voigt model (figure A-B, **chapter 3**) and the standard linear-viscous solid model (figure A-A, **chapter 3**) had no difference as shown by the concordance correlation coefficient greater than 0.99. The Kelvin-Voigt model however detected corneal viscous lag (figure B, **chapter 3**) after artificially phase-shifting the deflection amplitude waveform relative to the air-puff pressure profile. This action was carried out to induce the viscous effect virtually on the waveform.<sup>28</sup> The above observation shows current air-puff profile and associated magnitude and rate of loading may not result in a detectable viscous lag in deflection amplitude waveform. A recent study also arrived at the same conclusion after analysing deformation and deflection amplitude using Burgers viscoelastic model in normal and keratoconic corneas.<sup>29</sup> Keratoconus is known to reduce the elastic modulus of the cornea.<sup>30</sup> Imaging data on in-vivo eyes suggest local degeneration of biomechanical properties,<sup>31</sup> most likely resulting in both elastic and viscous property changes. Even so, the Corvis-ST configuration in its current form was inadequate to assess the viscous

properties (response to second problem statement). Increased air-puff duration of Corvis-ST could provide a greater time scale for the corneal viscous lag to occur. Also, decreased peak air-puff pressure could reduce the effects of whole eye movement.

Literature on biomechanical changes after laser-assisted in situ keratomileusis (LASIK) and small incision lenticule extraction (SMILE) was conflicted on the best corneal stiffness conserving surgical option.<sup>32-39</sup> Few studies report similar changes<sup>36-39</sup> while others report reduced changes after SMILE<sup>32-35</sup>. The development of a predictive simulation would need a detailed understanding of the transient wound healing and deformation response after LASIK and SMILE. **Chapter 4** presents innovative imaging biomarkers for evaluating tissue-level biomechanical, biophysical and optical responses after LVC surgery. The assessment of the transient wound healing was based on Bowman's roughness index (BRI) and corneal speckle distribution. SMILE and LASIK transient wound healing and biomechanical changes during the acute phase were summarized in figures 5a and 5b (**chapter 4**). Postoperative SMILE corneal speckle changed up to 1 week and was nearly back to preoperative distribution by 1<sup>st</sup> month (figure 5a, **chapter 4**). BRI returned to the preoperative level by the 3<sup>rd</sup> month (figure 5a, **chapter 4**). Corneal deformation in post-SMILE eyes continued to remodel up to the 6<sup>th</sup> month follow-up and possibly beyond (figure 5a, **chapter 4**). While in post-LASIK eyes corneal speckle normalized by the 3<sup>rd</sup> month post-surgery, BRI and

corneal deformation continued to remodel even after the 6<sup>th</sup> month follow-up (figure 5b, **chapter 4**). A recent study however reported similar transient wound healing of the cornea after photorefractive keratectomy (PRK), LASIK and SMILE based on the densitometry from Scheimpflug imaging.<sup>40</sup> The contrasting results could be due to the difference in the infrared light of optical coherence tomography (OCT) versus visible blue light (Scheimpflug imaging), not to mention the higher axial resolution of OCT technology enabling the detection of more tissue information. The novel marker BRI was greater in both LASIK and SMILE.<sup>41</sup> We theorized structural changes in the flap/cap region were causing this change. The helical collagen fibres are under tension preoperatively (figure 6, **chapter 4**).<sup>42</sup> Owing to the surgical severing of collagen fibre, the fibres could undergo stress relaxation resulting in collagen crimping,<sup>43</sup> which could result in increased BRI (figure 6, **chapter 4**). Corneal remodelling post-surgery could result in collagen fibres returning to normalcy and lower BRI (figure 6, **chapter 4**). Reduced fibre severed in a cap cut versus the flap cut could explain the variance in the BRI value difference between SMILE and LASIK, respectively. Also, the amount of fibre severed might be the reason for the longer time involved in the return of LASIK BRI value to preoperative levels (figure 5, **chapter 4**).

According to mathematical modeling, the SMILE surgery procedure is less invasive than LASIK by design leading to a logical prediction of biomechanical advantage of SMILE over LASIK.<sup>44, 45</sup>

Corneal stiffness is a cumulative marker of the non-linear stress vs. strain response of the cornea.<sup>46-48</sup> Mean corneal force vs. corneal deformation curves (figure 4, **chapter 4**) were analyzed at discrete locations. At low corneal force, the curve was linear, and an insignificant difference was observed between LASIK and SMILE surgery. However, at higher forces when the collagen fibres bear some of the mechanical stress SMILE showed clear trends toward recovering biomechanical strength (figure 4, **chapter 4**). This observation correlated well with the BRI observation between SMILE and LASIK. The study noted strong inter-dependence in the measured corneal properties in SMILE eyes; transient changes in BRI, corneal speckle and corneal deformation. Such an inter-dependence between these corneal properties was absent in LASIK eyes. Such disparity between LASIK and SMILE could be due to the greater severing of peripheral collagen lamellae in LASIK. In corneal speckle analysis, LASIK eyes showed a greater transient decrease in the number of high-intensity pixels indicating possible greater keratocyte death in the stroma (figure 3, **chapter 4**).<sup>49</sup> In contrast, SMILE eyes could have interface fluid which could present itself as high-intensity pixels in the acute phase (figure 3, **chapter 4**). Also, this could lead to greater stromal light scattering, explaining acute complications after SMILE.<sup>50, 51</sup> There is literature evidence supporting our speckle distribution result.<sup>44, 47-49</sup> Fewer keratocytes apoptosis, less proliferation, less inflammation and faster regeneration of nerve density were noted after SMILE in comparison to other LVC surgery.<sup>49, 52-54</sup> LASIK eyes had keratocyte apoptosis both

above and below the flap interface.<sup>49</sup> However, the same was observed around the lenticular interfaces only after SMILE.<sup>54</sup> This interesting feature of the temporal corneal wound healing, biomechanics and structural changes is being reported for the first time in literature. Observations made in **chapter 4** demonstrate biomechanical, biophysical, and optical response differences between LASIK and SMILE during the acute phase of tissue healing. However, the clinical implications of these differences, in the long run, would require dedicated prospective randomized controlled studies.

ABM cannot derive strain within the tissue due to deformations. Advanced methods based on finite element method (FEM) modelling are needed to estimate this information.<sup>18</sup> **Chapter 5** introduces a surgery specific FEM model to predict postoperative corneal stiffness using just the preoperative data. Surgery specific FEM models for prediction were necessary as we observed that the PRK eyes have the least amount of decrease in corneal stiffness in comparison to SMILE and LASIK (Figure 3, **Chapter 5**). Also, theoretical models have proposed SMILE to cause the least amount of stiffness change in comparison to other LVC surgery.<sup>44, 45</sup> Surgery specific simulations were formulated using the inference drawn from **chapter 4**. As shown by Figures 4A and B (**Chapter 5**) an accurate determination of deformation amplitude post-surgery is possible. The predicted deformation amplitude waveforms can be used to calculate corneal stiffness using the ABM model described in **chapter 2**. Results of

**chapter 5** show that in the PRK eyes predicted values had the highest degree of similarity with the in-vivo values; postoperative stiffness, peak deformation amplitude and peak deflection amplitude. The predictability of postoperative corneal stiffness value in SMILE and LASIK was also excellent (table 2, **chapter 5**). However, reduced agreement in peak deformation amplitude and deflection amplitude could be due to the flap or cap cut. Two variants of corneal remodelling were introduced in this chapter concerning the short and long-term healing of the cornea based on the observations made in **chapter 4** and our previous work on the subject.<sup>55</sup> SMILE spared a significant amount of peripheral collagen lamellae; which were cut in LASIK. Also, **chapter 4** results indicate Bowman's layer distortions returned to normalcy by 6 months after SMILE. But the same remained high even at longer follow-ups for LASIK eyes. **Chapter 5** introduced the first-of-its-kind predictive simulation for corneal deformation after LASIK, SMILE and PRK that had high agreement with the in-vivo postoperative measurement. The third problem statement about predicting postoperative corneal stiffness using preoperative biomechanical information was answered with the findings of **chapter 5**.

**Chapter 6** showcases the proposed AcuSimX™ software platform. The platform integrated the postoperative corneal stiffness predictive model developed in **chapter 5** with the essential base systems such as a graphical user interface, database management and input data quality control enabling it to perform virtual LVC surgery. However,

the model was initially tested using just 36 eyes (**chapter 5**). Hence, **chapter 6** describes a large sample size study using AcuSimX™. The study also developed a decision tree classifier for normal and ectasia eyes at the preoperative stage; using 10 ectasia eyes and 529 normal eyes. Large sample size nomogram development using the FEM model was previously complex and expensive due to the nature of commercial FEM packages. In contrast, AcuSimX™ was easy to use in clinics by clinicians. Overall simulation process takes about 20 keyboard strokes to initialize and run time of 2 hours on an everyday desktop computer. Input for the software was basic CSV export data from Corvis-ST and Pentacam HR along with basic surgical parameters required to be programmed into the LVC system. The current literature states that ectatic eyes had lower corneal stiffness postoperatively than non-ectatic eyes.<sup>56, 57</sup> Thus, a low predicted postoperative corneal stiffness and preoperative parameters similar to the preoperative parameters of ectasia eyes could be used in identifying ectasia risk after LVC (response to fourth problem statement). However, this needs to be evaluated in a prospective randomized controlled study. One of the most important features was the patient-specific FEM model estimating cornea specific preoperative material property constants and postoperative corneal deformation amplitude prediction. The predicted postoperative corneal deformation amplitude was then used in calculating the postoperative corneal stiffness using ABM (**chapter 2**). FEM predicted result was further refined by incorporating preoperative patient parameters from Corvis-ST, Pentacam HR and surgery



specifications in the artificial intelligence (AI) lasso regression model. Stress-Strain Index (SSI) is a new biomechanical parameter introduced in a recent software update of Corvis-ST that uses FEM modelling.<sup>58</sup> However, SSI is not based on a patient-specific FEM model and is adapted to a given patient based on regression.<sup>58</sup> To the best of our knowledge, this is the first advanced biomechanical computation software in the field of ophthalmology that can be deployed at clinical sites and with the use of conventional computers.

The predictive simulation introduced in **chapter 5** achieved an intraclass correlation coefficient (ICC)  $> 0.95$  across all surgical categories (12 eyes per surgical technique). However, in **chapter 6**, ICC with 529 eyes across all surgeries was 0.84 [0.78, 0.89] (table 2, **chapter 6**). One of the potential reasons for the decrease in ICC could be the assumption of a wavefront-optimized ablation profile irrespective of the type of surgery. Our postoperative mesh generation for the planned surgical parameters was derived from wavefront-optimized spherocylindrical correction formulation.<sup>59</sup> However, actual ablation profiles will vary across platforms. In the future, the incorporation of a laser platform-specific ablation profile could further improve the ICC. Additionally, in a recent study, the difference between predicted and measured postoperative CCT reduction was  $13.20 \pm 9.34 \mu\text{m}$  and  $13.12 \pm 8.68 \mu\text{m}$  in LASIK and SMILE eyes, respectively, using ultrasound pachymetry.<sup>60</sup> Also, the SMILE eye's overestimation of CCT was influenced by the amount of refractive correction.<sup>60</sup> The study found no

relation between the overestimation of CCT and visual outcome.<sup>60</sup> However, these overestimations may have influenced the accuracy of the FEM predictive simulations. Another factor that could improve the surgery specific FEM results and subsequent AI regressions was the use of patient-specific epithelium thickness,<sup>61</sup> due to accurate estimates of postoperative thickness models. Current AcuSimX™ incorporated real-world scenarios by using data from different centres with varied clinical management practices.

Another arm of the AcuSimX™ platform is customized corneal crosslinking (CXL) for the treatment of ectatic eyes (**chapter 7**). Customized CXL had generated a lot of interest, especially with reports of the possibility of reducing the region of treatment resulting in a lower average UVA dose delivered to the cornea.<sup>62, 63</sup> Many studies with 6-month to 2-year follow-up had reported greater flattening and reduction in corneal aberrations in the more tried and tested 3 mW/cm<sup>2</sup> for 30 minutes protocol in comparison to accelerated CXL protocols.<sup>64-66</sup> Customized CXL with energy density ranging from 7.2 to 15 J/cm<sup>2</sup> resulted in greater flattening of  $-1.16 \pm 1.37D$  than accelerated crosslinking at 30 mW/cm<sup>2</sup> for 3 minutes (5.4 J/cm<sup>2</sup>) which managed  $0.39 \pm 1.47D$  at 6 months.<sup>67</sup> Thus **chapter 7** aims to develop a computational approach of customized CXL that was driven by biomechanical assumptions and not just curvature or elevation to focus the UVA while delivering tomographic changes similar to or better than the 3 mW/cm<sup>2</sup> protocol (5.4 J/cm<sup>2</sup>). In **chapter 7**, a biomechanically

altered zone was determined using inverse optimization and curvature and, this altered zone was used to set the UV treatment centre and diameter of the circles (response to the fifth problem statement). This methodology set our study apart from the previous clinical or computational studies on customized CXL.

Analysis of corneal tomography parameters in our study showed a median index of height asymmetry (IHA), index of surface variance (ISV), index of height decentration (IHD) and keratoconus index (KI) reduction by 8.35, 9.5, 0.016 and 0.025, respectively (table 1, **chapter 7**). Lang et al. reported mean ISV, IHD and KI were reduced by 1.7, 0.011 and 0.040, respectively, using the 3 mW/cm<sup>2</sup> for 30 minutes protocol.<sup>66</sup> Toker et al. reported the same reduction by 9.90, 9.53, -0.02 and 0.03, respectively, while max keratometry reduced by 2.15D with the 3 mW/cm<sup>2</sup> for 30 minutes protocol.<sup>68</sup> Thus, our customized CXL approach compared well with the outcomes of the 3 mW/cm<sup>2</sup> (5.4 J/cm<sup>2</sup>) group. Also, in all the above studies, the 3 mW/cm<sup>2</sup> group had the best tomographic outcomes compared to accelerated protocols, e.g., 9 mW/cm<sup>2</sup> for 10 minutes and 30 mW/cm<sup>2</sup> for 3 minutes. Corneal aberration analysis showed defocus and spherical aberration increased by 2.85 and 5.2  $\mu\text{m}$  respectively and tend to approach the normative values of the healthy cornea (table 1, **chapter 7**). Thus, it was observed that customized CXL could achieve similar or better results to the 3 mW/cm<sup>2</sup> (5.4 J/cm<sup>2</sup>) group while using a lesser dose of  $4.50\pm 0.33$  J/cm<sup>2</sup> over a mean treatment zone size of  $32.22\pm 4.65$  mm<sup>2</sup>. The comparable

efficacy of the novel AI customized CXL to the time tested Dresden protocol answers the sixth problem statement. However, prospective randomized controlled studies with larger sample sizes and longer follow-ups are needed to validate the above observation of customized CXL in comparison with conventional procedures. Future studies could compare emerging inelastic scattering imaging reported zone to our estimated degeneration zone, e.g Brillouin microscopy reported Brillouin frequency shift<sup>31</sup>.

As explained above, the AcuSimX™ platform had two applications focusing on LVC and ectasia treatment planning using the finite element method (FEM), a mathematical method used for understanding complex engineering and physical phenomenon. The origin of this sophisticated and highly capable technique can be traced back to the 1940s.<sup>69, 70</sup> Traditionally, the use of this technique needs expertise in several open-source and/or proprietary software along with access to high-end computing infrastructure.<sup>18, 71-75</sup> The use of FEM modelling outside the research domain let alone a clinical setup is very rare. The only other relevant platform for patient-specific simulation is called HeartFlow FFR<sub>CT</sub> Analysis (HeartFlow Inc, USA).<sup>76</sup> HeartFlow FFR<sub>CT</sub> Analysis uses computational fluid dynamics to calculate the fractional flow reserve (FFR) non-invasively before the interventional cardiology procedure.<sup>76, 77</sup>

AcuSimX™ platform has the potential to have a profound impact on the laser vision correction planning process. Current planning protocol involves optical and imaging investigations to formulate a plan for a surgical procedure.<sup>78</sup> However, no algorithm or device exists to predict if the plan would result in a successful correction or an ectatic response. AcuSimX™ intervenes at this point providing the much-required capability of understanding the biomechanical implication of the surgical plan. As AcuSimX™ is a software tool the surgeon has the opportunity to optimize the procedure to best suit his patient by simulating multiple surgical plans, thus realizing personalised medicine. The predictive simulation model used in AcuSimX™ was based on an anisotropic hyperelastic fibre dependent material model. The accuracy of this material model to capture preoperative material property is proportional to its prediction accuracy. Thus, future research could focus on incorporating patient-specific fibre models. Polarization-sensitive optical coherence tomography (PS-OCT) device recorded birefringence data could be used for deriving such personalised fibre directionals.<sup>79</sup>

The degeneration zone prediction in the AcuSimX™ platform was based on tomographical reference data. Hence, the true reference for the inverse FEM model was the patient's tomographic data before the disease manifestation. However, the probability of having access to serial progression data was extremely rare thus requiring a healthy eye tomographical data reference. The efficacy of the degeneration zone

calculated was validated in this dissertation (**chapter 7**) using the results of customized CXL treatment centred on the zone. Thus, future studies could validate the use of healthy eye reference data by comparing the calculated degeneration maps to Brillouin microscopy<sup>31</sup> measurements. Unlike a normal eye, keratoconic eyes are known to have a gross organizational change in stromal lamellae.<sup>80</sup> Hence, keratoconic eye material property definitions could be improved using patient-specific fibre directions derived from PS-OCT.<sup>79, 81</sup>

Future research could also focus on adopting the idea of predictive simulation to solve complex prediction questions in ophthalmology such as keratoconic progression, myopic progression, glaucoma-related optic nerve damage, retinal detachment, lens changes etc. All the basic modules for such sophisticated prediction systems such as data management, data quality control, FEM simulation and artificial intelligence (AI) algorithms are already built into AcuSimX™.

## References

1. Randleman JB, Woodward M, Lynn MJ, Stulting RD. Risk assessment for ectasia after corneal refractive surgery. *Ophthalmology* 2008;115:37-50.
2. Moshirfar M, Albarracin JC, Desautels JD, Birdsong OC, Linn SH, Hoopes PC, Sr. Ectasia following small-incision lenticule

- extraction (SMILE): a review of the literature. *Clin Ophthalmol* 2017;11:1683-1688.
3. Bohac M, Koncarevic M, Pasalic A, et al. Incidence and Clinical Characteristics of Post LASIK Ectasia: A Review of over 30,000 LASIK Cases. *Semin Ophthalmol* 2018;33:869-877.
  4. Kachanov AB, Nikulin S, Churakov T, Bauer SM, Kornikov VV, Zimin BA. Corneal ectasia after 10,000 ReLEx SMILE operations: 37 th CONGRESS OF THE ESCRS PROGRAMME 14–18 September 2019. 2019.
  5. Khamar P, Dalal R, Chandapura R, et al. Corneal tomographic features of postrefractive surgery ectasia. *J Biophotonics* 2019;12:e201800253.
  6. Hallahan KM, Sinha Roy A, Ambrosio R, Jr., Salomao M, Dupps WJ, Jr. Discriminant value of custom ocular response analyzer waveform derivatives in keratoconus. *Ophthalmology* 2014;121:459-468.
  7. Luz A, Lopes B, Hallahan KM, et al. Discriminant Value of Custom Ocular Response Analyzer Waveform Derivatives in Forme Fruste Keratoconus. *Am J Ophthalmol* 2016;164:14-21.
  8. Shah S, Laiquzzaman M, Bhojwani R, Mantry S, Cunliffe I. Assessment of the biomechanical properties of the cornea with the ocular response analyzer in normal and keratoconic eyes. *Invest Ophthalmol Vis Sci* 2007;48:3026-3031.
  9. Kirwan C, O'Malley D, O'Keefe M. Corneal hysteresis and corneal resistance factor in keratoectasia: findings using the

- Reichert ocular response analyzer. *Ophthalmologica* 2008;222:334-337.
10. Schweitzer C, Roberts CJ, Mahmoud AM, Colin J, Maurice-Tison S, Kerautret J. Screening of forme fruste keratoconus with the ocular response analyzer. *Invest Ophthalmol Vis Sci* 2010;51:2403-2410.
  11. Galletti JD, Ruisenor Vazquez PR, Fuentes Bonthoux F, Pfortner T, Galletti JG. Multivariate Analysis of the Ocular Response Analyzer's Corneal Deformation Response Curve for Early Keratoconus Detection. *J Ophthalmol* 2015;2015:496382.
  12. Hallahan KM, Rocha K, Roy AS, Randleman JB, Stulting RD, Dupps WJ, Jr. Effects of corneal cross-linking on ocular response analyzer waveform-derived variables in keratoconus and postrefractive surgery ectasia. *Eye Contact Lens* 2014;40:339-344.
  13. Spoerl E, Huhle M, Seiler T. Induction of cross-links in corneal tissue. *Exp Eye Res* 1998;66:97-103.
  14. Wollensak G, Spoerl E, Seiler T. Riboflavin/ultraviolet-a-induced collagen crosslinking for the treatment of keratoconus. *Am J Ophthalmol* 2003;135:620-627.
  15. Vinciguerra P, Camesasca FI, Albe E, Trazza S. Corneal collagen cross-linking for ectasia after excimer laser refractive surgery: 1-year results. *J Refract Surg* 2010;26:486-497.



16. Yildirim A, Cakir H, Kara N, et al. Corneal collagen crosslinking for ectasia after laser in situ keratomileusis: long-term results. *J Cataract Refract Surg* 2014;40:1591-1596.
17. Herber R, Francis M, Spoerl E, Pillunat LE, Raiskup F, Sinha Roy A. Comparison of waveform-derived corneal stiffness and stress-strain extensometry-derived corneal stiffness using different cross-linking irradiances: an experimental study with air-puff applanation of ex vivo porcine eyes. *Graefes Arch Clin Exp Ophthalmol* 2020;258:2173-2184.
18. Sinha Roy A, Kurian M, Matalia H, Shetty R. Air-puff associated quantification of non-linear biomechanical properties of the human cornea in vivo. *J Mech Behav Biomed Mater* 2015;48:173-182.
19. Nguyen TD, Jones RE, Boyce BL. A nonlinear anisotropic viscoelastic model for the tensile behavior of the corneal stroma. *J Biomech Eng* 2008;130:041020.
20. Pandolfi A, Holzapfel GA. Three-dimensional modeling and computational analysis of the human cornea considering distributed collagen fibril orientations. *J Biomech Eng* 2008;130:061006.
21. Sinha Roy A, Dupps WJ, Jr. Patient-specific computational modeling of keratoconus progression and differential responses to collagen cross-linking. *Invest Ophthalmol Vis Sci* 2011;52:9174-9187.

22. Vinciguerra R, Ambrosio R, Jr., Elsheikh A, et al. Detection of Keratoconus With a New Biomechanical Index. *J Refract Surg* 2016;32:803-810.
23. Ambrosio R, Jr., Lopes BT, Faria-Correia F, et al. Integration of Scheimpflug-Based Corneal Tomography and Biomechanical Assessments for Enhancing Ectasia Detection. *J Refract Surg* 2017;33:434-443.
24. Mahmoud AM, Roberts CJ, Lembach RG, et al. CLMI: the cone location and magnitude index. *Cornea* 2008;27:480-487.
25. Wang LK, Tian L, Zheng YP. Determining in vivo elasticity and viscosity with dynamic Scheimpflug imaging analysis in keratoconic and healthy eyes. *J Biophotonics* 2016;9:454-463.
26. De Vicente J. *Viscoelasticity: From Theory to Biological Applications*: BoD—Books on Demand; 2012.
27. Hoeltzel DA, Altman P, Buzard K, Choe K. Strip extensimetry for comparison of the mechanical response of bovine, rabbit, and human corneas. *J Biomech Eng* 1992;114:202-215.
28. Boyce BL, Jones RE, Nguyen TD, Grazier JM. Stress-controlled viscoelastic tensile response of bovine cornea. *J Biomech* 2007;40:2367-2376.
29. Jannesari M, Mosaddegh P, Kadkhodaei M, Kasprzak H, Behrouz MJ. Numerical and clinical investigation on the material model of the cornea in Corvis tonometry tests: differentiation between hyperelasticity and viscoelasticity. *Mechanics of Time-Dependent Materials* 2019;23:373-384.

30. Nash IS, Greene PR, Foster CS. Comparison of mechanical properties of keratoconus and normal corneas. *Exp Eye Res* 1982;35:413-424.
31. Scarcelli G, Besner S, Pineda R, Kalout P, Yun SH. In vivo biomechanical mapping of normal and keratoconus corneas. *JAMA ophthalmology* 2015;133:480-482.
32. Osman IM, Helaly HA, Abdalla M, Shousha MA. Corneal biomechanical changes in eyes with small incision lenticule extraction and laser assisted in situ keratomileusis. *BMC Ophthalmol* 2016;16:123.
33. Wang B, Zhang Z, Naidu RK, et al. Comparison of the change in posterior corneal elevation and corneal biomechanical parameters after small incision lenticule extraction and femtosecond laser-assisted LASIK for high myopia correction. *Cont Lens Anterior Eye* 2016;39:191-196.
34. Wang D, Liu M, Chen Y, et al. Differences in the corneal biomechanical changes after SMILE and LASIK. *J Refract Surg* 2014;30:702-707.
35. Wu D, Wang Y, Zhang L, Wei S, Tang X. Corneal biomechanical effects: small-incision lenticule extraction versus femtosecond laser-assisted laser in situ keratomileusis. *J Cataract Refract Surg* 2014;40:954-962.
36. Zhang J, Zheng L, Zhao X, Xu Y, Chen S. Corneal biomechanics after small-incision lenticule extraction versus Q-value-guided

- femtosecond laser-assisted in situ keratomileusis. *J Curr Ophthalmol* 2016;28:181-187.
37. Sefat SM, Wiltfang R, Bechmann M, Mayer WJ, Kampik A, Kook D. Evaluation of Changes in Human Corneas After Femtosecond Laser-Assisted LASIK and Small-Incision Lenticule Extraction (SMILE) Using Non-Contact Tonometry and Ultra-High-Speed Camera (Corvis ST). *Curr Eye Res* 2016;41:917-922.
  38. Pedersen IB, Bak-Nielsen S, Vestergaard AH, Ivarsen A, Hjortdal J. Corneal biomechanical properties after LASIK, ReLEx flex, and ReLEx smile by Scheimpflug-based dynamic tonometry. *Graefes Arch Clin Exp Ophthalmol* 2014;252:1329-1335.
  39. Agca A, Ozgurhan EB, Demirok A, et al. Comparison of corneal hysteresis and corneal resistance factor after small incision lenticule extraction and femtosecond laser-assisted LASIK: a prospective fellow eye study. *Cont Lens Anterior Eye* 2014;37:77-80.
  40. Poyales F, Garzon N, Mendicute J, et al. Corneal densitometry after photorefractive keratectomy, laser-assisted in situ keratomileusis, and small-incision lenticule extraction. *Eye* 2017.
  41. Pahuja N, Shroff R, Pahanpate P, et al. Application of high resolution OCT to evaluate irregularity of Bowman's layer in asymmetric keratoconus. *J Biophotonics* 2017;10:701-707.

42. Yadav R, Lee KS, Rolland JP, Zavislan JM, Aquavella JV, Yoon G. Micrometer axial resolution OCT for corneal imaging. *Biomed Opt Express* 2011;2:3037-3046.
43. Grytz R, Meschke G. A computational remodeling approach to predict the physiological architecture of the collagen fibril network in corneo-scleral shells. *Biomech Model Mechanobiol* 2010;9:225-235.
44. Reinstein DZ, Archer TJ, Randleman JB. Mathematical model to compare the relative tensile strength of the cornea after PRK, LASIK, and small incision lenticule extraction. *J Refract Surg* 2013;29:454-460.
45. Sinha Roy A, Dupps WJ, Jr., Roberts CJ. Comparison of biomechanical effects of small-incision lenticule extraction and laser in situ keratomileusis: finite-element analysis. *J Cataract Refract Surg* 2014;40:971-980.
46. Matalia J, Francis M, Tejwani S, Dudeja G, Rajappa N, Sinha Roy A. Role of Age and Myopia in Simultaneous Assessment of Corneal and Extraocular Tissue Stiffness by Air-Puff Applanation. *J Refract Surg* 2016;32:486-493.
47. Pahuja N, Kumar NR, Francis M, et al. Correlation of Clinical and Biomechanical Outcomes of Accelerated Crosslinking (9 mW/cm<sup>2</sup>) in 10 minutes) in Keratoconus with Molecular Expression of Ectasia-Related Genes. *Curr Eye Res* 2016;41:1419-1423.

48. Matalia J, Francis M, Gogri P, Panmand P, Matalia H, Sinha Roy A. Correlation of Corneal Biomechanical Stiffness With Refractive Error and Ocular Biometry in a Pediatric Population. *Cornea* 2017;36:1221-1226.
49. Dong Z, Zhou X, Wu J, et al. Small incision lenticule extraction (SMILE) and femtosecond laser LASIK: comparison of corneal wound healing and inflammation. *Br J Ophthalmol* 2014;98:263-269.
50. Agca A, Ozgurhan EB, Yildirim Y, et al. Corneal backscatter analysis by in vivo confocal microscopy: fellow eye comparison of small incision lenticule extraction and femtosecond laser-assisted LASIK. *J Ophthalmol* 2014;2014:265012.
51. Kamiya K, Shimizu K, Igarashi A, Kobashi H. Visual and refractive outcomes of femtosecond lenticule extraction and small-incision lenticule extraction for myopia. *Am J Ophthalmol* 2014;157:128-134 e122.
52. Li M, Niu L, Qin B, et al. Confocal comparison of corneal reinnervation after small incision lenticule extraction (SMILE) and femtosecond laser in situ keratomileusis (FS-LASIK). *PLoS One* 2013;8:e81435.
53. Wei S, Wang Y, Wu D, Zu P, Zhang H, Su X. Ultrastructural Changes and Corneal Wound Healing After SMILE and PRK Procedures. *Curr Eye Res* 2016;41:1316-1325.

54. Sekundo W. *Small Incision Lenticule Extraction (SMILE): principles, techniques, complication management, and future concepts*: Springer; 2015.
55. Shroff R, Francis M, Pahuja N, Veeboy L, Shetty R, Sinha Roy A. Quantitative Evaluation of Microdistortions in Bowman's Layer and Corneal Deformation after Small Incision Lenticule Extraction. *Transl Vis Sci Technol* 2016;5:12.
56. Dupps WJ, Jr., Santhiago MR. Structural relationships in post-refractive surgery ectasia: What have we learned? *J Cataract Refract Surg* 2019;45:391-393.
57. Salomao MQ, Hofling-Lima AL, Gomes Esporcatte LP, et al. The Role of Corneal Biomechanics for the Evaluation of Ectasia Patients. *Int J Environ Res Public Health* 2020;17.
58. Eliasy A, Chen KJ, Vinciguerra R, et al. Determination of Corneal Biomechanical Behavior in-vivo for Healthy Eyes Using CorVis ST Tonometry: Stress-Strain Index. *Front Bioeng Biotechnol* 2019;7:105.
59. Mrochen M, Donitzky C, Wullner C, Loffler J. Wavefront-optimized ablation profiles: theoretical background. *J Cataract Refract Surg* 2004;30:775-785.
60. Wu F, Yin H, Yang Y. Evaluation of the Difference between Predicted and Measured Central Corneal Thickness Reduction after SMILE and Femtosecond Laser-assisted LASIK for Myopia. *Curr Eye Res* 2021;1-7.

61. Khamar P, Chandapura R, Shetty R, et al. Epithelium Zernike Indices and Artificial Intelligence Can Differentiate Epithelial Remodeling Between Flap and Flapless Refractive Procedures. *J Refract Surg* 2020;36:97-103.
62. Seiler TG, Fischinger I, Koller T, Zapp D, Frueh BE, Seiler T. Customized Corneal Cross-linking: One-Year Results. *Am J Ophthalmol* 2016;166:14-21.
63. Shetty R, Pahuja N, Roshan T, et al. Customized Corneal Cross-linking Using Different UVA Beam Profiles. *J Refract Surg* 2017;33:676-682.
64. Mazzotta C, Baiocchi S, Bagaglia SA, Fruschelli M, Meduri A, Rechichi M. Accelerated 15 mW pulsed-light crosslinking to treat progressive keratoconus: Two-year clinical results. *J Cataract Refract Surg* 2017;43:1081-1088.
65. Vounotrypidis E, Athanasiou A, Kortum K, et al. Long-term database analysis of conventional and accelerated crosslinked keratoconic mid-European eyes. *Graefes Arch Clin Exp Ophthalmol* 2018;256:1165-1172.
66. Lang PZ, Hafezi NL, Khandelwal SS, Torres-Netto EA, Hafezi F, Randleman JB. Comparative Functional Outcomes After Corneal Crosslinking Using Standard, Accelerated, and Accelerated With Higher Total Fluence Protocols. *Cornea* 2019;38:433-441.
67. Nordstrom M, Schiller M, Fredriksson A, Behndig A. Refractive improvements and safety with topography-guided corneal

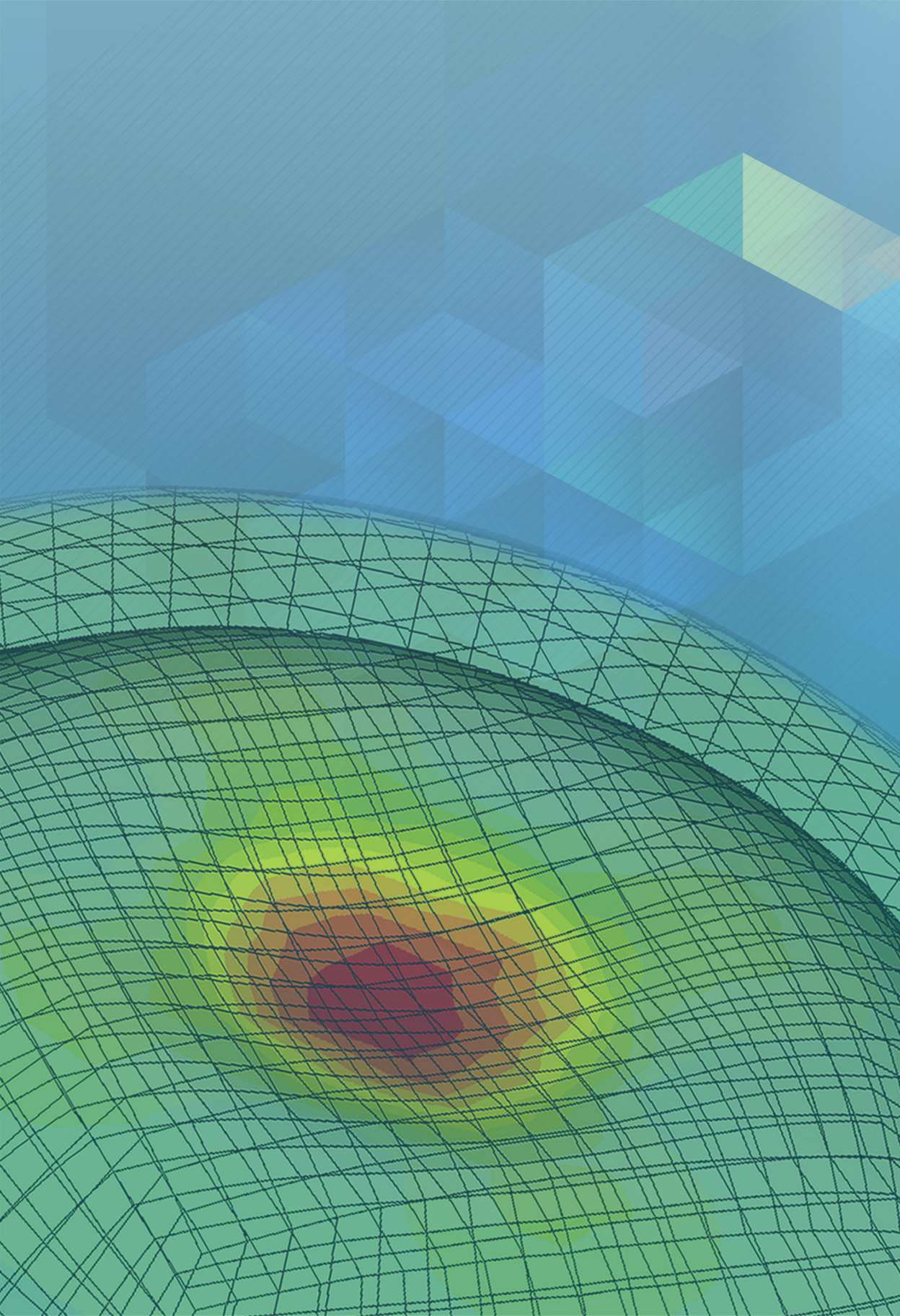


- crosslinking for keratoconus: 1-year results. *Br J Ophthalmol* 2017;101:920-925.
68. Toker E, Cerman E, Ozcan DO, Seferoglu OB. Efficacy of different accelerated corneal crosslinking protocols for progressive keratoconus. *J Cataract Refract Surg* 2017;43:1089-1099.
69. Hrennikoff A. Solution of problems of elasticity by the framework method. 1941.
70. Courant R. Variational methods for the solution of problems of equilibrium and vibrations. *Bulletin of the American mathematical Society* 1943;49:1-23.
71. Pandolfi A, Manganiello F. A model for the human cornea: constitutive formulation and numerical analysis. *Biomech Model Mechanobiol* 2006;5:237-246.
72. Pinsky PM, van der Heide D, Chernyak D. Computational modeling of mechanical anisotropy in the cornea and sclera. *J Cataract Refract Surg* 2005;31:136-145.
73. Studer H, Larrea X, Riedwyl H, Buchler P. Biomechanical model of human cornea based on stromal microstructure. *J Biomech* 2010;43:836-842.
74. Nguyen TD, Boyce BL. An inverse finite element method for determining the anisotropic properties of the cornea. *Biomech Model Mechanobiol* 2011;10:323-337.
75. Petsche SJ, Pinsky PM. The role of 3-D collagen organization in stromal elasticity: a model based on X-ray diffraction data and

- second harmonic-generated images. *Biomech Model Mechanobiol* 2013;12:1101-1113.
76. Taylor CA, Fonte TA, Min JK. Computational fluid dynamics applied to cardiac computed tomography for noninvasive quantification of fractional flow reserve: scientific basis. *J Am Coll Cardiol* 2013;61:2233-2241.
77. Norgaard BL, Leipsic J, Gaur S, et al. Diagnostic performance of noninvasive fractional flow reserve derived from coronary computed tomography angiography in suspected coronary artery disease: the NXT trial (Analysis of Coronary Blood Flow Using CT Angiography: Next Steps). *J Am Coll Cardiol* 2014;63:1145-1155.
78. Ang M, Gatinel D, Reinstein DZ, Mertens E, Alio Del Barrio JL, Alio JL. Refractive surgery beyond 2020. *Eye (Lond)* 2021;35:362-382.
79. Beer F, Patil RP, Sinha-Roy A, Baumann B, Pircher M, Hitzenberger CK. Ultrahigh Resolution Polarization Sensitive Optical Coherence Tomography of the Human Cornea with Conical Scanning Pattern and Variable Dispersion Compensation. *Appl Sci (Basel)* 2019;9:4245.
80. Meek KM, Tuft SJ, Huang Y, et al. Changes in collagen orientation and distribution in keratoconus corneas. *Invest Ophthalmol Vis Sci* 2005;46:1948-1956.
81. Patil R, Shetty R, Narasimhan R, et al. Mapping of corneal birefringence in thin and asymmetric keratoconus corneas with

ultrahigh resolution polarization sensitive OCT. *J Cataract Refract Surg* 2022.







# Chapter 9

---

## Summary



This dissertation is a collection of focused research on corneal tissue responses to customized surgical treatments. It is structured into tissue healing and biomechanical assessment within the domain of laser vision correction (LVC) surgery, predicting postoperative corneal stiffness after LVC and customized collagen cross-linking (CXL) planning for ectasia treatment.

**Chapter 1** starts with background information associated with the problem statements and discusses the structure of this dissertation. **Chapter 2** introduces an analytical biomechanical model (ABM) for Corvis-ST waveform analysis for LVC screening. The ABM derived mean and constant corneal stiffness were used in the separation of the suspect (fellow eye of a keratoconus eye) and the keratoconus eyes from the normal eyes. It was designed to model the cornea as a pure spring, which decision was further validated in **chapter 3**. The chapter investigated two ABM models: first a standard linear-viscous solid model (SLM) similar to chapter 2, then a 2-compartment Kelvin-Voigt model (KVM) in which both the cornea and extra-corneal tissue were modelled as viscoelastic materials. Corneal stiffness parameters derived from both models were almost perfectly similar and corneal viscosity calculated from the KVM model was practically zero for normal eyes. A similar trend was observed in the suspect eye and keratoconic cornea, despite disease-associated localized weakness having a profound effect on both elastic and viscous properties of the diseased cornea. Hence, **chapter 3** concluded that the air-puff applanation technique appeared

inadequate to assess the viscous properties with the analytical models in its current configuration. **Chapter 4** investigated longitudinal tissue healing after LVC surgery from biophysical, structural and biomechanical response perspectives. Optical coherence tomography (OCT) speckle distribution biophysical marker changes after surgery to preoperative distribution in both laser-assisted in situ keratomileusis (LASIK) and small incision lenticule extraction (SMILE) showed two completely different recovery processes. The study found a better transient healing process after SMILE than LASIK overall. Bowman's roughness index (BRI) the structural marker showed differential crimping effects between LASIK and SMILE, due to differences in the number of severed fibres between a flap and a cap procedure. Analysis of mean corneal force vs. corneal deformation curves at higher forces correlated well with the BRI.

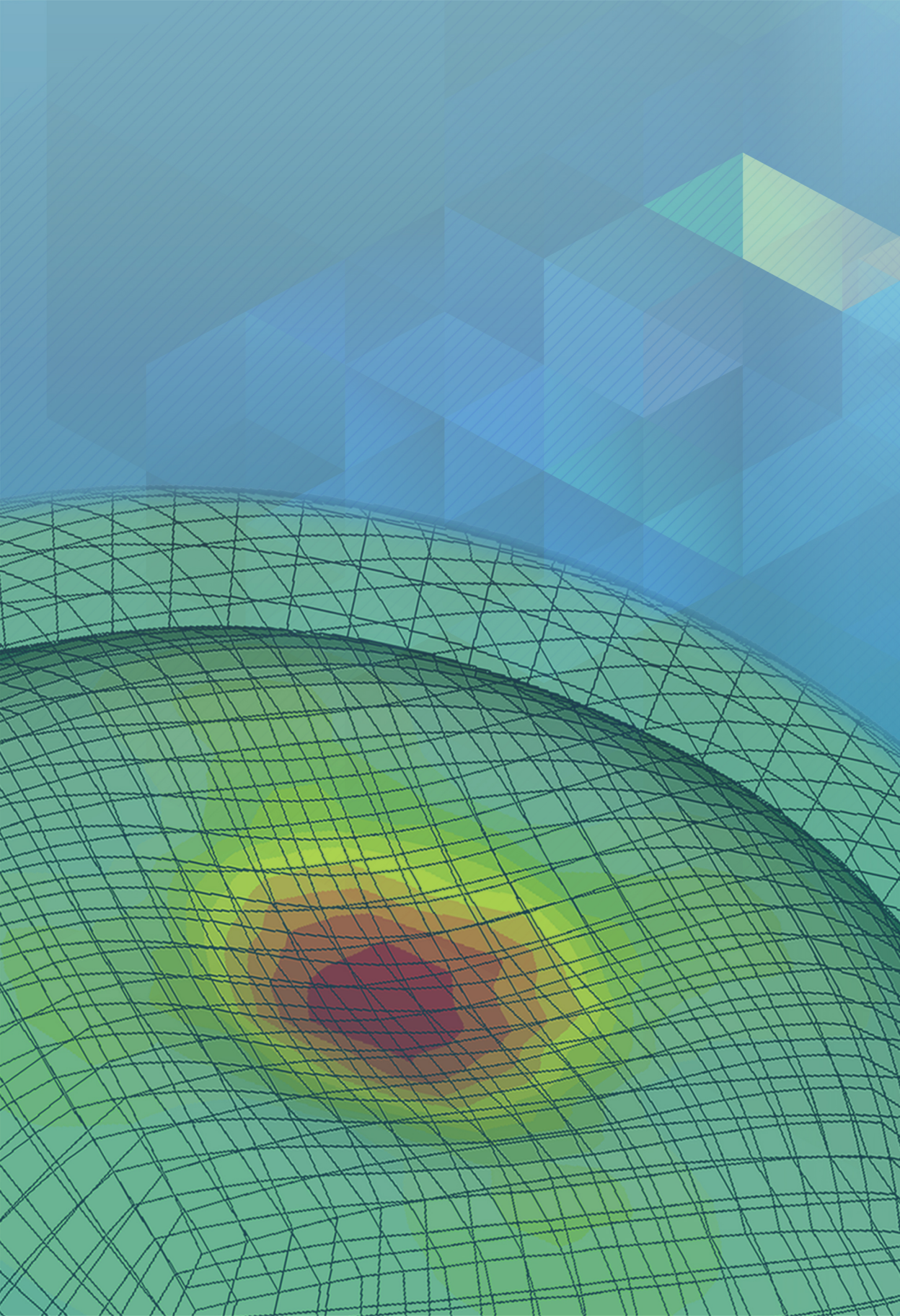
Based on the corneal tissue responses observed in **chapters 2,3 and 4** a postoperative corneal stiffness prediction finite element method (FEM) simulation models for LASIK, SMILE and photorefractive keratectomy (PRK) were introduced in **chapter 5**. The surgery specific models had a short-term and long-term prediction model assuming transient changes in play, and more stable effects of surgery, respectively. Excellent agreement observed between predicted versus the in-vivo postoperative stiffness indicated that our novel predictive simulation may be representative of the in-vivo state of the cornea after surgery. This was the first time such a predictive simulation had been



showcased. However, the surgery specific predictive simulation needed to be validated using a larger database. **Chapter 6** conducted this validation study of the AcuSimX™ platform built from the surgery specific prediction model using 529 eyes from multiple centres around the world comprising LASIK, SMILE and PRK, and an additional 10 eyes that developed ectasia after LVC. The study also introduced a unique preoperative parameters pattern that could assist in identifying potential ectasia eyes before surgery. Thus, a predictive simulation that yields a low corneal stiffness postoperatively combined with preoperative parameters pattern could safeguard both the patients and surgeons further.

A novel customized CXL planning based on an inverse FEM modelling based method to estimate the shape and size of the biomechanical altered zone in an ectatic eye was introduced in **chapter 7**. A 3-dimensional patient-specific model of the cornea was developed from Scheimpflug tomography. Here, initially, the material property of the healthy cornea was assumed, which was then spatially scaled to simulated biomechanical degeneration. The resultant biomechanical degeneration zone was used in the prospective planning of customized CXL procedures. Evaluation of customized CXL results based on the newly generated biomechanical degeneration map showed improved tomographic remodelling of the cornea, comparable to the Dresden protocol. With this predictive simulation approach, better results were achieved using a lower treatment dose.







## Chapter 10

---

# Impact Paragraph



A case report about a 26 year old female subject who underwent refractive surgery sparked this idea of a prediction platform. All preoperative screening tests were normal for the subject and a well laid out postoperative management was followed. But the result was ectasia, diagnosed 3.5 years after the surgery. Questions soon followed from the clinics to the lab. “Why did this happen?” How do we prevent it?” AcuSimX™ was envisioned and then realized to give a predictive edge while planning a laser vision correction (LVC) or a customized collagen cross-linking (CXL) surgery so that such incidents can be prevented. In other words, it can be called a Digital Twin. A digital twin is a concept first practically defined by NASA in 2010, where a digital simulation was used to understand possible spacecraft operations.<sup>1</sup> The idea was that missions can be evaluated virtually on the ground and the best possible approach can be carried out in space. Similarly, we do simulations to understand the complex biomechanical responses of the human cornea and harness this knowledge to better shape the biomechanical outcome after surgery.

AcuSimX™ is introduced in this dissertation as a platform and not software. AcuSimX™ is a collection of software modules to implement any predictive simulation project in the field of ophthalmology. The platform has a 3-dimensional modelling module that can be used to create surfaces from a point cloud, e.g. creating a 3-dimensional corneal model from Pentacam HR tomographer elevation and thickness points. It also includes a module for implementing

complex material property models to transform 3-dimensional structures into the mechanically functional body. AcuSimX™ incorporates mathematical equation solvers to perform finite element method (FEM) calculations using the defined bodies such as the cornea. The platform can also adjust the results using a large data AI-derived correction model, e.g. regression equations developed from AI using normative data.

For any platform to work outside the research domain a certain level of automation and simplicity is required. To this extent, the platform is encapsulated in an intuitive graphical user interface with ergonomic controls and well laid out workflow. Additionally, an internal database management module is present to keep track of the clinical data and simulation results. Most significantly, the platform has a robust input data quality control system. Patient measurement and clinical data suffer quality issues arising from an uncooperative patient (due to dry eyes, low vision etc.), instrument-related or operator related issues. Thus a robust quality control system can help in ensuring results are not affected by lower quality input data.

To the clinical community, this dissertation adds a way to use predictive surgery in clinical practice and thereby reduce the risk of ectasia after LVC procedures. Also, the treatment of keratoconus and post-LVC ectasia utilizing the promising customized CXL procedure.

The platform also provides a framework to envision future applications involving AI and FEM in the ophthalmology domain.

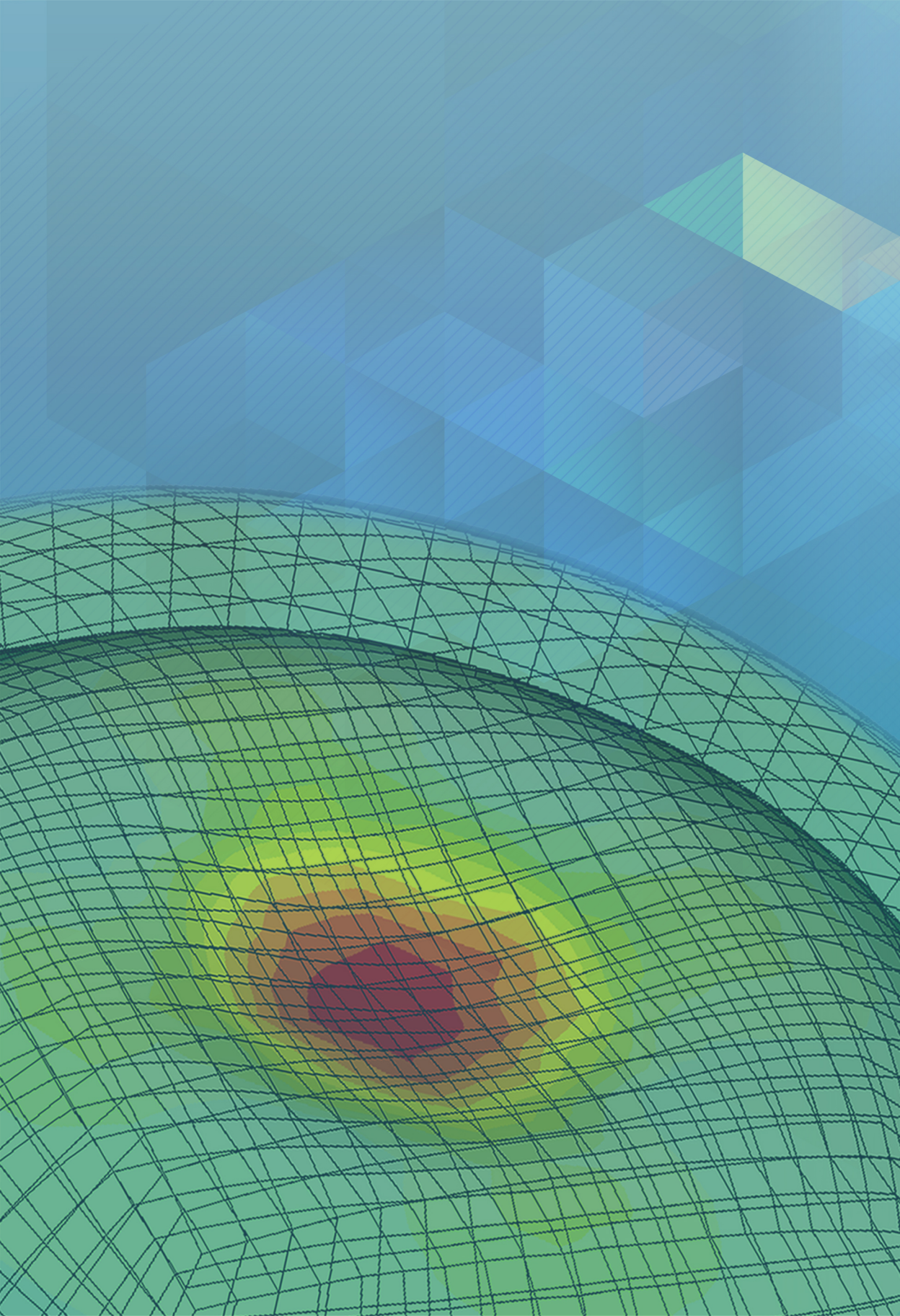
To society, the better prediction of possible ectasia after surgery means an increase in the accessibility of LVC procedures due to decreased false positives in screening tests. Also, increased safety due to reduced false negatives. Reduced ectasia incidence after the LVC procedure could lead to cost savings as further surgical intervention and medical care can be avoided. A well planned customized CXL procedure can increase the flattening and aid in better vision. All of which will help improve the visual acuity of the workforce, one of the most valuable natural resource of any nation.

To the scientific community, the dissertation already has accumulated a sizable normative and ectatic data set. Advanced machine learning and deep learning models which have shown great promise require a huge amount of data. A simple platform for predictive simulation would allow for large scale usage of such technology in the clinic. This would lead to more data generation, which could drive greater scientific research in the field of early diagnosis and treatment management.

## Reference

1. Negri E, Fumagalli L, Macchi M. A review of the roles of digital twin in CPS-based production systems. *Procedia Manufacturing* 2017;11:939-948.



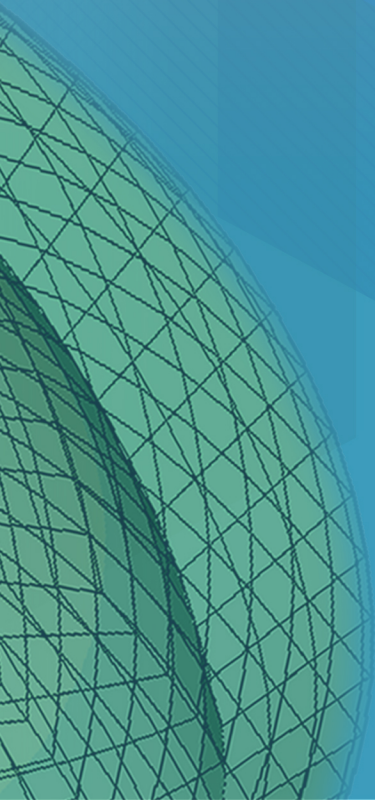




## Chapter 11

---

# Acknowledgement



This doctoral dissertation was an eventful journey. I would like to do my best and acknowledge all those who helped me complete this journey.

A call from Dr. Abhijit Sinha Roy on a fine Sunday morning started this journey back in 2015. From that day onwards he has helped and guided my journey. It was a great honour to work under him. My greatest achievement and worst mistakes were all in his presence, every time he helps me learn from them and move forward. No words would ever suffice to express my gratitude for his guidance and support. Dr. Rohit Shetty my co-supervisor always took time from his busy schedule to be there to guide me in my journey. Discussions with him are very special, it's the time when the work is laid out and connections are made, clinics to science and then to a solution. He ritualistically used such meetings to do two things; motivate me to break my glass ceiling and reinforce the importance of translational research. He is the driving force behind the research atmosphere in our hospital.

Prof. dr. R.M.M.A. (Rudy) Nuijts my supervisor and linchpin of the whole work. Prof Nuijts played a great role in my admittance to the doctoral degree program at Maastricht University. I would like to acknowledge his illuminating words and valuable guidance. Dr. TTJM (Tos) Berendschot is my link to the university and the person whom you can always depend upon. Additionally, many thanks to Maastricht University Medical Center+ (MUMC) for providing me with the

opportunity to do this doctoral research. Also, to Prof. dr. B.M.J. (Bart) Haex for his guidance and support. Special thanks to Dr. Shyam Vasudevarao, technical director, Maastricht University, India for his support.

As an institution, Narayana Nethralaya Foundation and its management team supported this dissertation wholeheartedly. Our chairman Dr. K Bhujang Shetty is an excellent role model. He started Narayana Nethralaya back in 1982 as an eye clinic and then proceeded to build one of the best multi-centre super speciality hospitals in India. His effort was the ground on which all the work at Narayana Nethralaya happens. Also, I would like to acknowledge the entire IBMS lab and GROW lab team for their support and encouragement; especially Dr. Arkasubhra Ghosh, Dr. Swaminathan Sethu, Mr. Rahul Patil, Ms. Nivedhitha G, Mr. Raghav Narasimhan, Mr. Yash Patel and Ms. Anchana A.P. Special thanks to Dr. Naren Shetty (Vice Chairman), Mr. S K Mittal (CEO), Dr. Sri Harsha Nagaraj (Clinical Research) and Dr. Narendra P (COO). Also, the clinical team; Dr. Himanshu P Matalia, Dr. Jyoti Matalia, Dr. Sushma Tejwani, Dr. Pooja Khamar, Dr. Nandini C and Dr. Gairik Kundu. Special thanks to all the former fellows of Narayana Nethralaya; particularly Dr. Rushad Shroff and Dr. Natasha Pahuja for all their support. The entire Narayana Nethralaya family was also with me the whole time.

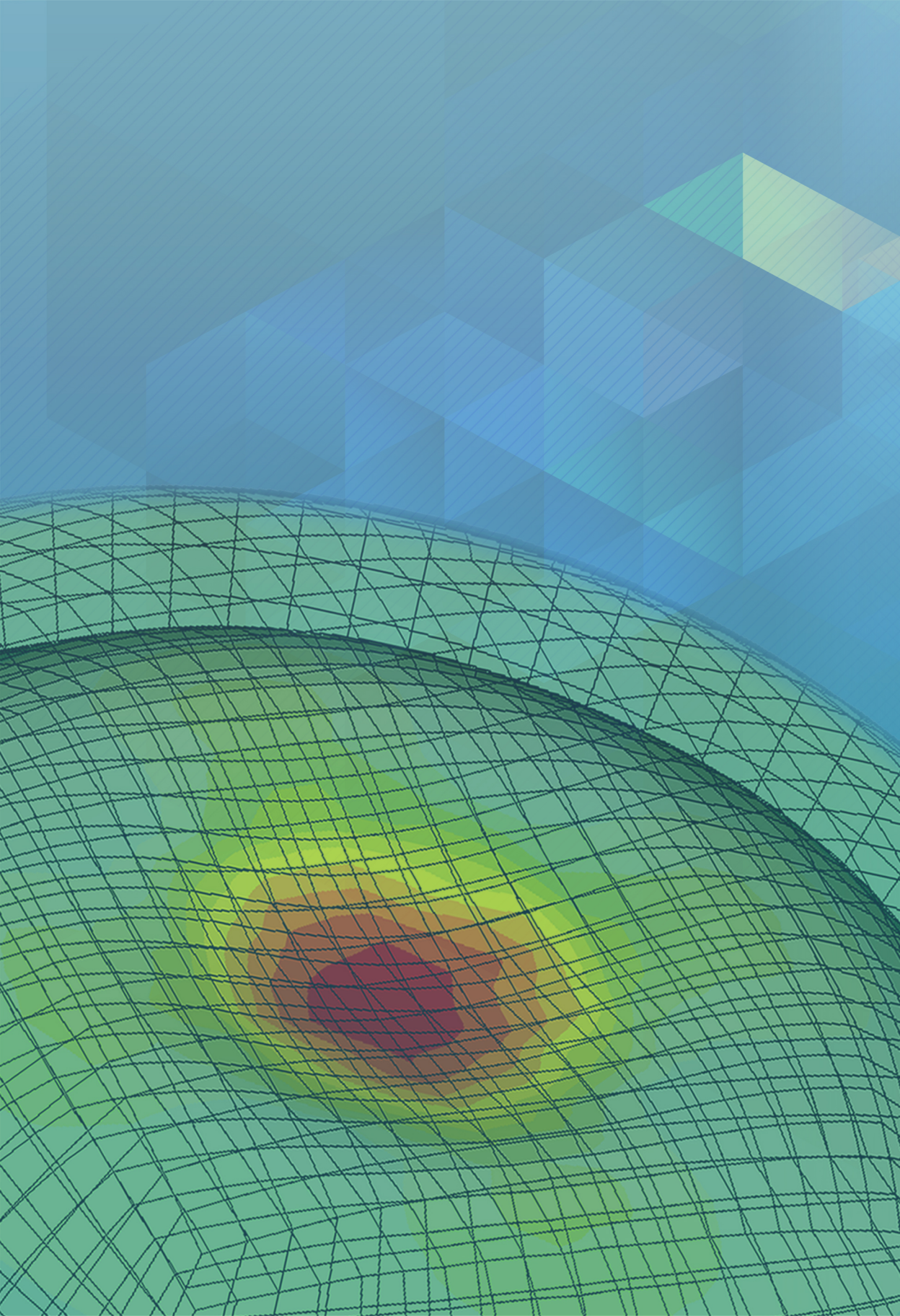
This research wouldn't be complete without the cooperation and support from Dr. Prema Padmanabhan (Medical Research Foundation, Sankara Nethralaya, Chennai, Tamil Nadu, India) and Dr. Riccardo Vinciguerra (Humanitas San Pio X Hospital, Milan, Italy). Also, I would like to acknowledge the help and support from OCULUS Optikgeräte GmbH, Germany; particularly Dr. Sven Reisdorf (Product Manager, OCULUS Optikgeräte GmbH).

Financial support is an essential part of any research study. I am deeply grateful to the Indo-German Science & Technology Centre (IGSTC) for partly funding this dissertation through the grants awarded to Dr. Abhijit. I would like to thank the Association for Research in Vision and Ophthalmology (ARVO) for the publication grant awarded to my article (chapter 5) for publishing in the Investigative Ophthalmology & Visual Science (IOVS) Journal. Also, international travel support award from the Science and Engineering Research Board, Department of Science and Technology, Government of India for presenting my research (chapter 2) at the International Society for Eye Research (ISER) biennial meeting in 2016.

I would like to acknowledge and thank my family for believing and supporting me throughout this journey. My wife Mrs. Smisha Jose is a kind-hearted and loving soul, who stood by my side throughout this journey. She has been supportive and has made countless sacrifices to

get me to this point. Also, to the numerous individuals and events in my life that moulded me and to the almighty force, thank you.



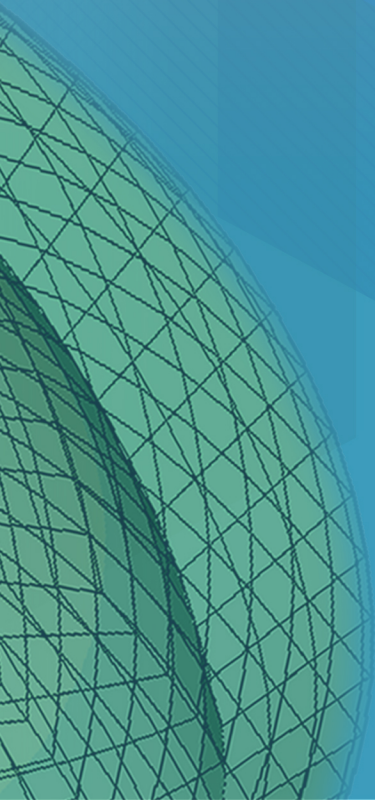




## Chapter 12

---

# Curriculum Vitae





Mathew Francis was born on 24<sup>th</sup> March 1989 in Thrissur (Kerala, India). After his schooling; he joined Sahridaya College of Engineering and Technology, Thrissur (Kerala, India) affiliated with the University of Calicut and completed his Bachelor of Technology degree in Biomedical Engineering. Afterwards, he did two years of industrial training. Then he returned to Sahridaya College and completed his Master of Technology degree in Embedded Systems. In 2015, soon after his masters, he joined the Imaging, Biomechanics and Mathematical Modeling Solutions (IBMS) lab, Narayana Nethralaya Foundation (Bengaluru, India) as Research Engineer. At IBMS lab, he worked on corneal biomechanics analysis and advanced ocular imaging projects. His research activity at the IBMS lab has culminated in this dissertation. Currently, he continues at the IBMS lab as Junior Scientist.

Mathew Francis received the international travel support award from Science and Engineering Research Board, Department of Science and Technology, Government of India for presenting his research titled "Next-generation comprehensive diagnosis of suspect and keratoconus eyes using high-resolution tomography and biomechanics: Thinking beyond topography" at the International Society for Eye Research (ISER) biennial meeting in 2016, Tokyo, Japan. He also received a publication grant from the Association for Research in Vision and Ophthalmology (ARVO) for publishing his research in Investigative Ophthalmology & Visual Science Journal titled "In vivo prediction of air-puff induced corneal deformation using LASIK, SMILE and PRK

finite element simulations". He has contributed to many peer-reviewed journal articles and conference presentations during his career at the IBMS lab. He is also among the listed inventors of two patents.

